Investigation of electronic and magnetic structure of advanced magnetic materials

A thesis presented to

Fachbereich Physik
Universität Osnabrück

Faculty of Physics
Babes-Bolyai University

by

Vasile REDNIC

Scientific supervisors:

Prof. Dr. Manfred NEUMANN

Prof. Dr. Marin COLDEA

Osnabrück
January 2010

Contents

Introduction

The problem of local moments confined to the transition metals (T) sites, i.e., localized behaviour in some aspects of itinerant electrons, is one of the most important issues in the physics of the magnetic alloys and intermetallic compounds. It was found experimentally that under certain conditions the magnetic moment of a transition metal remains localized when solute in another transition metal. The condition for the existence of the local moment at the T site is $\pi\Delta / U < 1$, where Δ is the width of the d states (corresponds to the virtual bound states in the Friedel's model) and U is the Coulomb correlation energy between d electrons.

The 3d band width $\Delta = Z^{1/2}J_h$ depends on the number of near-neighbours Z with d orbitals and the hopping integral J_{ohn}, which is very sensitive to the distance between the atoms. On the other hand, the strength and the sign of the interaction between the neighbouring local moments are determined by the occupation fraction of d-orbitals and the orientation of these orbitals in the lattice. By alloying with other elements, the vicinity of the transition metal atom is changing. This leads to structural modifications with remarkable variations in the electronic structure and magnetic properties of the parent compound.

The understanding and prediction of the properties of mater at atomic level represents one of the great achievements of the last years in science. In this content, the advantage of photoelectron spectroscopy, in the study of electronic structure and properties of matter is due to progress in both, experimental and in relevant theory. Photoemission techniques have been developed sufficiently to become a major tool for the experimental studies of solids. These techniques are also attractive for the study of changes in, or destruction of, crystalline order.

The fine details of the relationship between the electronic structure and the magnetic properties of matter represent a state of the art challenge in the solid state physics. The link is evident even from a didactic approach: electrons are the 'carriers' of spin magnetic moments and their movement around nucleus gives rise to orbital momentum i.e. orbital contribution to the magnetic moments. From a more sophisticated point of view, the information on the electronic structure turns up to be essential for the understanding of magnetic behavior.

The XPS spectra give information on the electrons binding energies, the valence band and the density of states at the Fermi level, the hybridization between orbitals, the ions valence states and the charge transfer between the elements. The energy position and the width of the valence band, the comparison between the valence band and the calculated band structure, the

splitting of the 3s core level, the presence of the satellite structures to the valence band and 2p core levels give information on the localization degree of the 3d electrons, the occupation of the *3d* band, the spin and valence fluctuations effects, which are the basic elements in explaining the magnetic properties of metallic systems based on 3d elements.

In the present study the ternary system Al-Mn-Ni was chosen because the following reasons:

- Manganese is particularly interesting because according to Hund's rule the magnetic moment of the free atom can have the maximum value of 5 μ_B. The antiferromagnetic alloys formed by Mn with nickel, palladium, and platinum have high Néel temperatures, which makes them very promising materials for practical applications, such as pinning layers of GMR and TMR devices.

- Nickel metal is a ferromagnet having a magnetic moment of 0.6 μ_B/Ni. By alloying with Al, the Ni 3d-Al 3sp hybridization leads to a partial ($AlNi_3$) or complete ($AlNi$) filling of Ni 3d band depending on Al concentration and distances between Al and Ni atoms.

- By varying the concentration of the elements the first vicinity of transition metal atoms and the distance between them is different, which leads to important changes in the crystallographic and electronic structure with remarkable effects on the magnetic properties of Mn-Ni-Al alloys and compounds.

The aim of this thesis is to study the changes in the crystallographic, electronic and magnetic structure of the Al-Mn-Ni ternary metallic system by modifying the concentration of the constituent elements.

The thesis is organized in 6 Chapters, followed by the summary. Chapter 1 contains a brief theoretical introduction into the magnetism of metallic systems, as well the principles of X-ray photoelectron spectroscopy, which is the main technique used to investigate the electronic structure of the intermetallic alloys and compounds. The sample preparation details and all the experimental techniques employed in the characterization of the systems are described in Chapter 2. The next 4 Chapters contain the experimental results for $Mn_{1-x}Al_xNi_3$, $Mn_{1-x}Al_xNi$, $Ni_{1-x}Mn_xAl$, and $Ni_{0.7-x}Al_xMn_{0.3}$ systems. The structural, electronic and magnetic properties of the alloys and compounds are investigated by X-ray diffraction, X-ray photoelectron spectroscopy, band structure calculations, magnetization and magnetic susceptibility measurements.

Chapter 1

Theoretical considerations

1.1 General issues of magnetism

All materials have an inherent magnetic character arising from the movements of their electrons. Since dynamic electric fields induce a magnetic field, the orbit of electrons, which creates atomic current loops, results in magnetic fields. An external magnetic field will cause these atomic magnetic fields to align so that they oppose the external field. This is the only magnetic effect that arises from electron pairs. If a material exhibits only this effect in an applied field it is known as a diamagnetic material.

Magnetic properties other than diamagnetism, which is present in all substances, arise from the interactions of unpaired electrons. These properties are traditionally found in transition metals, lanthanides, and their compounds due to the unpaired *d* and *f* electrons on the metal. There are three general types of magnetic behaviors: paramagnetism, in which the unpaired electrons are randomly arranged, ferromagnetism, in which the unpaired electrons are all aligned, and antiferromagnetism, in which the unpaired electrons line up opposite of one another. Ferromagnetic materials have an overall magnetic moment, whereas antiferromagnetic materials have a magnetic moment of zero. A compound is defined as being ferrimagnetic if the electron spins are orientated antiparrallel to one another but, due to an inequality in the number of spins in each orientation, there exists an overall magnetic moment. There are also enforced ferromagnetic substances (called spin-glass-like) in which antiferromagnetic materials have pockets of aligned spins.

1.1.1 The origin of atomic moments

At the atomic scale, magnetism comes from the orbital and spin electronic motions. The nucleus can also carry a small magnetic moment, but it is insignificantly small compared to that of electrons, and it does not affect the gross magnetic properties.

Quantum mechanics gives a fixed energy level to each electron which can be defined by a unique set of quantum numbers:

1. The total or principal quantum number *n* with integral values *1, 2, 3,...* determines the size of the orbit and defines its energy. Electrons in orbits with *n=1, 2, 3,...* are referred to as occupying *K, L, M,...* shells, respectively.

2. The orbital angular momentum quantum number l describes the angular momentum of the orbital motion. For a given value of l, the angular momentum of an electron due to its orbital motion equals $\hbar\sqrt{l(l+1)}$. The number l can take one of the integral values *0, 1, 2,..., n-1*. The electrons with l = *0, 1, 2, 3,...* are referred to as *s, p, d, f, ...* electrons, respectively.

3. The magnetic momentum quantum number m_l describes the component of the orbital angular momentum l along a particular direction. For a given l: m_l= *l, l-1,..., 0,...,-l+1,-l*

4. The spin quantum number m_s describe the component of the electron spin along a particular direction, usually the direction of the applied field. The electron spin s is the intrinsic angular momentum corresponding with the rotation (or spinning) of each electron about an internal axis. The allowed values of m_s are $\pm 1/2$.

According to the *Pauli Exclusion Principle*, each electron occupies a different energy level (or quantum state), thus the states of two electrons are characterized by different sets of quantum numbers *n, l, m_l,* and *m_s*.

The motion of the electron around the nucleus may be considered as a current flowing in a wire having no resistance, which coincides with the electron orbit. The corresponding magnetic effects can be than derived by considering the equivalent magnetic shell. An electron with an orbital angular momentum $\hbar l$ has an associated magnetic moment:

$$\vec{\mu}_l = -\frac{|e|}{2m}\hbar\vec{l} = -\mu_B\vec{l} \tag{1.1}$$

where μ_B is the *Bohr magneton*: $$\mu_B = \frac{e\hbar}{2m} \tag{1.2}$$

The absolute value of the magnetic moment is given by:

$$\left|\vec{\mu}_l\right| = \mu_B\sqrt{l(l+1)} \tag{1.3}$$

The situation is different for the spin angular momentum. In this case, the associated magnetic moment is:

$$\vec{\mu}_s = -g_e\frac{|e|}{2m}\hbar\vec{s} = -g_e\mu_B\vec{s} \tag{1.4}$$

where g_e (=2.002290716) is the spectroscopic splitting factor.

The magnetic moment of a free atom (or ion) is the sum of the moments of all electrons. When describing the atomic origin of magnetism, one has to consider the orbital and spin motions of all electrons as well as the interactions between them. The maximum number of electrons occupying a given shell is:

$$2\sum_{l=0}^{n-1}(2l+1) = 2n^2 \tag{1.5}$$

The total orbital angular momentum and total spin angular momentum of a given atom are defined as:

$$\vec{L} = \sum_i \vec{l}_i \tag{1.6}$$

and respectively:
$$\vec{S} = \sum_i \vec{s}_i \tag{1.7}$$

where the summation extends over all electrons. The summation over a complete shell is zero, so only the incomplete shells contribute effectively to the total angular momentum. The resulted $\vec{S}$ and $\vec{L}$ are coupled through the spin-orbit interaction to form the resultant total angular momentum $\vec{J}$:

$$\vec{J} = \vec{L} + \vec{S} \tag{1.8}$$

For all but the heaviest atoms the ground state of a free atom with an unfilled shell is determined by three empirical rules known as *Hund's rules*:

1. The ground state will have the largest spin S that is consistent with the *Pauli Exclusion Principle.*

2. The ground state will have the largest total orbital angular momentum L that is consistent with both the first rule and the exclusion principle.

3. This rule determines the value of the overall total angular momentum number J, which can lie between $|L - S|$ and $L + S$. The $(2L+1)\times(2S+1)$ possible states have different energies that are determined by interactions of the form $\lambda \vec{L}\cdot\vec{S}$ which is known as Russel-Saunders coupling. The factor λ is positive for shells that are less than half filled, and negative for shells that are more than half filled. Thus J is given by the number N of electrons:

$$J = |L - S| \text{ for } N \leq 2l+1 \text{ and } J = L + S \text{ for } N \geq 2l+1$$

When J has a non-zero value, the atom or ion has a magnetic moment:

$$\vec{\mu} = -g\mu_B \vec{J} \tag{1.9}$$

with the absolute value:

$$\mu = g\mu_B \sqrt{J(J+1)} \tag{1.10}$$

where g is the *Landé spectroscopic factor* and is approximately:

$$g \approx 1 + \frac{J(J+1) + S(S+1) - L(L+1)}{2J(J+1)} \qquad (1.11)$$

In most cases, the energy separation between the ground-state level and the other levels are large compared to kT. For describing the magnetic properties of the ions at 0K, it is therefore sufficient to consider only the ground state characterized by the angular momentum quantum number J.

Two series of elements play a fundamental role in magnetism: the *3d* transition elements and the *4f* rare earths. These two series are important because the unfilled shells are not the outer shells and in solids the *3d* (respectively *4f*) shell can remain unfilled, leading to magnetism. In the case of the *4d* and *5d* series of elements, the magnetism is generally very weak. This is because the *4d* and *5d* shells are rather delocalized, allowing the participation of these electrons to the conduction band.

1.1.2 Classes of magnetic materials

Diamagnetism

Diamagnetism is a fundamental property of all matter, although it is usually very weak. It can be regarded as originating from the shielding currents induced by an applied field in the filled electron shells of ions. These currents are equivalent to an induced moment present on each of the atoms. The diamagnetism is a consequence of Lenz's law stating that if the magnetic flux enclosed by a current loop is changed by the application of a magnetic field, a current is induced in such a direction that the corresponding magnetic field opposes the applied field. The magnetic susceptibility of diamagnetic materials is negative and has no temperature dependence.

Paramagnetism

In the case of paramagnetic materials, some of the atoms carry intrinsic magnetic moments due to unpaired electrons in partially field orbitals, but the individual magnetic moments do not interact with each another. The magnetization is zero in the absence of an external magnetic field, like for diamagnetic materials. The presence of an external magnetic field leads to a partial alignment of the atomic magnetic moments in the direction of the field, resulting in a net positive magnetization and positive susceptibility. The efficiency of the field is opposed by the thermal effects which favour disorder of magnetic moments and tend to decrease the susceptibility. This results in a temperature dependent susceptibility, known as Curie's law:

$$\chi = \frac{C}{T} \qquad (1.12)$$

At normal temperatures and in moderate fields, the paramagnetic susceptibility is small, but larger than the diamagnetic contribution. Curie's law states that if the reciprocal values of the magnetic susceptibility, measured at various temperatures, are plotted versus the corresponding temperatures, one finds a straight line passing through the origin. The Curie constant can be estimated from the slope of this line and hence a value for the effective moment.

Ferromagnetism

Ferromagnetic materials have a non vanishing magnetic moment, or spontaneous magnetization, even in the absence of a magnetic field. Unlike paramagnetic materials, the atomic moments in these materials exhibit very strong interactions. These interactions are produced by electronic exchange forces and result in a parallel alignment of atomic moments. The exchange force is a quantum mechanical phenomenon due to the relative orientation of the spins of two electrons. The elements Fe, Ni, and Co and many of their alloys are typical ferromagnetic materials. Two distinct characteristics of ferromagnetic materials are their spontaneous magnetization and the existence of magnetic ordering temperature, called Curie temperature. The spontaneous magnetization is the net magnetization that exists inside a uniformly magnetized microscopic volume in the absence of a field. The magnitude of this magnetization, at 0K, is dependent on the spin magnetic moments of electrons. The magnetic ordering competes with thermal disorder effects and each material is characterized by a critical temperature (Curie temperature), which is a measure of the strength of magnetic interactions and is an intrinsic property of the material.
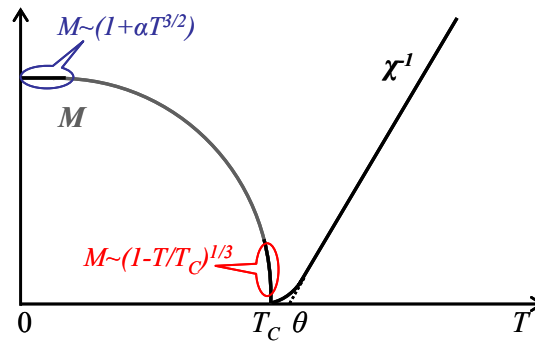

Fig. 1.1. The temperature dependence of the spontaneous magnetization M (T<T_C) and magnetic susceptibility $\chi(T > T_C)$ for a ferromagnetic system

At temperatures above the Curie temperature the thermal effects dominate and the material has a paramagnetic behaviour; below this temperature the magnetic interactions dominate and the material is magnetically ordered. Above the Curie temperature the magnetic susceptibility obeys the Curie-Weiss law:

$$\chi = \frac{C}{T - \theta_p} \tag{1.13}$$

where $\theta_p > 0$ is called the asymptotic or paramagnetic Curie temperature and differs from the Curie temperature due to the thermal fluctuations.

In addition to the Curie temperature and saturation magnetization, ferromagnets can retain a memory of an applied field once it is removed. This behaviour is called hysteresis and a plot of the variation of magnetization with magnetic field is called a hysteresis loop.

Antiferromagnetism

In the case of antiferromagnets, although there is no net total moment in the absence of the field, the magnetic interactions favour an antiparallel orientation of neighbouring moments. In a simple antiferromagnet, magnetic atoms can be divided into two sublattices with their magnetizations equal but antiparallel. The net magnetization is then zero at any temperature. The clue to antiferromagnetism is the behaviour of susceptibility above a critical temperature, called the Néel temperature (T_N). Above T_N, the susceptibility obeys the Curie-Weiss law for paramagnets but with a negative intercept indicating negative exchange interactions.
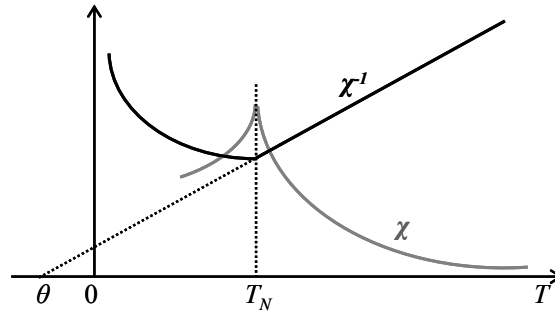

Fig. 1.2. The temperature dependence of the magnetic susceptibility for an antiferromagnet

Slight deviations from ideal antiferromagnetism can exist if the anti-parallelism is not exact. If neighbouring spins are slightly tilted (<1°) or canted, a very small net magnetization can be produced. This is called canted antiferromagnetism and hematite is a well known example. Canted antiferromagnets exhibit many of the typical magnetic characteristics of ferromagnets and ferrimagnets (e.g., hysteresis, Curie temperature).

Ferrimagnetism

A ferrimagnet is an antiferromagnet in which the different sublattice magnetizations are not equal, which results in a net magnetic moment. This requires non equivalent magnetic sublattices and/or atoms. Ferrimagnetism is therefore similar to ferromagnetism. It exhibits all the hallmarks of ferromagnetic behaviour spontaneous magnetization, Curie temperatures, and

hysteresis. However, ferromagnets and ferrimagnets have very different magnetic ordering. The temperature dependence of the magnetization in ferrimagnetic compounds is determined by the magnitude and sign of the coupling constants that describe the magnetic coupling between the different sublattices and between two moments residing on the same magnetic sublattice. Above the Curie temperature the reciprocal susceptibility is given by the Néel hyperbolic law:

$$\frac{1}{\chi} = \frac{1}{\chi_0} + \frac{T}{C} - \frac{\sigma}{T-\theta} \tag{1.14}$$

where C is the mean value of the Curie constant and χ_0, σ and θ are constants that depend on the nature of the sublattices present in the system.

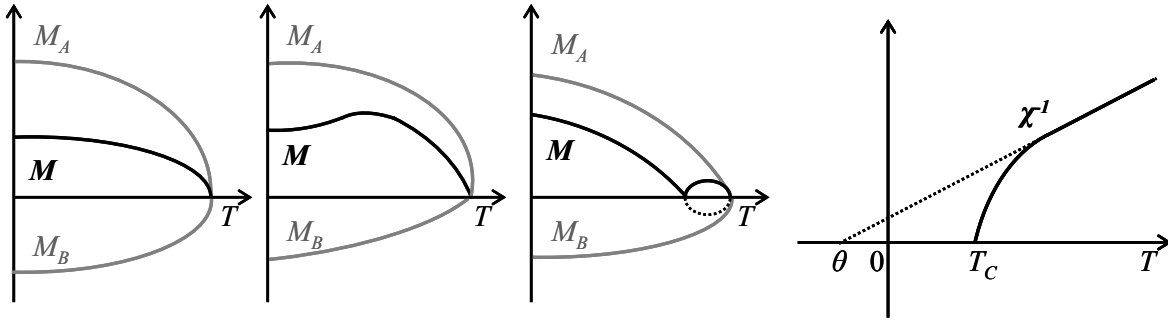Fig. 1.3. The temperature dependence of the spontaneous magnetization M (T<T$_C$) (several cases are presented) and magnetic susceptibility χ (T>T$_C$) for a ferrimagnetic system consisting of two sublattices A and B

1.2 Magnetic properties of metallic systems

There are several models in magnetism, but none that fully describes the magnetic behaviour for magnetically ordered materials. Although the molecular field theory gives an intuitive description for the most important physic properties of ferromagnetic materials (temperature dependence of spontaneous magnetization, specific heat and magnetic susceptibility behaviour at high temperatures), it fails to describe the low temperatures and critical regions. At very low temperatures the experimental results are best described by the spin waves theory.

1.2.1 Localized moments in solids

The magnetic interaction between localized moments, the magnetic coupling, determines the behaviour of a compound when placed in a magnetic field and may favor magnetic ordering. The magnetic coupling is usually described in terms of a model spin Hamiltonian, most often the Heisenberg Hamiltonian:

$$H = -\sum_{i,j} J_{ij} \vec{S}_i \vec{S}_j \tag{1.15}$$

9

where *i, j* can be restricted to run over all nearest neighbour or next nearest neighbour pairs of magnetic moments on account of the fact that the magnetic interaction is weak and decreases exponentially with distance. Positive values of the Heisenberg coupling constant *J* correspond to ferromagnetic coupling, negative ones to antiferromagnetic coupling. In *3d* based materials $J_{ij} \approx 10^2 \div 10^3 K$. A spin operator of this form was first deduced from the Heitler-London results by Dirac [1] and first extensively applied in the theory of magnetism by Van Vleck [2]. The universal use of the name Heisenberg Hamiltonian acknowledges his original discussion of the quantum mechanical concept of electron exchange and the introduction of the term *exchange integral* in his theoretical work on the helium atom [3]. A conceptually similar but not at all identical term appears in the work of Heitler and London to express the difference in energy between the singlet and triplet states in the hydrogen molecule.

When the magnetic orbitals of two neighbouring atoms are sufficiently extended to produce a direct overlap, there is an effective interaction between the spins of these atoms, called *direct exchange*. The origin of the *exchange interaction* is in the different energies for the parallel and antiparallel spin states as a result of the Pauli principle. This direct exchange, which occurs in *3d* intermetallic compounds, is the largest interatomic interaction and it is, in particular, responsible for the high ordering temperatures found in the ferromagnets used for most technological applications. The Slater-Néel curve illustrates the variation of this interaction as a function of interatomic distance and magnetic shell radius.
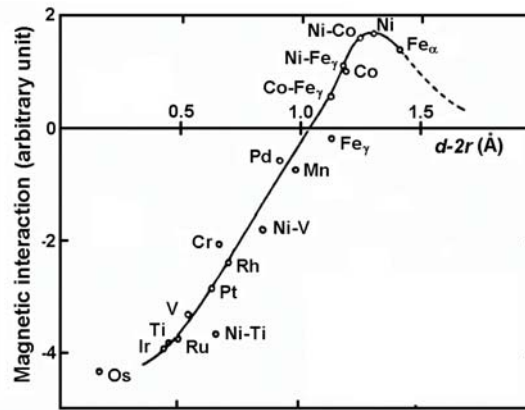

Fig. 1.4. Slater-Néel curve (d=distance between two atoms, r=magnetic shell radius)

When magnetic orbitals of two neighbouring atoms are too localized to overlap, as in the case for the *4f* series, the exchange process can occur through conduction electrons if the system is metallic. This leads to the *RKKY indirect exchange interaction*. If there are no conduction electrons, as in ceramics where magnetic atoms are separated by non-magnetic atoms like oxygen, the external electrons of the latter participate in covalent binding and mediate the

exchange interaction. This is the *superexchange interaction*. The term *superexchange* was introduced by Kramers [4] in 1934 in an early attempt to explain the magnetic interaction in anti-ferromagnetic ionic solids. The distance between the transition metal ions is generally far too large for direct magnetic interactions, as occur in metals, to be of any significance. Since the metal ions always have negative ions as nearest neighbours he proposed that these anions played an intermediary role in the interaction mechanism. A more elaborate and successful evaluation was carried out in 1959 by Anderson [5].

The Molecular Field Model

Pierre Weiss postulated the presence of a molecular field in his phenomenological theory of ferromagnetism in 1907 [6], long before its quantum-mechanical origin was known. The model proposed by Weiss is based on the powerful assumption that the fluctuations of molecular field with time and the dependence on the instantaneous values of the magnetic moments can be neglected. The origin of the Weiss molecular field was attributed by Heisenberg [7] to the quantum-mechanical exchange interaction between neighbouring atoms, usually written:

$$H_{exch} = -2\sum_{i<j} J_{ij} \vec{S}_i \vec{S}_j \tag{1.16}$$

where the summation extends over all spin pairs in the crystal lattice. The exchange constant J_{ij} depends, amongst other things, on the distance between the two atoms i and j considered. In most cases, it is sufficient to consider only the exchange interaction between spins on nearest-neighbour atoms. By considering Z magnetic nearest-neighbour atoms surrounding a given magnetic atom, the exchange Hamiltonian becomes:

$$H_{exch} = -2ZJ_{nn} \vec{S} \cdot \langle \vec{S} \rangle \tag{1.17}$$

where $\langle \vec{S} \rangle$ is the average spin of the nearest-neighbour atoms. This relation can be rewritten:

$$H_{exch} = -2ZJ_{nn}(g-1)^2 \vec{J} \cdot \langle \vec{J} \rangle \tag{1.18}$$

The atomic moment is related to the angular momentum by (Eq. 1.9), resulting in:

$$H_{exch} = \frac{-2ZJ_{nn}(g-1)^2 \vec{\mu} \cdot \langle \vec{\mu} \rangle}{g^2 \mu_B^2} = -\mu_0 \vec{\mu} \vec{H}_m \tag{1.19}$$

where:

$$\vec{H}_m = \frac{2ZJ_{nn}(g-1)^2 \langle \vec{\mu} \rangle}{g^2 \mu_B^2} \tag{1.20}$$

can be regarded as an effective field, the so-called molecular field, produced by the average moment $\langle \vec{\mu} \rangle$ of the Z nearest-neighbour atoms. If all the magnetic moments are identical, the magnetization of the system can be written $\vec{M} = N \langle \vec{\mu} \rangle$ and in consequence $\vec{H}_m$ is proportional to the magnetization:

$$\vec{H}_m = N_W \vec{M} \tag{1.21}$$

The constant N_W is called the molecular-field constant or the Weiss-field constant.

In the Weiss molecular filed theory the Curie temperature is given by:

$$T_C = \frac{N_W N \mu_0 g^2 J(J+1) \mu_B^2}{3 k_B} \tag{1.22}$$

and the magnetic susceptibility above T_C is given by:

$$\chi = \frac{N \mu_0 g^2 J(J+1) \mu_B^2}{3 k_B (T - T_C)} \tag{1.23}$$

Heisenberg assumed that the exchange integral between neighbouring atoms is positive and of appropriate order of magnitude. Subsequent attempts to calculate J for ferromagnetic transition metals from realistic atomic orbitals have failed to explain the sign and magnitude of J. In fact, the molecular field theory gives a grossly inadequate picture of the critical region, fails to predict spin waves at low temperatures, and even at high temperatures reproduces without error only the leading correction to Curie's law. Nevertheless the theory has been widely used and quoted and when confronted with a new situation (e.g., a particular complicated arrangement of spins on a crystal structure with several types of coupling) it probably offers the simplest rough way of sorting out the types of structures expected to arise. Also the molecular field theory is sometimes taken as starting point for more sophisticated calculations.

The Heisenberg model is actually justified when well-defined local atomic moments exist, like in the case of magnetic insulators and in the majority of rare-earth metals. In the former, the mechanism of exchange interaction is the superexchange which is usually antiferromagnetic, while in the latter indirect exchange interaction via the conduction electrons dominates.

1.2.2 Itinerant-electron magnetism

Opposite to the localized model is the itinerant (or band) model which considers that each magnetic carrier (electron or hole) is itinerant through the solid. In this case, the unpaired electrons responsible for the magnetic moment are no longer localized and accommodated in

energy levels belonging exclusively to a given atom, but move in the potential of other electrons and ions, and the corresponding atomic levels form energy bands. The extent of the broadening of the energy bands depends on the interatomic separation between the atoms. The ordered magnetic states, stabilized by electron-electron interactions, are characterized by the difference of the number of electrons (or holes) with up and down spins. The most prominent examples of itinerant-electron systems are metallic systems based on *3d* transition elements, with the *3d* electrons responsible for the magnetic properties, where the unfilled *d* shell is rather extended.

The Stoner Model

The simplest model of itinerant-electron magnetism is the Stoner model [8], which has mainly been used to account for the existence of ferromagnetism in itinerant systems. If the relative gain in the exchange interaction (the interaction of electrons via Pauli's exclusionary principle) is larger than the loss in kinetic energy, the spin up and spin down electron bands will split spontaneously. In the Stoner band model, the energies of the spin up and down electron bands are:

$$E_\uparrow(\vec{k}) = E(\vec{k}) - I\frac{n_\uparrow}{n}$$
$$E_\downarrow(\vec{k}) = E(\vec{k}) - I\frac{n_\downarrow}{n}$$
(1.24)

where $E(\vec{k})$ is the energy of the metal before exchange effects are included, $n_\uparrow$ and $n_\downarrow$ represent the number of electrons with spin up and spin down, and n is the number of electrons in the system ($N=n_\uparrow+n_\downarrow$). The Stoner parameter I describes the energy change due to electron spin correlations. The relative difference between the number of electrons occupying the spin up and spin down bands is:

$$R = \frac{n_\uparrow - n_\downarrow}{n}$$
(1.25)

which is proportional to the magnetization of the system.
In consequence:

$$E_\uparrow(\vec{k}) = \tilde{E}(\vec{k}) - \frac{IR}{2}$$
$$E_\downarrow(\vec{k}) = \tilde{E}(\vec{k}) + \frac{IR}{2}$$
(1.26)

where: $$\tilde{E}(\vec{k}) = E(\vec{k}) - I\frac{n_\uparrow + n_\downarrow}{2n}$$ (1.27)

The energy separation between the two bands is independent of the wave vector of an electron.

We can evaluate R using the Fermi-Dirac statistics, where:

$$n = \sum_{\vec{k}} f(\vec{k}) = \sum_{\vec{k}} \frac{1}{\exp\left(\dfrac{E(\vec{k}) - E_F}{k_B T}\right) + 1} \tag{1.28}$$

which gives

$$R = \frac{1}{n} \sum_{\vec{k}} \left[\frac{1}{\exp\left(\dfrac{\widetilde{E}(\vec{k}) - IR/2 - E_F}{k_B T}\right) + 1} - \frac{1}{\exp\left(\dfrac{\widetilde{E}(\vec{k}) + IR/2 - E_F}{k_B T}\right) + 1} \right] \tag{1.29}$$

Eq. (1.29) can have real solutions, which means that the system has a magnetic moment in the absence of an external magnetic field, and therefore is ferromagnetic. In order to find the condition for the existence of magnetic moments in the system, the following approximation is used:

$$f\left(x - \frac{\Delta x}{2}\right) - f\left(x + \frac{\Delta x}{2}\right) = -f'(x)\Delta x - \frac{2}{3!}\left(\frac{\Delta x}{2}\right)^3 f'''(x) \tag{1.30}$$

which leads to:

$$R = -\frac{1}{n} \sum_{\vec{k}} \frac{\partial f(\vec{k})}{\partial \widetilde{E}(\vec{k})} IR - \frac{1}{24} \frac{1}{n} \sum_{\vec{k}} \frac{\partial^3 f(\vec{k})}{\partial \widetilde{E}(\vec{k})^3} (IR)^3 \tag{1.31}$$

If $R>0$ the band is exchange split, which corresponds to ferromagnetism. Therefore the condition for the stability of a ferromagnetic state is:

$$-1 - \frac{I}{n} \sum_{\vec{k}} \frac{\partial f(\vec{k})}{\partial \widetilde{E}(\vec{k})} > 0 \tag{1.32}$$

Considering that around 0K: $-\dfrac{\partial f}{\partial \widetilde{E}} = \delta(\widetilde{E} - E_F)$, we can write:

$$\frac{1}{n} \sum_{\vec{k}} \frac{\partial f(\vec{k})}{\partial \widetilde{E}(\vec{k})} = \frac{V}{(2\pi)^3 n} \int d\vec{k} \left(\frac{\partial f}{\partial \widetilde{E}}\right) = \frac{V}{(2\pi)^3} \frac{1}{n} \int d\vec{k}\, \delta(\widetilde{E} - E_F) = \frac{1}{2} \frac{V}{n} N(E_F) \tag{1.33}$$

Thus a ferromagnetic state is realized for:

$$IN(E_F) > 1 \tag{1.34}$$

where $N(E_F)$ is the density of states at the Fermi energy per spin and volume.

The later condition is the Stoner criterion for ferromagnetism.

The conditions favouring magnetic moments in metallic systems are obviously: a large value of the exchange energy, but also a large density of state at the Fermi level. The density of states of the s and p electron bands is considerably smaller than that of the d band, which

explains why band magnetism is restricted to elements that have a partially empty d band. However, not all of the d transition elements show band ferromagnetism, as presented in Fig. 1.5.

For instance, in the *4d* metal Pd, the Stoner criterion is not met, although it comes very close to it. The only pure d metals that show band ferromagnetism under normal conditions are Fe, Co and Ni.

Two situations have to be considered in the case of itinerant-electron magnetism:
- if both the spin up and spin down bands are not completely filled up, the compound is a *weak ferromagnet;* this is the case for Fe metal
- if the spin up band is completely full, the compound is a *strong ferromagnet*; this is the case for Ni and Co metals

These terms are only definition and they do not do not imply that the spontaneous moments per

Fig. 1.5. a) the Stoner parameter,
b) the density of states at Fermi level,
c) the Stoner criterion [9]

3d atom or the magnetic ordering temperatures are higher in the former case than in the latter. Indeed, n Fe the magnetization is 2.4μ_B/Fe whereas in Co and Ni it is 1.9 and 0.6 respectively. The magnetization of the system at T≈0K is:

$$M = 2\mu_B^2 \frac{n}{V} \frac{N(E_F)}{1 - IN(E_F)} B$$ (1.35)

When *IN(E$_F$)* is barely larger than 1, the Stoner criterion is fulfilled but the magnetization is weak and we have the so-called *very weak itinerant ferromagnetism*.
The magnetic susceptibility is given by:

$$\chi = \frac{\chi_0}{1 - IN(E_F)}$$ (1.36)

where χ_0 is the Pauli susceptibility of free electrons. This is referred to as the Stoner enhancement of the susceptibility.

This itinerant electron model is consistent with the observed magnetizations per atom of Fe, Co, Ni, which are not integral multiples of the Bohr magneton per *3d* atom. However, the Stoner theory fails to explain the Curie-Weiss magnetic susceptibility observed in almost all ferromagnets. Calculated Curie temperatures for *3d* metals are too high in comparison to the
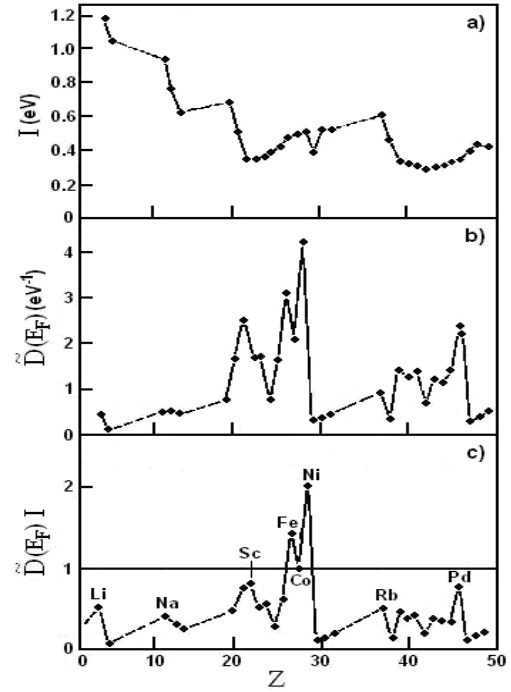
observed ones and the calculated anomalous entropy around the Curie temperature is too small to explain the observed values.

1.2.3 Local moments in metals

Both the localized model and itinerant model fail to fully describe the magnetic behaviour of magnetic transition metals. It is very clear that d electrons should be treated as localized electrons in magnetic insulator compounds and as correlated itinerant electrons in transition metals. Theoretical efforts since the 1950s have been concentrated on finding a way of reconciling the two mutually opposite pictures into a unified one, taking into account the effect of electron-electron correlation in the itinerant electron model. There have been two main directions in this attempt: one was to improve the Stoner theory by considering the electron-electron correlation, and the other was to start with the study of local moments in metals.

The picture of local moments in metals resolved the controversy over the two models. Van Vleck [10] discussed the justification of local moments, considering the importance of electron correlation in narrow d bands. An explicit model describing the local moments in metals was proposed by Anderson [11] on the basis of the Friedel picture of virtual bound states in dilute magnetic alloys [12].The Anderson concept of local moments in metals has been quite important in the development of the theory of ferromagnetic and antiferromagnetic metals. It may be possible in some cases to regard a metallic ferromagnet as consisting of local moments associated with the virtual bound states. Although in this case the local moment is not as well defined as in insulator magnets, an approximate Heisenberg-type picture can be used even in metals. The interaction between local moments in metals was studied by Alexander an Anderson [13] and by Moriya [14] on the basis of the Anderson model. Simple rules regarding the sign of the effective exchange coupling between neighbouring moments were obtained, which will be discussed later on. These rules and their generalizations for a pair of different atoms were successfully applied to explain various magnetic structures of numerous ferromagnetic and antiferromagnetic metals, intermetallic compounds and alloy.

Virtual bound state

The picture of local moments in metals is tied up with the concept of virtual bound states introduced by Friedel for dilute alloys [12]. Consider a transition metal impurity in a non-magnetic metallic host. The excess nuclear charge (the charge of the interstitial impurity or the change in charge if the impurity substitutes an atom in the matrix) displaces locally the mobile electrons until the displaced charge screens out the new nuclear charge. As the screening should

be perfect within the limits of classical physics, its radius should have atomic dimensions. The effect is a perturbing potential in addition to the periodic potential of the pure matrix at the impurity position.

Alloys with transitional impurities often exhibit peculiar properties that are related to the presence of d bound states or virtual bound states. In transition metals the screening occurs on the impurity atom itself and thus two impurity atoms do not interact even when nearest neighbours. In Fig. 1.6 is presented the case of a transition metal atom with a spherical potential (pictured by the dashed curve) that accommodates a d bound state characterized by the quantum number l. If the perturbing potential reduces the potential of the impurity from the value of the dashed curve to the actual value corresponding to the continuous curve, the bound state increases in energy and merges into the conduction band of the host. The interaction of the d electron with the conduction electrons leads to an admixture or hybridization between the s states of the solute and the d states of the impurity. As a result there will no longer be a localized bound d state, but a wave packet of width w localized at the transition element position around E_0, producing a virtual bound state.
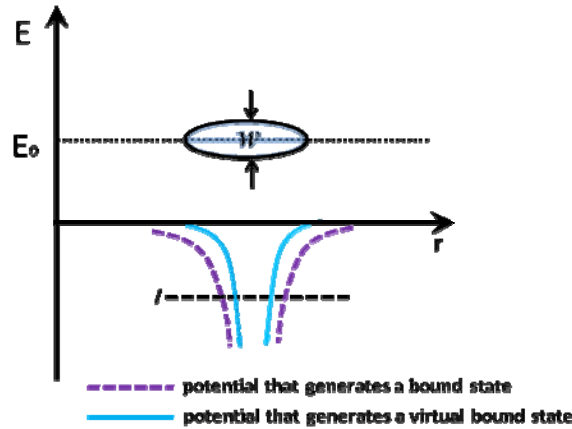
Fig.1.6. Real bound state and virtual bound state in energy versus space diagram [12]

The width w of the virtual bound level decreases for increasing l (for l=0 it is so large that virtual s levels have no physical significance) and for a give l it is roughly proportional to E_0. The width of the virtual d states for transitional impurities in Al is around 4eV, due to the high Fermi energy, while in Cu matrix is around 2eV, if the conductive electrons are treated as free. The splitting within the d shell due to the exchange interactions can only occur if the energy of splitting is larger than the width w of the states. The condition considering Hund's rule is:

$$w \leq p\Delta E \qquad (1.37)$$

where p is the number of electrons (if less than 5) or holes (otherwise) in the d shell and ΔE is the average energy gained when two d electrons with antiparallel spins are put with their spins

parallel. From atomic spectra ΔE is estimated from 0.6 to 0.7 eV. As $p \leq 5$, the exchange splitting is impossible in Al. For Cu matrix the exchange splitting occurs for $p \geq 3$, thus for impurities like Fe, Mn or Cr, but not for Ni or Co.

The interaction with the conduction electrons can be also regarded as a scattering problem. Consider an impurity atom embedded in an electron gas. Assuming the impurity potential to be spherically symmetric around the origin, we have the problem of an electron scattered by the impurity potential. We are interested in a change in the density of states induced by the impurity atom. The transition metal atom introduces an excess charge Z, which must be screened by the same amount of electronic charge, as required by the charge neutrality condition. The redistribution of the conduction electrons results in a change in density of states in the energy range ε to $\varepsilon + d\varepsilon$.

$$\Delta N(k)\delta k = \frac{1}{\pi}\sum_{l,\sigma}(2l+1)\left(\frac{d\eta_{l\sigma}}{d\varepsilon}\right)\left(\frac{d\varepsilon}{dk}\right)\delta k = \frac{1}{\pi}\sum_{l,\sigma}(2l+1)\left(\frac{d\eta_{l\sigma}}{d\varepsilon}\right)\delta\varepsilon \equiv \Delta N(\varepsilon)\delta\varepsilon \qquad (1.38)$$

where $\eta_{l\sigma}$ is the phase shift for the lth partial wave function of a scattered electron with spin σ. The total excess electronic charge is obtained by integrating up to the Fermi level and must be equal to the extra charge of the impurity Z. Thus the following Friedel sum arises:

$$Z = \frac{2}{\pi}\sum_{l}(2l+1)\eta_{l}(E_F) \qquad (1.39)$$

where the factor 2 is due to the spin degeneracy.

When an energy level of the impurity atom is close to the energy of an incident electron, resonance scattering takes place and the phase shift varies very rapidly with energy. For a transition metal impurity atom the d-wave ($l=2$) scattering shows this character. This means that the bound state of the impurity atom, when introduced in a metal, resolves into scattered states within a relatively small energy range. The change in the density of states due to the d-wave scattering from an impurity atom is given from the term with $l=2$ in Eq. (1.38) as:

$$\Delta N_2(\varepsilon) = \frac{5}{\pi}\sum_{\sigma}\frac{d\eta_{2\sigma}}{d\varepsilon} \qquad (1.40)$$

When this has a fairly sharp peak it is called a virtual bound state.

By taking account of the exchange interaction between d electrons in the impurity atom, the virtual bound state can split under favourable conditions. The condition may be given by:

$$J\Delta N_2(E_F) > 1 \qquad (1.41)$$

where J is the intra-atomic exchange energy. When there is a local moment of size M, the phase shifts are derived from:

$$M = \frac{5}{2\pi}(\eta_{2\uparrow} - \eta_{2\downarrow})$$

$$Z = \frac{5}{2\pi}(\eta_{2\uparrow} + \eta_{2\downarrow})$$

(1.42)

By using these relations Friedel gave a systematic explanation of the residual resistivity due to 3d-metal impurities in Al and Cu. In the former case impurity atoms have no local moment while in the latter some of them have local moments.

The Anderson Model

The "Anderson model" [11] is the simplest one which provides an electronic mechanism for the existence of local moments. Assuming that the local moment exists, this means that a d-shell state φ_d on the impurity atom of spin up is full and of spin down is empty. Since only a spin down electron can be added, an electron of spin down will see the repulsion of the extra-spin electron, while the electrons of spin-up will not. Thus if the unperturbed energy of the spin-up state is situated at E_d below the Fermi surface, the energy of the spin-down state will be $-E_d+U$, where U is the repulsive d-d interaction and must lie above the Fermi level because we assumed that this state is empty. The effect of covalent admixture of free-electron states with the d states is to reduce the number of electrons in the spin-up state and to increase the number of the spin-down state, which leads to a reduction of the total moment. The changes in the number of d electrons are such as to decrease the difference U between the spin-up and spin-down energies: -E_d moves up to $-E_d+\delta nU$ and $-E_d+U$ moves down to $-E_d+(1-\delta n)U$. δn depends on the density of the free ions, the strength of the electron admixture and on the energy difference between up and down states. If, by a change of one of these parameters, is increase, the energy difference between decreases. The situation may become completely unstable, resulting in the disappearance of the local magnetic moment.

In order to deal with the local moment in metals more explicitly, Anderson introduced a mathematical model, in which he inserted the vital on-site exchange term U, and characterized the impurity atom by an additional orbital φ_d, with occupancy $n_{d\sigma}$ and creation operator $c_{k\sigma}^+$ over and above the free electron states near the Fermi surface of the metal. The Hamiltonian is expressed by:

$$H = H_{0f} + H_{0d} + H_{corr} + H_{sd}$$

(1.43)

H_{0f} is the unperturbed energy of the free electron system in second-quantized notation:

$$H_{0f} = \sum_{k\sigma} \varepsilon_k n_{k\sigma}$$

$$n_{k\sigma} = c^{+}_{k\sigma} c_{k\sigma}$$

(1.44)

where ε_k is the energy of the free electron state of momentum k.

The second term is the unperturbed energy of the d states on the impurity atom:

$$H_{0d} = E_d(n_{d\uparrow} + n_{d\downarrow})$$

(1.45)

The third term is the repulsive energy among the d functions:

$$H_{corr} = U n_{d\uparrow} n_{d\downarrow}$$

(1.46)

The fourth essential part of the Hamiltonian is the s-d interaction term:

$$H_{sd} = \sum_{k,\sigma} V_{dk}(c^{+}_{k\sigma} c_{d\sigma} + c^{+}_{d\sigma} c_{k\sigma})$$

(1.47)

where V_{dk} is the matrix element for the covalent admixture between the impurity state and the conduction band.

Anderson obtained by Green's function methods the density distribution of the d state:

$$N_{d\sigma}(\varepsilon) = \frac{1}{\pi} \frac{\Delta}{(\varepsilon - E_\sigma)^2 + \Delta^2}$$

(1.48)

where Δ is the "width parameter" of the virtual state, defined by:

$$\Delta = \pi \left\langle V^2 \right\rangle_{av} N(\varepsilon)$$

(1.49)

and:

$$E_\sigma = E_d + U\left\langle n_{d-\sigma} \right\rangle$$

(1.50)

In Fig. 1.7 are shown the two virtual states in terms of their distributions $N_{d\sigma}(\varepsilon)$ from Eq. (1.48) centered around the self-consistent energies E_σ.
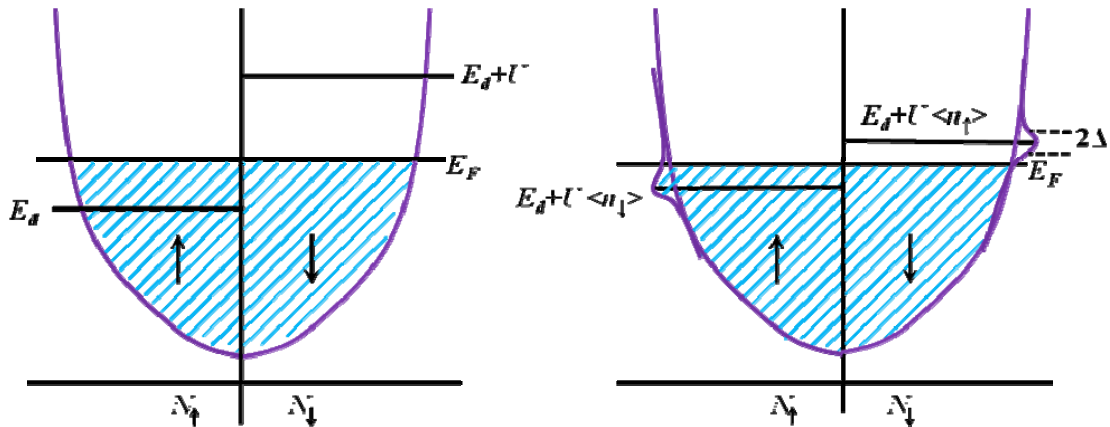
Fig.1.7. Density of state distributions in a magnetic state. The arrows indicate the spin up and spin down. The "humps" at $E_d+U<n_\downarrow>$ and $E_d+U<n_\uparrow>$ are the virtual d levels of width 2Δ, for up and down spins, respectively. [11]

In order to determine the number of d electrons of a given spin σ, we integrate Eq. (1.48) up to the Fermi energy E_F:

$$\langle n_{d\sigma} \rangle = \frac{1}{\pi} \int_{-\infty}^{E_F} \frac{\Delta}{(\varepsilon - E_\sigma)^2 + \Delta^2} d\varepsilon = \frac{1}{\pi} \cot^{-1}\left(\frac{E_\sigma - E_F}{\Delta} \right) \tag{1.51}$$

Thus:

$$\langle n_{d\uparrow} \rangle = \frac{1}{\pi} \cot^{-1}\left(\frac{E_d - E_F + U\langle n_{d\downarrow} \rangle}{\Delta} \right)$$

$$\langle n_{d\downarrow} \rangle = \frac{1}{\pi} \cot^{-1}\left(\frac{E_d - E_F + U\langle n_{d\uparrow} \rangle}{\Delta} \right) \tag{1.52}$$

To show the possibilities inherent in these equations, Anderson introduced two dimensionless parameters:

1. $y = \dfrac{U}{\Delta}$ (the ratio of the Coulomb integral to the width of the virtual state)

When y is large, correlation is large and there is localization in the system, while y corresponds to the "normal" non-magnetic state.

2. $x = \dfrac{E_F - E_d}{U}$

This parameter is also useful: $x=0$ indicates that the empty d state is right at the Fermi level, while $x=1$ puts E_d+U at the Fermi level. $x=1/2$, where E_d and E_d+U are symmetrically disposed about the Fermi level, is the most favourable case for magnetism. In fact $0 \leq x \leq 1$ is the only magnetic range.   Inserting these parameters in Eq. (1.52), leads to:

$$\pi n_{d\uparrow} \cong \cot^{-1}[y(n_{d\downarrow} - x)]$$

$$\pi n_{d\downarrow} \cong \cot^{-1}[y(n_{d\uparrow} - x)] \tag{1.53}$$
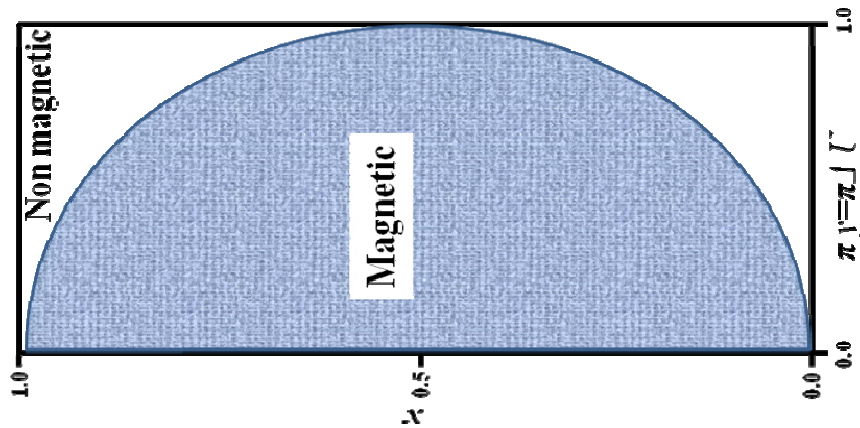
Fig. 1.8. Regions of magnetic and non-magnetic behaviour [11]

There are several special cases:

A. Magnetic limit: $y \gg 1$, x is not small or too near to 1

Then $\cot^{-1}$ is either close to 0 or to π, and $n_{d\sigma}$ is near 0 or 1. By assuming $n_{d\uparrow} \sim 1$ and $n_{d\downarrow} \sim 0$:

$$\pi n_{d\uparrow} \cong \pi - \frac{1}{y(x - n_{d\downarrow})} \quad \text{and} \quad \pi n_{d\downarrow} \cong \frac{1}{y(n_{d\uparrow} - x)}$$

which can be approximately solved to obtain:

$$m = n_{d\uparrow} - n_{d\downarrow} \cong 1 - \frac{1}{\pi y x(1-x) - 1} \tag{1.54}$$

B. Non-magnetic case: $n_{d\uparrow} = n_{d\downarrow} = n$. In this case: $\cot \pi n = y(n - x)$

   ◦ n not far from 1/2, so: $\cot \pi n = y(1/2 - x)$

$$n \cong \frac{1}{2} \frac{1 + 2xy/\pi}{1 + y/\pi} \tag{1.55}$$

Since n tends to take on the value 1/2, the effective energy level stays near the Fermi level

   ◦ y large, x near 0 (or 1): $\cot \pi n \cong 1/\pi n$ and $y(n - x) \cong 1/\pi n$

$$n \cong (xy)^{-1/2} + x/2 + \dots \tag{1.56}$$

C. The Transition Curve from magnetic to non-magnetic behaviour is characterized by $n_{d\uparrow} = n_{d\downarrow}$ and:

$$y_c = \pi / \sin^2 \pi n_c \tag{1.57}$$

These results are summarized in Fig.1.8 that shows the transition curve as a function of x and π/y.

The condition for the appearance of a local moment in the Anderson model is given by:

$$\pi \Delta / U < 1 \tag{1.58}$$

In order to get a feeling for orders of magnitude, in the iron group U is expected to be around 10eV. The density of states is fairly widely variable, from 0.1eV^{-1} (Cu) to twice or three times that for *d*-band metals. In the case of Cu, V_{av} is estimated around 2-3eV, thus $\Delta = \pi < V^2 >_{av} N(\varepsilon)$ runs of the order 2-5eV. This shows that the transition $U/\Delta = y = \pi$ occurs right in the interesting region and it is perfectly possible to have a transition from magnetic to non-magnetic localized states due to changes in the density of states or motion of the Fermi level.

The best example of local moment systems are the Heusler alloys [15,16]. Although they are metals, these intermetallic compounds have localized magnetic properties and are ideal model systems for studying the effects of both atomic disorder and changes in the electron concentration on magnetic properties. In Heusler alloys such as Pd_2MnSn, Ni_2MnSn, Cu_2MnAl, etc., manganese atoms are spatially separated from each other, (the distance between two Mn

atoms is more than 4Å) and are believed to carry well-defined local moments of around $4\mu_B$/Mn. The local moment picture for several Heusler alloys was corroborated by neutron scattering and static susceptibility measurements [17-20]. The magnetic properties of these compounds are governed by an indirect exchange coupling of RKKY type, mediated by the conduction electrons, between the Mn moments responsible for the ferromagnetic order.

Other systems close to the local moment limit are: $MnPt_3$, $MnPd_3$, $FePd_3$, $FePt_3$ [21-28]. The dominant interaction responsible for the magnetic order in these compounds is the nearest-neighbor Mn-Mn interaction. $MnPt_3$ and $FePd_3$ have ferromagnetic behaviour below T_C=390K and 530K, respectively. The values for the moments at low temperature are $3.64\mu_B$/Mn and $0.26\mu_B$/Pt in $MnPt_3$ and $2.68\mu_B$/Fe and $0.34\mu_B$/Pd in $FePd_3$. If the near-neighbor Mn – Mn distance is smaller than ~3Å [29], there is an overlap of the 3d orbitals and the interaction is antiferromagnetic. $MnPd_3$ and $FePt_3$ are antiferromagnets with the Néel temperature of 200K and 170K, respectively. The values for the moments at low temperature are $4\mu_B$/Mn and $0.2\mu_B$/Pd in $MnPd_3$ and $3.3\mu_B$/Fe and 0 for Pt in $FePt_3$. In view of the existing experimental results it is likely that there are fairly well-defined *3d* local moments (in Anderson's sense) on Mn and Fe atoms in these materials that couple with the itinerant *4d* or *5d* electrons of Pd or Pt.

Interaction between local moments in metals

When there are local moments in Anderson's sense, ferromagnetism or antiferromagnetism is destroyed by thermal excitations of spin rotations and there are disordered local moments above T_C. The interaction between a neighbouring pair of the same kind of atoms was studied by Alexander and Anderson [13] using the Anderson model, by extending the kinetic superexchange and double exchange mechanisms [5] to a pair of virtual bound states. This theory was generalized by Moriya [14] to 5-fold degenerate local orbitals and to different species of atoms. The exchange energy is given by:

$$E_{ex} = -\frac{V^2}{\Delta}(F_{ferro} - F_{antiferro}) \qquad (1.59)$$

$$F = F_\uparrow + F_\downarrow$$

with:

$$F_\sigma = -\Delta\frac{n_{1\sigma} - n_{2\sigma}}{E_{1\sigma} - E_{2\sigma}} \qquad (1.60)$$

where $E_{j\sigma}$ is the Hertree-Fock energy level and $n_{j\sigma}$ is the occupation number of electrons of the atomic orbitals (virtual bound state) with spin σ and of the *j*th atom, Δ is the width of the virtual bound state, and $V^2 = \sum_{m'} V_{mm'}^{12} V_{m'm}^{21}$, *m* and *m'* specifying one of the 5 degenerate orbitals, is the

mean-square transfer integral per orbital and is assumed to be independent of m. For a virtual bond state with a Lorentzian shape the number of occupied electrons $n_{j\sigma}$ is given from $(E_{j\sigma}-\varepsilon_F)/\Delta$ and thus F_σ is function of $n_{1\sigma}$ and $n_{2\sigma}$ only.

The gain in kinetic energy due to covalent transfer between two atoms is given by the second order perturbation and may be evaluated by:

$$\Delta\varepsilon = -V^2 \sum_\sigma n_{1\sigma} \frac{1-n_{2\sigma}}{\Delta E_{12}^\sigma} \tag{1.61}$$

where E_{12}^σ is the average of the excitation energy.

In his systematic study Moriya points out that the sign of the interaction between the local neighbouring local moments is primarily determined by the occupation fraction of the localized d-orbitals:

- when each atomic d-shell is nearly half-filled the coupling between the local moments is antiferromagnetic

- when the occupied or empty fraction of each atomic d-shell is small the coupling between the local moments is ferromagnetic

The sign of the induced spin polarization of neighbouring atoms is also governed by the same rules. To show how these rules arise, we show in Fig. 1.9 sketches of the densities of exchange-split virtual bond states for pairs of neighbouring atoms [30].
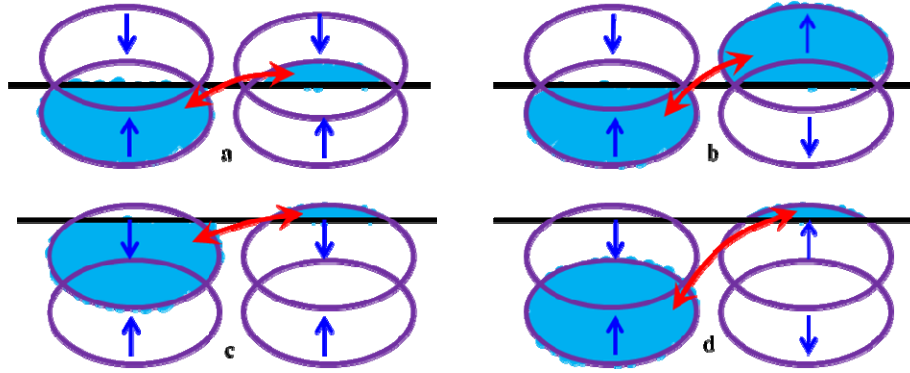
Fig. 1.9. Mechanism for the interaction between a pair of local moments associated with virtual bound states. The vertical direction is taken for energy and the horizontal lines represent the Fermi level. The arrows indicate the spin up and spin down. (a,b) half-filled case. (c,d) nearly filled virtual bound states [30]

It is now clear that for nearly half-filled virtual bound states the antiparallel pair has lower energy that the parallel pair since the former has a larger number of intermediate states as shown by the shaded area (Fig. 1.9 a,b). On the other hand, when the virtual states are nearly

filled (Fig. 1.9 c,d), the difference in excitation energy is more important and the parallel pair has lower energy.

These simple rules have been remarkably successful in qualitatively interpreting magnetic properties of a number of magnetic metals, alloys and intermetallic compounds. Furthermore, if the effective interatomic exchange energy is evaluated by properly estimating the width of the virtual bound state and the transfer integral from the observed or calculated d-band width, fairly god values are be obtained for the Curie or Néel temperatures.

1.2.4 Self-Consistent Renormalization (SCR) Theory of spin fluctuations of ferromagnetic metals

The necessity of self-consistent renormalization is a natural consequence of logical considerations toward a consistent theory beyond Hartree-Fock-random phase approximation (HF-RPA). Another motivation was the observation of very good Curie-Weiss (CW) susceptibilities in weakly ferromagnetic metals such as $ZrZn_2$ and Sc_3In [31,32], where the local moment picture is clearly inadequate and the HF-RPA theory cannot explain the CW law consistently.

A self-consistent treatment needs to calculate the dynamical susceptibility $\chi(q, \omega)$ and the free energy at the same time so that the static long-wavelength limit of the dynamical susceptibility agrees with that calculated from the renormalized free energy through $\partial F(M)/\partial M = h$, $\partial^2 F(M)/\partial M^2 = -\left[\partial^2 F(h)/\partial h^2\right]^{-1} = 1/\chi$. Such a theory was postulated by Moriya and Kawabata [33]. The formally exact expression for the dynamical susceptibility is considered to

be: $\chi \overline{M} \overset{+}{I}(q,\omega) = \dfrac{\overline{\chi M} \overset{+}{I}(q,\omega)}{1 - I\overline{\chi M} \overset{+}{I}(q,\omega)} = \dfrac{\chi \overline{M} \overset{+}{0}(q,\omega)}{1 - I\chi \overline{M} \overset{+}{0}(q,\omega) + \lambda_{MI}(q,\omega)}$ (1.62)

where $\overline{\chi M} \overset{+}{I}(q,\omega)$ is defined by a set of irreducible bubble diagrams each of which cannot be separated into two pieces each with an external vertex by removing an interaction vertex. Although calculating $\overline{\chi}(q,\omega) = \chi_0(q,\omega)/\left[1 + \lambda(q,\omega)\right]$ is possible within certain approximations, one can simplify the treatment by taking advantage of the long-wavelength approximation which is valid in a weakly ferromagnetic case.

Under an external magnetic field h (in energy units), the following general relations hold:

$$\partial F(M,I)/\partial M = \partial F_0(M,T)/\partial M - 2IM + \partial \Delta F(M,T)/\partial M - h = 0$$

$$1/\chi \overline{M} \overset{+}{I}(0,0) = \left[1 + \lambda_{MI}(0,0)\right]/\chi \overline{M} \overset{+}{0}(0,0) - I = h/2M$$

25

These yield $\lambda_{MI}(0,0) = \dfrac{\chi \overline{M}\,\overset{+}{0}}{2M}\left(\dfrac{\partial F_0(M,T)}{\partial M} + \dfrac{\partial \Delta F(M,T)}{\partial M}\right) - 1$ 　　　　(1.63)

For long-wavelength components one can approximate $\lambda_{MI}(q,\omega) \cong \lambda_{MI}(0,0)$. Then we need only

to solve (1.63) and $\Delta F(M,T) = T\displaystyle\sum_m \sum_q \int_0^I dI\left[\chi \overline{M}\,\overset{+}{I}(q,i\omega_m) - \chi \overline{M}\,\overset{+}{0}(q,i\omega_m)\right]$ with (1.62)

$\lambda_{MI}(0,0)$. For this purpose we still need more approximations in evaluating ΔF and $\partial \Delta F / \partial M$.

Using (1.62) in $\Delta F(M,T) = T\displaystyle\sum_m \sum_q \int_0^I dI\left[\chi \overline{M}\,\overset{+}{I}(q,i\omega_m) - \chi \overline{M}\,\overset{+}{0}(q,i\omega_m)\right]$ and neglecting

$\partial \lambda_{MI}/\partial I$ and $\partial \lambda_{MI}/\partial M$ compared with $\chi \overline{M}\,\overset{+}{0}(0,0)$ and $I\partial \chi \overline{M}\,\overset{+}{0}(0,0)/\partial M$, respectively, give

$$\Delta F(M,T) = T\sum_m \sum_q \left[\ln\left(1 - I\chi_{M0} + \lambda + I\chi_{M0}\right)\right]$$

$$\partial \Delta F(M,T)/\partial M = -T\sum_m \sum_q \left[\frac{I(I\chi_{M0} - \lambda)\partial I\chi_{M0}/\partial M}{1 - I\chi_{M0} + \lambda}\right] \qquad (1.64)$$

with $\chi M0 = \chi \overline{M}\,\overset{+}{0}(q,i\omega_m)$, $\lambda = \lambda MI(q,i\omega_m)$.

This approximation should be reasonable in weakly ferromagnetic metals where the amplitude of spin fluctuation is small, so thus $\lambda \ll I\chi M0 \sim 1$. On the other hand, note that λ is important in the denominator in (1.64) since $1 - I\chi M0(0,0)$ is very small. A detailed analyze of SCR theory for T> Tc and T < Tc was made by Moriya [34].

1.3 Photoelectron spectroscopy

Regarded today as a powerful surface spectroscopic technique, the *photoelectron spectroscopy* (PES) strikes its roots over more than a century ago. In 1887 W. Hallwachs and H. Hertz discovered the external photoelectric effect [35, 36] and in the following years refined experiments by J. J. Thomson led to the discovery of the electron, thus elucidating the nature of photo–emitted particles [37]. In 1905 A. Einstein postulated the quantum hypothesis for electromagnetic radiation and explained the systematic involved in experimental results [38]. By the early sixties C.N. Berglund and W. E. Spiecer extended the theoretical approach and presented the first model of photoemission [39]. In the same period a group conducted by K.Siegbahn in Sweden reported substantially improvements on the energy resolution and sensitivity of so–called β–spectrometers. They used X–rays ($h\upsilon \approx 1500$ eV) and managed to improve the determination of electron binding energies in atoms. Chemical shifts of about 1 eV

became detectable [40–42]. The new technique was accordingly named *Electron Spectroscopy for Chemical Analysis* (ESCA). The seventies marked the full recognition of technique's potential as a valuable tool for the surface analysis. Accurate data on the mean free path of the slow electrons were obtained and *ultra–high vacuum* (UHV) instruments became commercially available. More on the historical development of the photoelectron spectroscopy can be found in [43].

1.3.1. Physical principles of the technique

A PES experiment is schematically presented in Fig. 1.10. Incident photons are absorbed in a sample and their energy may be transferred to the electrons. If the energy of photons is high enough the sample may be excited above the ionization threshold which is accomplished by photoemission of electrons. Their kinetic energy is measured and the initial state energy of the electron before excitation can be traced back. Depending on the energy of incident radiation, the experimental techniques are labeled as: *Ultra–Violet Photoelectron Spectroscopy* or UPS ($h\upsilon$ < 100 eV), *Soft X–ray Photoelectron Spectroscopy* or SXPS (100 eV < $h\upsilon$ < 1000 eV) and *X–ray Photoelectron Spectroscopy* or XPS ($h\upsilon$ > 1000 eV).
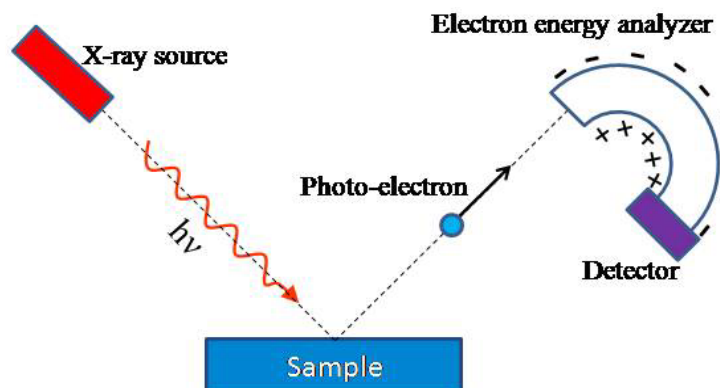
Fig. 1.10. Schematic representation of a PES experiment

In practical XPS, the most used incident X–rays are Al Kα (1486.6 eV) and Mg Kα (1253.6 eV). The photons have limited penetrating power in a solid on the order of 1–10 micrometers. However the escape depth of the emitted electrons is limited to some 50 ˚A. This characteristic makes XPS to an attractive surface science tool.

For a free atom or molecule, the energy conservation before and after photoemission is given by:

$$E_{in} + h\upsilon = E_{kin} + E_{fin} \tag{1.65}$$

where E_{in} and E_{fin} are the total initial and final energies of the atom or molecule before and after photoemission, respectively, $h\upsilon$ is the photon energy and E_{kin} is the photoelectron kinetic energy. The binding energy (E_b) for a given electron is defined as the energy necessary to remove the electron to infinity with zero kinetic energy. Therefore, one can write:

$$h\upsilon = E_{kin} + E_b \tag{1.66}$$

In eq. (1.66) the vacuum level is considered as reference level since it corresponds to a free atom (molecule). For the case of solids, the spectrometer and the solid are electrically connected in order to keep the system at a common potential during photoemission. Being connected, the Fermi levels of the spectrometer and solid become the same, as shown in Fig. 1.11 for a metal. Therefore, the kinetic energy of the photoelectron leaving the solid surface (E_{kin}) will be modified by the field ($\Phi - \Phi_s$) in such a way that in spectrometer one measures a photoelectron kinetic energy:

$$E'_{kin} = E_{kin} - (\Phi - \Phi_s) \tag{1.67}$$

where Φ and Φ_s [44] are the work functions of the solid and spectrometer, respectively.
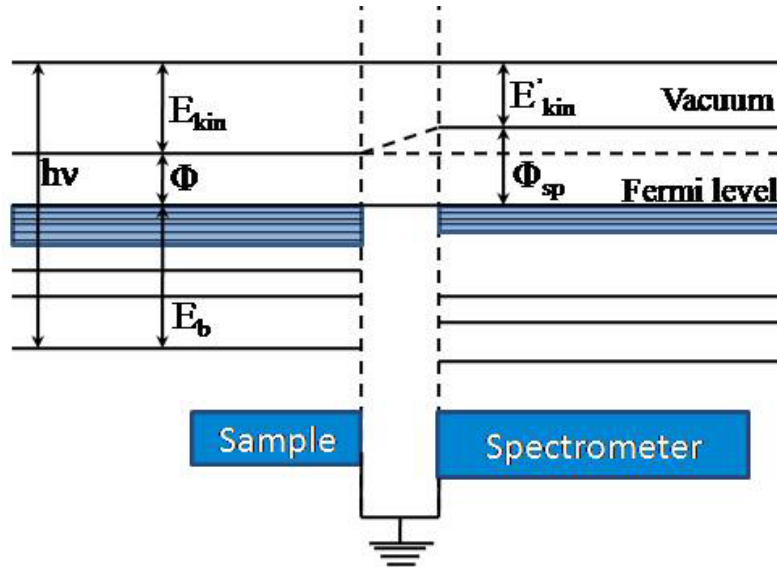
Fig. 1.11. The energy levels diagram for a solid electrically connected to a spectrometer

The binding energy for the metallic solid relative to the Fermi level is then given by:

$$E_b = h\nu - E'_{kin} - \Phi_s \tag{1.68}$$

In case of semiconducting and insulating samples, the assigning of the zero binding energy may be even more complicated and the calibration of zero binding energy is performed with reference to some known line of an element in the sample with known valence state.

The XPS spectrum illustrates the number of electrons (recorded with the detector) versus their kinetic energy (measured by using the electron analyzer). For practical purposes it is generally preferred to use the binding energy as abscissa [45]. This is convenient since the kinetic energy depends on the energy of the incident radiation and the binding energies are alone material specific.

1.3.2 Theory of photoelectron spectroscopy

A rigorous theoretical description of the photoelectron spectroscopy implies a full quantum–mechanical approach. In this section important aspects underlying XPS are sketched focusing on the main approximations and models.

Let us consider a system containing N electrons which is described by the wave function $\Psi_{in}(N)$ and the energy $E_{in}(N)$. Absorption of a photon with the energy $h\upsilon$ causes the excitation into a final state described by $\Psi_{fin}^{k}(N)$ and $E_{fin}^{k}(N)$ [46]:

$$\overset{initial\_state}{\Psi_{in}(N); E_{in}(N)} \xrightarrow{h\upsilon} \overset{final\_state}{\Psi_{fin}^{k}(N); E_{fin}^{k}(N)} \tag{1.69}$$

where k labels the electron orbital from which the photoelectron has been removed. The transition probability (which dictates the photocurrent intensity) obeys the Fermi's golden rule [47]:

$$w = \frac{2\pi}{\hbar}\left|\left\langle \Psi_{in}(N)\left|H\right|\Psi_{fin}^{k}(N)\right\rangle\right|^{2}\delta(E_{fin}^{k}(N) - E_{in}(N) - h\upsilon \tag{1.70}$$

where the δ function ensures the energy conservation during transition and H is the interaction operator. The eq. (1.70) is satisfied when the perturbation H applied to the system is small. The interaction operator can be written as:

$$H = \frac{e}{2m_{e}c}\left(Ap + pA\right) - e\varphi + \frac{e^{2}}{2m_{e}c^{2}}AA \tag{1.71}$$

Here e and m_{e} denote the electron charge and mass, c is the light speed, A and φ are the vector potential operator and respectively the scalar potential of the exciting electromagnetic field and p is the momentum operator of the electron. A simplified form of the interaction Hamiltonian can be obtained by assuming that the two–phonon processes can be neglected (the

term AA), that the electromagnetic field can be described in the dipole approximation and choosing $\varphi = 0$ [48]:

$$H = \frac{e}{m_e c} A_0 p \tag{1.72}$$

where A_0 is the constant amplitude of electromagnetic wave. The dipole approximation is valid if the radiation wave–length is much larger than atomic distances, which is correct for the visible and ultraviolet regions of the electromagnetic spectrum. Mathematically the vector potential operator can be then written as $A(r,t) = A_0 e^{(kr-\omega t)}$. The approximation interaction Hamiltonian for the structure of final state is more subtle [48, 49].

For high energy spectroscopy it can be assumed that the outgoing electron is emitted so fast that it is sufficiently weak coupled to the $(N - 1)$ electron ion left behind. This is the so–called *sudden–approximation* which is actually valid in the keV region of energies. For lower energy regions its applicability has certain restrictions [50, 51]. The final state can be split up in two configurations:

$$\overset{initial\_state}{\overbrace{\Psi_{in}(N); E_{in}(N)}} \overset{h\upsilon}{\longrightarrow} \overset{final\_state\_ion}{\overbrace{\Psi_{fin}^k(N-1); E_{fin}^k(N)}} + \overset{photoelectron}{\overbrace{\xi^k(1); E_{kin}^k}} \tag{1.73}$$

where $\xi^k(1)$ is the wave function of the photoelectron.

The energy conservation during photoemission simply yields:

$$E_{in}(N) + h\upsilon = E_{fin}^k(N-1) + E_{kin}^k + \Phi \tag{1.74}$$

Here Φ is the work function. According to eq. (1.68) the binding energy with respect to the Fermi level may be defined as:

$$E_b^k = E_{fin}^k(N-1) - E_{in}(N) \tag{1.75}$$

Koopmans assumed that the above binding energy difference can be calculated from Hartree–Fock wave functions for the initial as well as for the final state [52]. The binding energy is then given by the negative one–electron energy of the orbital from which the electron has been expelled by the photoemission process:

$$E_b^k = -\varepsilon_k \tag{1.76}$$

This approach assumes that the remaining orbitals are the same in the final state as they were in the initial state (*frozen–orbital approximation*) and leaves out the fact that after the ejection of an electron the orbitals will readjust to the new situation in order to minimize the total energy. This

is the intra–atomic relaxation. In fact the relaxation also has an extra-atomic part connected with the charge flow from the crystal to the ion where the hole was created. Therefore the binding energy is more accurately written as:

$$E_b^k = -\varepsilon_k - \delta\varepsilon_{relax} \tag{1.77}$$

where $\delta\varepsilon_{relax}$ is a positive relaxation correction. An even more rigorous analysis must take into account relativistic and correlation effects which are neglected in the Hartree–Fock scheme. Usually both increase the electron binding energy.

1.3.3 Photoelectron spectroscopy models

Three–step model

In frame of this model the complicated photoelectron processes broken up into three independent events [39]:

    (**I**) absorption of a photon and photo–excitation of an electron as described above;

    (**II**) transport of the electron to the surface;

Some of the photoelectrons reach the surface of the solid after suffering scattering processes, the dominant scattering mechanism being the electron–electron interaction. For low energies electron–phonon interaction dominates [53]. One of the most important parameter which describes these processes is the *inelastic mean free path* λ. It is defined as the mean distance between two successive inelastic impacts of the electron on its way through the crystal. Assuming that the mean free path λ is isotropic, several calculations were performed and an *universal dependence curve* of the mean free path was drawn [53–55]. More recent results based on Bethe's equation [56] came up with [57]:

$$\lambda(E) = \frac{E}{E_{plas}^2 \beta \ln(\gamma E)} \tag{1.78}$$

where λ will be deduced in (Å), E is the electron energy given in (eV), β and γ are parameters. E_{plas} is the plasmon energy of the free electron gas in (eV) and it can be calculated with $E_{plas}\, 28.8\sqrt{N_v\rho/M}$ where N_v is the number of valence electrons per molecule, ρ is the density and M is the molecular mass. An extended approach based on a modified Bethe equation delivers even better results [58–63]. For practical purposes the reduced

formula $\lambda \propto E^p$, where p ranges from 0.6 to 0.8, can be used since it delivers reasonable results of the mean free path for electron energies in 100–1000 eV range [64].

(III) escape of the electron into vacuum;

The escaping electrons are those for which the component of the kinetic energy normal to the surface is enough to overcome the surface potential barrier. The other electrons are totally reflected back.

One–step model

Apart from its didactic simplicity, the three–step model fails to offer a practical computational tool for the simulation of photoelectron lines. State of the art is the employing of one–step theoretical approaches in which the whole photoelectron process is regarded as a single one. The first of this kind was a compact and mathematically elegant solution to the previous three-step model [65] but was followed by fully dynamical [66] and relativistic one–step theories [48]. When specific crystal potentials are given as input data one–step models deliver theoretical simulations of the XPS spectra [67].

1.3.4 Spectral Characteristics

The first step which is taken generally in the sample characterization is the recording of a wide scan. This so called survey spectrum allows identifying the chemical components in the sample and to define acquisition windows. The lines which are of interest are recorded afterwards with a high resolution.

The XPS spectra can be divided into: *primary spectrum* which is given by the electrons which leave the solid without inelastic scattering processes, and *secondary spectrum* arising from photo-electrons which have already lost a percentage of their kinetic energy trough inelastic scattering processes on their way to the surface.

1.3.4.1 Core level lines

Photoemission produces a final state that is lacking one electron with respect to the initial state. Therefore PES (photoemission spectroscopy) always measures final-state energies which can be related to initial-state energies only after some theoretical considerations, as it was mentioned in the last paragraph. The XPS lines associated with the core levels may have variable intensities and widths, which, except for the s levels, are doublets. Photoelectrons, which originate from core-levels, give rise to the most intensive lines in the XPS spectra. The position of the core level lines is like a fingerprint for each element and thus the chemical identification

of the components in the investigated specimen can be easily performed. Generally two or more elements will be detected on the surface. The relative intensities of their lines are governed by: occupancy of the sub–shell, stoichiometry, and atomic cross-section σ. The values of σ can be derived from X-ray mass absorption coefficients or can be directly calculated [68, 69]. Since the occupancy of the atomic sub-shells is known, XPS can be used as a non-destructive chemical analysis tool.

Core-level lines shape and width

The width of the peak is defined as the full width at half maximum intensity (FWHM). This is a sum of three distinct contributions [70]: the natural inherent width of the core-level γ_n, the width of the photon source γ_p and the analyzer resolution γ_a. Thus the overall FWHM will be given by:

$$\gamma = \sqrt{\gamma_n^2 + \gamma_p^2 + \gamma_a^2}$$
(1.79)

The first contribution is dictated via the uncertainty principle $\Delta E \Delta t \geq \hbar$ by the core-hole life time τ.

$$\gamma_n = \frac{h}{\tau}$$
(1.80)

where h is the Plank constant. The lifetimes depend on the relaxation processes which follow the photoemission. The narrowest core-levels have lifetimes in the range $10^{-14} - 10^{-15}$ s whilst the broader have lifetimes close or slightly less than 10^{-15}s.

A range of physically possible line profiles in core-level XPS is possible, and simple Gaussian or Lorentzian functions are very rarely adequate. In the case of metal samples it has been shown that asymmetric profiles should be expected on theoretical grounds [71], however, recorded spectra exhibit deviations from idealized profiles due to a range of instrumental and physical effects:

• the response function of the electron analyzer;

• the profile of the X-ray line-shape;

• intrinsic life-time broadening of the core level hole state;

• photon broadening;

• differential surface charging of the sample.

In addition to the instrumental considerations the shape of a synthetic peak is also influenced by the choice of background algorithm used to remove the so-called extrinsic electrons from the

data. The intrinsic part of the XPS peak due to the core-level life time is described by a Lorentz function:

$$f_L(\varepsilon) = \left(1 + \frac{4\varepsilon^2}{\gamma_n^2}\right)^{-1}$$ (1.81)

where $\varepsilon = E - E_0$ is the difference relative to the maximum of the curve. The overall line shape of core lines are obtained by convoluting the above two functions in a resulting so-called Voigt profile:

$$f_L = f_L \otimes f_G = \int_{-\infty}^{+\infty} f_L(\varepsilon')f_G(\varepsilon - \varepsilon')d\varepsilon'$$ (1.82)

Doniach and Sunjic [71] have shown that in metals the core level lines have a characteristic asymmetrical shape:

$$f_{DS}(\varepsilon,\alpha) = \Gamma(1-\alpha)\frac{\cos\left[\pi\frac{\alpha}{2} + (1-\alpha)\arctan\left(\frac{2\varepsilon}{\gamma_n}\right)\right]}{\left[\varepsilon^2 + (\gamma_n/2)^2\right]^{\frac{1-\alpha}{2}}}$$ (1.83)

where Γ is the gamma function, $\Gamma(z) = \int_{-\infty}^{+\infty} t^{z-1}e^{-t}dt$, and α is an asymmetry parameter.

The values of α can range between 0.1 and about 0.25 [72]. For the case of non-conducting samples the asymmetry factor is equal to zero and $f_{DS}(\varepsilon,0) = f_L(\varepsilon)$. The asymmetry of the intrinsic XPS lines of conducting samples can be explained by taking into account the nonzero density of states at the Fermi level.

Spin-orbit coupling

In terms of a $j - j$ coupling scheme between angular and spin moments in an atom, for each orbital with nonzero angular quantum number l ($l > 0$), two energy levels are possible for electrons: the first with total quantum number $j = l + s$ and the second with $j = l - s$ (where s is the spin quantum number).

This spin–orbit splitting is present in XPS spectra; two peaks being observable, each for one j value. Taking into account that for a given j value there are ($2j + 1$) allowed states for electrons and that $s = 1/2$, the ratio of relative intensities can be easily calculated:

$$\frac{I_{j=l-s}}{I_{j=l+s}} = \frac{2\left(l-\frac{1}{2}\right)+1}{2\left(l+\frac{1}{2}\right)-1} = \frac{l}{l+1} \tag{1.84}$$

High–resolution core–level spectroscopy studies show small deviations from this branching–ratio due to different cross sections for the $j = l + s$ and $j = l - s$ lines and photo–diffraction effects.

Chemical shifts

In the investigation of the molecules and solids, one is not interested in the absolute binding energy of a particular core level, but in the change in binding energy between two different chemical forms of the same atom. This difference is the so-called chemical shift [45]. The chemical shift between a metal and its oxide can be used to monitor the surface cleanliness.

Multiplet splitting

In any atomic system with unpaired valence electrons, the exchange interaction affects spin-up and spin-down core electrons differently. Since exchange acts only between electrons with the same spin [73], core electrons with spins parallel to those of the unpaired valence electrons will experience a valence-electron exchange potential, whereas core electrons with spins antiparallel will not. Exchange interactions within or between closed shells balance exactly, as the numbers of electrons with same spin are equal. This interaction between core and unpaired valence electrons is responsible for core-polarization contributions to magnetic hyperfine structure [74]. The spectral splitting of the 3s core-level x-ray photoemission spectra (XPS) in transition metals and their compounds originates from the exchange coupling between the 3s hole and the 3d electrons and was experimentally observed about three decades ago [75, 76]. The magnitude of the 3s spectral splitting according to the van Vleck theorem [77] is determined by:

$$\Delta E_{ex} = \frac{2S+1}{2l+1} G^2(3s,3d) \tag{1.85}$$

where S is the total spin of the ground state of the 3d electrons, l is the orbital quantum number (l=2) and $G^2(3s,3d)$ is the Slater exchange integral. The intensity ratio for the two peaks is proportional in this model to the ratio of the angular momentum multiplicity:

$$\frac{I_{S+1/2}}{I_{S-1/2}} = \frac{2\left(S+\frac{1}{2}\right)+1}{2\left(S-\frac{1}{2}\right)+1} = \frac{S+1}{S} \tag{1.86}$$

The value of the multiplet splitting gives information about the total spin of 3d band [45]. The multiplet splitting of $2p_{3/2}$ line was observed in compounds with strong localized moments [78].

Satellites line

In the photoemission process the photon kicks out one electron so quickly that the remaining electrons do not have time to readjust. Thus the $(N - 1)$ electron system is left in a non–relaxed state Ψ_{fin}. This excited state has a certain overlap with the stationary states Ψ_n and according to the sudden approximation we obtain the probabilities $\left\langle \Psi_n \middle| \Psi_{fin} \right\rangle$ to end up in Ψ_n states [79]. This means that the XPS spectrum consists from the *main line* (corresponding to the lowest excited state) and a number of extra lines (so–called *satellites*) representing the higher excited states after photoemission.

In principle, there are two sources of satellites: an extrinsic part due to the *extra–atomic* events and an intrinsic part due to the *intra–atomic* relaxations.

The reorganization of electronic structure after the creation of a core hole could also lead to an excess of energy which is not available to the primarily excited photoelectron. Thus two–electron processes can occur in case of conducting samples. The corresponding structures in the spectra are denoted as *shake satellites*. The hole appears to increase the nuclear charge and this perturbation is the cause of valence electrons reorganization. It may involve the excitation of one of them to a higher energy level. If an electron is excited to a higher bounded state then the corresponding satellite is called *shake–up satellite*. If the excitation occurs into free continuum states, leaving a double ionized atom with holes both in the core level and valence shell, the effect is denoted as a *shake-off satellite* from [80]). Discrete shake-off satellites are rarely discerned in the solid [70].

1.3.4.2 Valence band

Whereas the core levels are usually reacted by well-resolved sharp XPS peaks, the valence band spectra are characterized by a band structure (many closely spaced levels) [70]. The valence electrons involved in the delocalized or bonding orbitals have low binding energies (< 20 eV). Because of the lower cross-sections of the valence photoelectrons as compared to the core photoelectrons, the valence band spectra intensity will appear much lower than for the core level spectra.

The valence band spectrum resembles the one–electron density of states curve, but due to certain facts they are not identical: the spectrum represents the DOS distribution in an excited state, several screenings of the created hole (many–body effects), emission of electrons with different quantum numbers (i.e. different sub-shell cross–sections) or from different atomic species (i.e. different atomic cross–sections) as well as the instrumental broadening being responsible for further modifications.

One way to interpret the XPS VB spectra is the comparison with theoretical calculations of the densities of states (DOS). The recorded spectra can be simulated when such calculations are available and thus the contribution of each sub–shell can be described. Another alternative is to employ different excitations energies. The relative intensities of the various valence electrons peaks can drastically change when varying the energy of the used radiation because the relative photo–ionization cross sections change versus the incident photon energy. For example, by comparing the UPS and XPS valence band spectra of a MxO oxide, one can get information about the partial contributions of the metal and oxygen states in the valence band. Another modern alternative is the interpretation of XPS VB in connection with other spectroscopic techniques like X–ray emission spectroscopy. In such joint VB studies certain features of the spectra can be directly assigned to the elemental components.

1.3.4.3 Secondary spectra (background)

During their transport to the surface, some photoelectrons lose part of their energy through inelastic scattering processes and end up at a lower energy in the spectrum, giving rise to a background. For quantitative analysis of the XPS spectra, the true peaks areas and their shapes need to be determined. Therefore, usually background corrections are applied. Shirley was the first to deal with this problem and he proposed a practical model [81]. However its results are in most of the cases unsatisfactory. In the Tougaard algorithms [82-85] the measured spectrum $j(E)$ is considered to consist of a primary photoelectron spectrum $F(E)$ and background, as given:

$$j(E) = F(E) + \lambda(E)\int_{E}^{\infty} K(E, E - E') j(E') dE' \qquad (1.87)$$

where $K(E, E - E')$ describes the probability that an electron with the energy E losses the energy $(E - E')$ during a mean free path travel. The second term in eq. (1.87) gives the

background correction. A universal loss function $\lambda(E)K(E,T)$ which should describe all pure materials was proposed:

$$\lambda(E)K(E,T) = \frac{B(T)}{\left[C + (T)^2\right]^2} \qquad (1.88)$$

where B and C are two constants. By comparison with experimental data, it was shown that the background correction for pure Ag, Au and Cu can be described using the following values: B = 2866 eV^2 and C = 1643 eV^2. In case of alloys this universal loss function delivers a general good fit with experiment. An accurate background can be obtained only from EELS (Electron Energy Loss Spectroscopy) experiments. In an EELS experiment electrons with kinetic energy E_0 are sent on the sample. A certain part of them will be reflected but the rest enter the surface and interact with the solid. Due to scattering processes the electrons lose energy E_L and leave the solid with the kinetic energy $E_S = E_0 - E_L$. The outgoing electrons are recorded energy resolved. In other words such an experiment simulates the kinetic energy loss of the XPS electrons [86].

1.3.4.4 Auger process

After photo–emission the core hole will be filled with an electron decaying from a higher occupied level. This recovery of the atom from a higher energy state may be accomplished by the photo–ejection of another electron. This two–electron process takes place on a 10^{-14} seconds time scale and is known as an Auger process. Fig. 1.12 presents a schematic energy level diagram of a solid, in which the energy is measured downwards from an assumed zero of energy at the Fermi level.
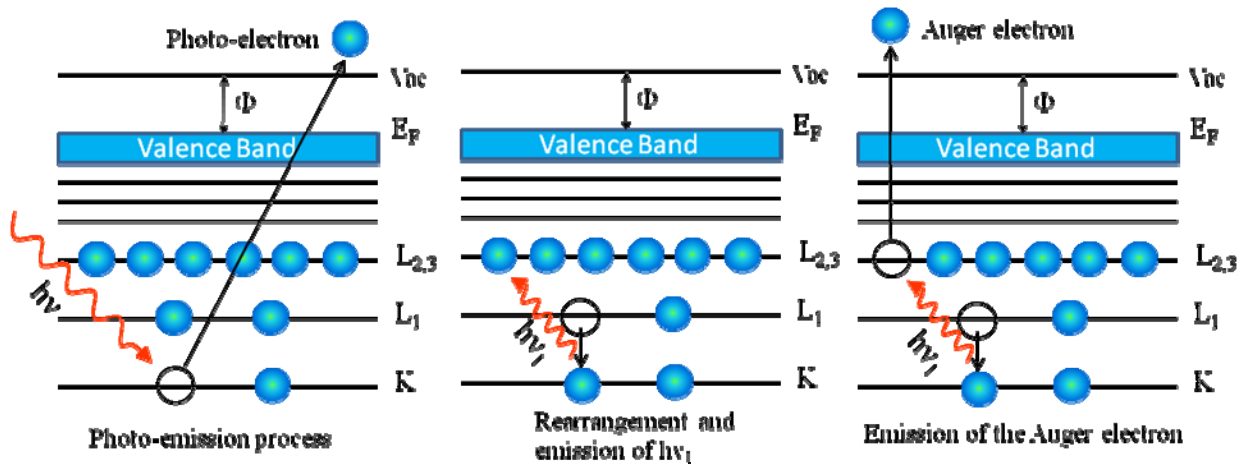
Fig. 1.12. Schematic diagram of the process of Auger emission in a solid (after [87])

In this example the K level is being ionized by an incident electron, whose energy E_p must be greater than the binding energy E_K of an electron in the K shell. Following creation of a hole in the level K, the atom relaxes by filling the hole via a transition from an outer level, in this example from the as L_1 level. As a result of that transition the energy difference $(E_K - E_{L_1})$ can be used by the atom in either of two ways. It can appear as a characteristic X-ray photon of that energy or it can be given to another electron either in the same level or in a more shallow level, whereupon the second electron is ejected. This first process is that of X-ray fluorescence, the second that of Auger emission. Both cannot take place from the same initial core hole, so that they complete. The Auger transition depicted in Fig.1.12, would be named in the conventionally used $j - j$ coupling $KL_1L_{2,3}$. The electrons taking part in the Auger process might also originate in the valence band of the solid, in which case the convention writes the transitions as, for example, $KL_{2,3}V$ if one electron comes from the valence band and, for example, KVV if both do. The energy of the ejected Auger electron is given by:

$$E_{KL_1L_{2,3}} = E_K - E_{L_1} - E^*_{L_{2,3}}$$

where E_i is the binding energies of the i-th atomic energy level. $E^*_{L_{2,3}}$ is starred because is the binding energy of the $L_{2,3}$ level in the presence of a hole in level L_1, and is therefore different from $E_{L_{2,3}}$.

Chapter 2

Preparation and Characterization techniques

2.1 Sample preparation

Polycrystalline samples were prepared by arc melting technique in a cold copper crucible under an argon atmosphere. High purity starting materials (>99.99%) were weighted in exact stoichiometric proportions and melted together. To ensure a good homogeneity of the samples, the compounds were melted several times in the same atmosphere. This preparation method preserves the phase from high temperatures. The weight loss of the final samples was found to be less than 1%. The homogeneity of the samples was checked by conventional X-ray diffraction technique. XRD measurements were performed on polished surfaces, due to the hardness of the samples. The quality of the samples, in terms of contamination, was also investigated by monitoring the oxygen and carbon 1s core levels by means of X-ray photoelectron spectroscopy.

2.2 Structure analysis

The crystallographic structure of all the samples was checked at room temperature using X-ray powder diffraction data. The interaction of X-rays with crystalline sample creates secondary diffracted beams of X-rays related to interplanar spacing in the crystalline powder according to the Bragg's Law:

$$n\lambda = 2d \sin \theta \qquad (2.1)$$

where n is an integer, λ is the wavelength of the incident X-ray beam, d is the interplanar spacing and θ is the diffraction angle. A typical powder diffraction pattern is collected in the form of scattered intensity as a numerical function of Bragg angle. The structure of every powder diffraction is determined by the unit cell dimensions and the atomic structure (unit cell content and special distribution of atoms in the unit cell) and can be thus be used to determine the crystalline structure of the samples. The individual Bragg peaks are located on the pattern and both their position and intensity are determined. The peak positions are used to establish the unit cell symmetry, parameters and content, while the peak intensities are used to determine space group symmetry and coordinates of atoms.

The structure investigation of the compounds was performed by conventional X-ray powder diffraction with Cu Kα radiation, using a Bruker AXS D8 Advance powder diffractometer. This instrument is based around a two circle goniometer, enclosed in a radiation

safety enclosure. The working principle of a Bragg-Brentano reflection goniometer is presented in Fig. 2.1.

The X-ray source is a 2.2 kW Cu anode situated in a long fine focus ceramic X-ray tube. The running conditions for the X-Ray tube are 40 kV and 40 mA. The sample stage is mounted on the goniometer for precision angle measurement. The two circle goniometer has independent stepper motors and optical encoders for the Theta and 2Theta circles with the following specifications: maximum measurement circle diameter of 250 mm, minimum measurement circle diameter of 100 mm, smallest angular step size of 0.0001^o, maximum rotational speed of 1500°/min, angular range (Theta) from -5° to 40°, angular range (2Theta) from -10° to 60°. The detector is a NaI dynamic scintillation detector with $2x10^6$ s^{-1} maximum count rate.
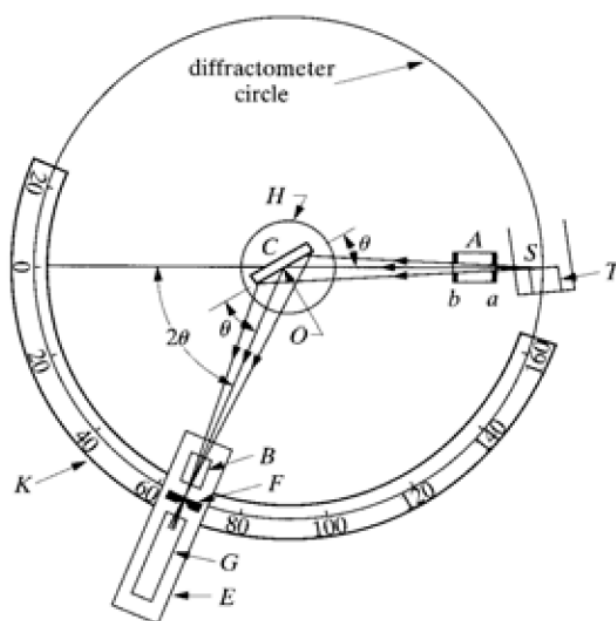
Fig. 2.1. Schematic diagram of a Bragg-Brentano Diffractometer

A computer controlled absorber is mounted directly in front of the detector and is used to attenuate the beam by about two orders of magnitude. To change the angular resolution several slits (0.05 to 2 mm) are available to be placed in front of the detector, as are a set of Soller slits to allow acquisition for small samples. Attenuators made of Cu and Ni are also available and can be manually placed in the beam, by inserting them into the slit holders in front of the detector. The detector electronics are capable of a $3x10^7$ s^{-1} count rate. In addition, the D8 Advance diffractometer can be equipped with a chamber for variable temperature or low pressure experiments. The software used enables the user to acquire and analyze data. For qualitative analysis the Rietveld method [88] was employed.

2.3 Magnetic measurements

The macroscopically magnetic properties (magnetic order, transition temperatures, magnetic moments, the contribution of each element to the total magnetization of the compound) were investigated by static and dynamic magnetic measurements in fields up to 10 T and temperature range of 4.2 – 1200K. A vibrating sample magnetometer (VSM) was used to measure the field and temperature dependence of the magnetization in order to determine the transition temperature and the value of the spontaneous magnetization at 0 K by extrapolation. A SQUID magnetometer was used to measure the magnetic susceptibility in field cooled (FC) and zero field cooled (ZFC). In the paramagnetic range (above the transition temperature) the variation of the magnetic susceptibility with the temperature was obtained using a Weiss balance and magnetic fields up to 1 T. The magnetic characterization of the investigated systems was realized by correlating the data from both ordered and paramagnetic states, which allowed the calculation of magnetic moments and the contribution of each element to the total magnetization of the compound.

2.3.1 Vibrating sample magnetometer

The Vibrating Sample Magnetometer (VSM) represents by far the most commonly used type of magnetometer. Since its invention some forty years ago, it has become the workhorse in both laboratory and production environments for measuring the basic magnetic properties of materials as a function of magnetic field and temperature.

The VSM, shown schematically in Fig. 2.2, employs an electromagnet which provides the magnetizing field, a vibrator mechanism to vibrate the sample in the magnetic field, and detection coils which generate the signal voltage due to the changing flux emanating from the vibrating sample. The output measurement displays the magnetic moment M as a function of the field H.

VSM operates by first placing the sample to be studied in a constant magnetic field, which will magnetize the sample. The stronger the constant field, the larger the magnetization will be. The sample is located at the end of a rigid holder attached to the vibration exciter and can oscillate in the vertical direction, perpendicular to the magnetic field. The sample rod can be rotated to achieve the desired orientation of the sample to the constant magnetic field. As the sample is moved up and down, it produces an alternating current in the detection coils at the same frequency as the vibration of the sample, according to Faraday's Law of Induction. The induction current which is proportional to the magnetization of the sample is then amplified by

an amplifier. Usually a lock-in amplifier is used to pick up only signals at the vibrating frequency, eliminating noise from the environment. The various components are hooked up to a computer interface. By varying the constant magnetic field over a given range, a plot of magnetization (M) versus magnetic field strength (H) is generated.
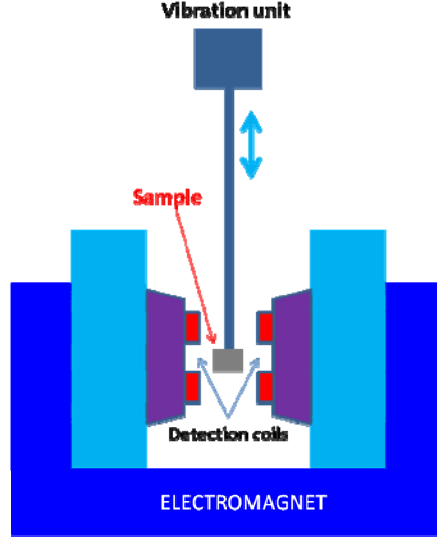
Fig. 2.2. Schematic diagram of the VSM

The spontaneous magnetization can be determined from magnetization isotherms, according to the approach to saturation law:

$$M = M_s\left(1 - \frac{\alpha}{H}\right) + \chi_0 H \qquad (2.2)$$

where χ_0 is a field independent susceptibility and α is the coefficient of magnetic hardness. Also the Curie temperature was determined from Arrott plot curves [89]. In the Arrott representation (M^2 versus H/M) the magnetic isotherms are parallel lines, with the critical isotherm passing through the origin. By using the experimental data for two temperatures close to the Curie temperature, $T_1 < T_C$ and $T_2 > T_C$, the Curie temperature is given by:

$$T_C = \frac{T_2\left(\frac{H}{M_C} - \frac{H}{M_1}\right) + T_1\left(\frac{H}{M_2} - \frac{H}{M_C}\right)}{\left(\frac{H}{M_2} - \frac{H}{M_1}\right)} \qquad (2.3)$$

All magnetization measurements were performed using a commercially built Oxford Instruments Vibrating Sample Magnetometer, located at the Laboratoire de Crystallographie CNRS, Grenoble. The VSM includes a cryostat for measurements between 4.2 K and 300 K. Measurements of magnetic moments as small as 5×10^{-6} emu are possible in magnetic fields from

zero to 8 T, reached using conventional laboratory electromagnets and superconducting solenoids. The vibration amplitude of the sample is 1.5 mm at a frequency of 55 Hz.

2.3.2 SQUID magnetometer

The superconducting quantum interference device (SQUID) consists of two superconductors separated by thin insulating layers to form two parallel Josephson junctions. The device may be configured as a magnetometer to detect incredibly small magnetic fields.

  ➢ Threshold for SQUID: 10^{-14} T
  ➢ Magnetic field of heart: 10^{-10} T
  ➢ Magnetic field of brain: 10-13 T

The great sensitivity of the SQUID devices is associated with measuring changes in magnetic field associated with one flux quantum. One of the discoveries associated with Josephson junctions was that the flux is quantized in units

$$\Phi_0 = \frac{2\pi\hbar}{2e} \cong 2.0678 \times 10^{-15}\, Tm^2$$

If a constant biasing current is maintained in the SQUID device, the measured voltage oscillates with the changes in phase at the two junctions, which depends upon the change in the magnetic flux. Counting the oscillations allows you to evaluate the flux change which has occurred.
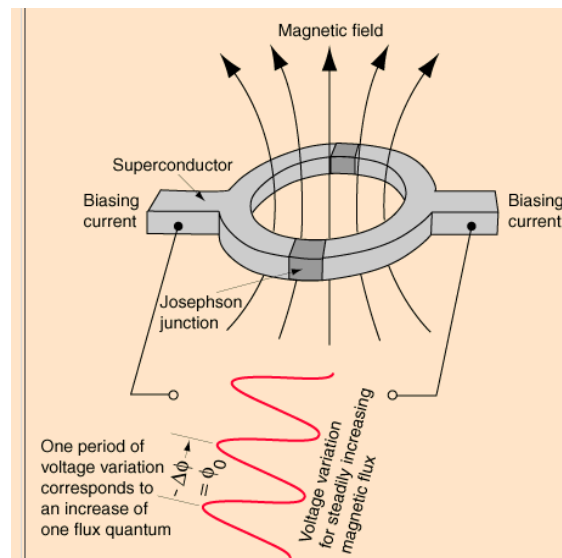
Fig. 2.3. Schematic representation of Josephson junction

The main components of a SQUID magnetometer are: (a) superconducting magnet (that must be acquired together its programmable bipolar power supply); (b) superconducting detection coil which is coupled inductively to the sample; (c) superconducting magnetic shield.
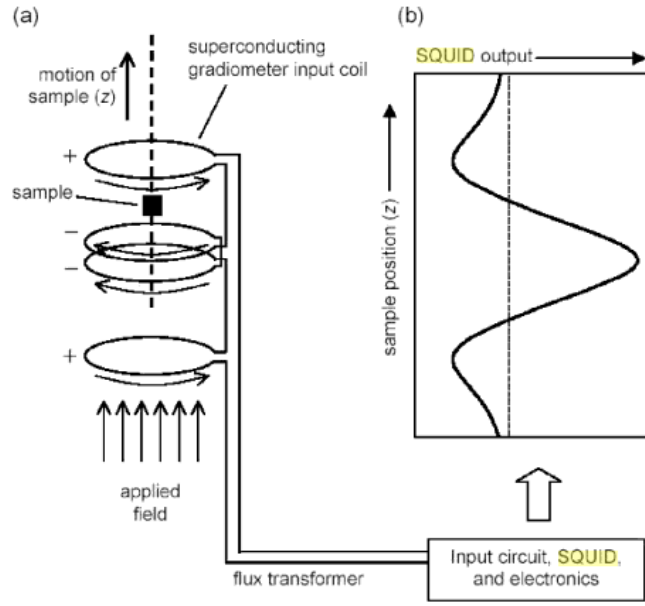
Fig. 2.4.a) Schematic of SQUID magnetometer; b) calibrated output from SQUID electronics

A superconducting magnet is a solenoid made of superconducting wire. This solenoid must be kept at liquid helium temperature. The uniform magnetic field is produced along the axial cylindrical bore of the coil. To operate a superconducting magnet requires an appropriate programmable bipolar power supply.

Superconducting detection coil is a single piece of superconducting wire configured as a second-order gradiometer. This pick-up coil system is placed in the uniform magnetic field region of the solenoid superconducting magnet.

Superconducting magnetic shield is used to shield the SQUID sensor from the fluctuations of the ambient magnetic field of the place where the magnetometer is located and from the large magnetic field produced by the superconducting magnet.

2.3.3 Weiss balance

The Weiss horizontal translation balance is a very sensitive instrument designed especially for investigating weak magnetic substances (diamagnets, antiferromagnets, spin-glasses) and for very small samples (about 10 mg), since it can measure magnetic susceptibilities as small as 10^{-7}. The detection of magnetic moments is done by measuring the force on a sample in an inhomogeneous magnetic field generated by an electromagnet. The inhomogeneity of the magnetic field between the poles of the electromagnet is determined by the shape of the caps. The force on a magnetic sample in the field gradient is given by:

$$F = \mu_0 m \chi H \frac{dH}{dx} \tag{2.4}$$
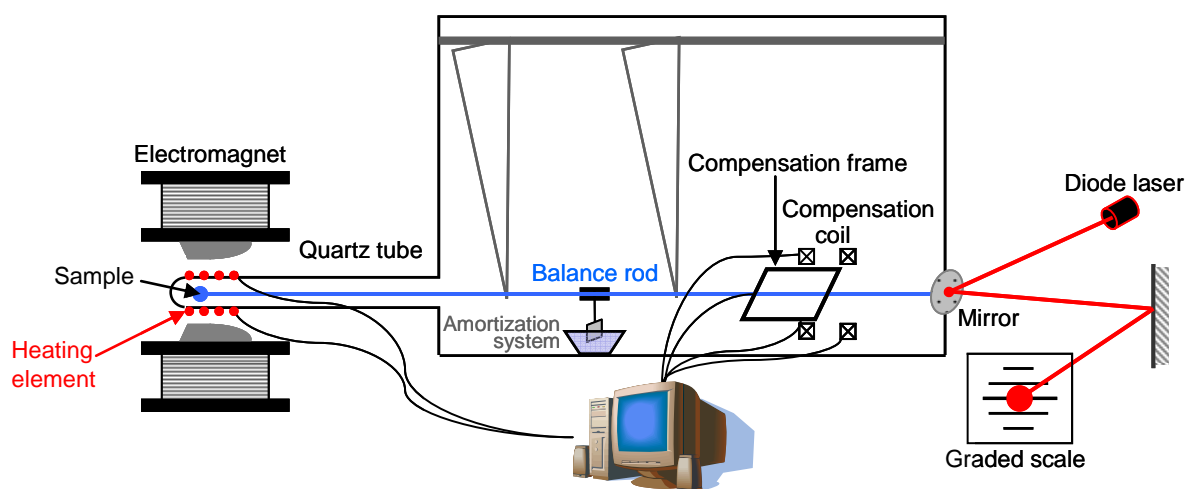
Fig. 2.5. Schematic diagram of a Weiss magnetic balance

As soon as the gradient *dH/dx* is known, it is easy to evaluate the magnetic susceptibility χ of a sample from the observed force.

The main components of the Weiss magnetic balance located in our laboratory are sketched in Fig. 2.5. The sample is housed in a quartz cup at the end of a horizontal quartz rod, connected to the balance beam, and is situated inside a quartz tube which is, between the pole caps, surrounded with a heating element in order to change the temperature. In order to guarantee proper force detection, the sample holder has to hang free from the walls of the surrounding tube. The balance rod is hanged in a horizontal position by two inextensible wires that allow free movement along the horizontal x-direction. The temperature is measured with thermocouples situated inside the quartz tube in the proximity of the sample. The current through the heating elements is controlled by a computer, allowing the programming of measurements at a user defined equidistant series of temperatures. The electromagnet used can generate magnetic fields up to 1.5 T. Our pole caps are cut so that on the symmetry axis of the magnet (x-direction) the product *HdH/dx* is constant over a considerable range in which the sample can move. The force generated by this gradient field will act along the x direction, producing a deviation of the laser beam spot on the graded scale in the optical system situated at the end of the balance rod. If the sample is at a position where the field gradient is known, the magnetic susceptibility can be evaluated from this deviation. A compensating coil system consisting of a rectangular frame fixed on the balance rod and two Helmholtz concentric coils is used to determine the force exerted on the sample. One side of the frame is situated outside the coils, while the opposite one is located in the centre of the Helmholtz coils perpendicular to the magnetic filed. An electrical current *I* applied through the frame will generate an axial compensatory force:

$$F_c = I_c l B \tag{2.5}$$

where B is the magnetic induction of the field generated by the Helmholtz coils and l is the length of the frame. This force is used to compensate the force given by Eq. (2.4).

$$I_c l B = \mu_0 m \chi H \frac{dH}{dx} \tag{2.6}$$

The zero deviation position is determined for zero magnetic fields ($H=0$, $B=0$) and no current through the frame ($I_c=0$). All these parameters are computer controlled. Considering that the magnetic induction B of is proportional to the current through the Helmholtz coils ($B=\alpha I H$):

$$I_c l \alpha I_H + (I_c l \alpha I_H)_{dia} = \mu_0 m \chi H \frac{dH}{dx} \tag{2.7}$$

where the second term is for the diamagnetic contribution of the balance rod. The measurement consists in compensating the effect of the applied magnetic field H on the sample by varying the compensatory currents in the Helmholtz coils and in the frame.

After performing a calibration by measuring the well known susceptibility of a small quantity of nickel of purity 99.999%, the magnetic susceptibility of an unknown sample is:

$$\chi = \chi_{Ni} \frac{m_{Ni}}{(I_c^{Ni} I_H^{Ni} + I_c^{dia} I_H^{dia})} \frac{(I_c I_H^i + I_c^{dia} I_H^{dia})}{m} = k \frac{(I_c I_H^i + I_c^{dia} I_H^{dia})}{m} \tag{2.8}$$

The effective magnetic moments for ferromagnetic and antiferromagnetic materials can be determined from the temperature dependence of the reciprocal susceptibility above the transition temperature, where the magnetic susceptibility obeys the Curie-Weiss law. This assumption is valid also for ferrimagnetic materials, for which the high temperature asymptote to the Néel hyperbolic law has a Curie-Weiss behavior. The molar Curie constant C is obtained from the slope of the temperature dependence of the reciprocal susceptibility at high temperatures, by linear fitting, and the magnetic moment is calculated as:

$$\mu_{eff} \cong 2.84\sqrt{C} \tag{2.9}$$

If more than one type of atoms contributes to the magnetic susceptibility of the material, the molar Curie constant is given by:

$$C = \sum_i C_i \tag{2.10}$$

2.4 X- ray photoelectron spectroscopy

The electronic structure of the materials was investigated by means of X-ray photoelectron spectroscopy, which was presented in the previous chapter. The XPS experiments

were performed using a commercially available spectrometer PHI Model 5600 Multi-Technique System produced by the Perkin Elmer Corporation, located at the Osnabrück University. The PHI spectrometer is built up from: a control computer, electronic control units, a "quick-entry" system and a main and preparation chamber. The bulk samples were crushed in situ in the preparation chamber in high–vacuum conditions (usually around $7x10^{-8}$ torr), in order to prevent surface contamination, and then transferred to the main chamber where the measurements were performed. A quick–entry system is also available allowing a rapid, convenient, and direct introduction of samples into the main chamber.

The main components of the spectrometer, which is situated in the main chamber, are sketched in Fig. 2.6.
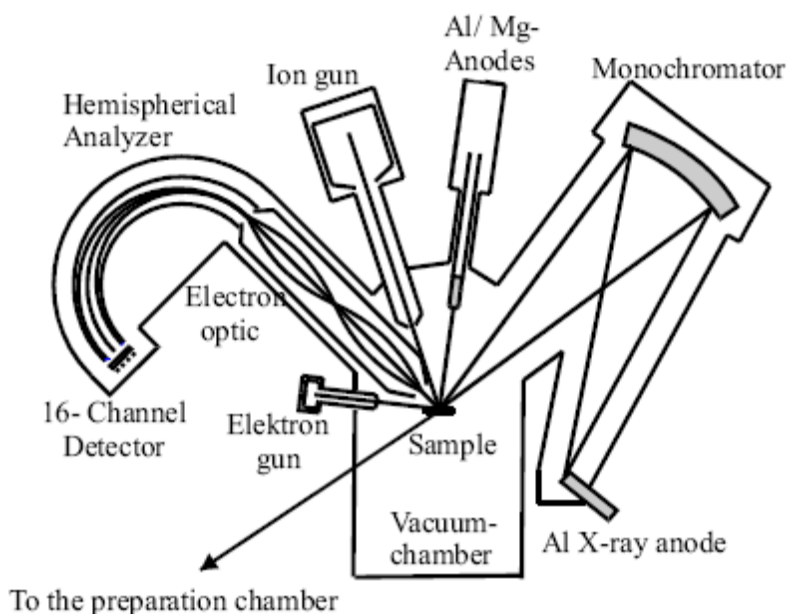
Fig. 2.6. Schematic diagram of the PHI 5600 spectrometer

The spectrometer is equipped with Al anode for measurements with monochromatic radiation and a dual Al/Mg anode positioned in an angle of 54.7^o to the analyzer. The characteristic energy and half–widths for the unmonochromatized radiations are: 1486.6 eV and 0.85 eV for Al Kα radiation and 1253.6 eV and 0.7 eV for Mg Kα radiation. The Al Kα characteristic radiation is filtered through a monochromator consisting of an accurate quartz crystal. The Al anode-crystal-sample angle is 23°, as resulted from the Bragg relation for the first order diffraction of Al Kα radiation ($\lambda = 8.34°A$) and $d = 4.255°A$ spacing of the (100) planes. The crystal–sample–analyzer angle is fixed to 90°. The monochromator focuses the radiation to a spot of 0.9 mm on the sample due to its toroidal shape, reduces the half-width to about 0.3 eV, eliminates the

satellites of characteristic Al Kα radiations and improves the signal to background ratio. All the XPS spectra were measured using monochromatic radiation from an Al anode with 12 kV accelerating potential and powered with 250 W. The energy of the photoemitted electrons is filtered using an 11 inches hemispherical condenser. The photoelectrons are focused with an electronic lens system and then enter the analyzer through an entrance slit which can be set to 4, 2, 0.5 or 0.15 mm. During all XPS measurements the "constant analyzer transmission" (CAT) mode was used, so that only the electrons with the energy $E_p \pm \Delta E$ (where E_p is the "pass-energy" and ΔE is the absolute energy resolution) passed through the analyzer. The relative resolution of the analyzer is given approximately by [90]:

$$\frac{\Delta E}{E_0} \approx 0.63 \frac{w}{R_0} \qquad (2.11)$$

where E_0 is the kinetic energy of the entering electrons and R_0 is the median radius of the hemispherical analyzer. For a $R_0 = 11$ inches analyzer and a $w = 2$ mm entrance slit, the absolute resolution of the analyzer is about 0.45% of the pass energy, considering that in the CAT mode E_0 corresponds to the pass–energy. For the detection of the electrons a multi channel detector with 16 channel plates is employed. The system also contains an ion gun with argon which can be used to perform sputter-etching of the samples. The ions can be accelerated to 4.5 kV maximal potential with a 3 μA available ion–current over a 10mm × 10mm scannable surface and a 100 μm focus. However, the ion gun was not used for the present work, due to the fact that even low accelerating potentials may induce drastic changes in surface geometry and/or stoichiometry [87]. For insulating samples a low-energy electron gun can be used to compensate the superficial local charges accumulated on the surface. The accelerating potential can be chosen between 0 and 10 V at a maximal current of 25 μA. All components of the main chamber ware kept under UHV during the experiments. There are two important reasons why ultra–high vacuum (UHV) conditions are requested when performing XPS measurements. In order for the photoelectrons to reach the analyzer without being scattered by gas molecules a basic vacuum in the 10^{-5} torr range is required. However under such a pressure the surface of the sample is quickly contaminated. In order to avoid surface contamination during the measurements, which can take up to several hours, a base pressure of about 10^{-10} torr must be ensured. UHV conditions are reached by employing a combination of appropriate turbo molecular, sputter and sublimation vacuum pumps. During the recording of the XPS spectra presented in this work the base pressure in the main chamber was maintained below 1×10^{-9} torr.

2.5 Electronic structure calculations

Theoretical investigations of the electronic and magnetic properties of selected alloys and compounds have been performed using the Munich SPR-KKR package version 3.6 [91]. The electronic structure of the alloys and compounds in the ferromagnetic state were calculated self-consistently by means of the spin polarized relativistic Korringa–Kohn–Rostocker (KKR) method in the atomic sphere approximation (ASA) mode [92-94]. Several different properties can be investigated by means of the SPRKKR package on the basis of the fully relativistic electronic structure calculation, especially response functions and spectroscopic properties.

The calculation method is based on the KKR-Green's function formalism that makes use of multiple scattering theory. This implies that the information on the electronic structure of a system is not expressed in terms of Bloch wave functions and eigenvalues but the corresponding Green's function. The method is based on the following Dirac-Hamiltonian for a spin-polarized system:

$$\left[\frac{\hbar}{i} c\vec{\alpha} \cdot \vec{\nabla} + \beta mc^2 + V_{eff}(\vec{r}) + \beta\vec{\sigma} \cdot \vec{B}_{eff}(\vec{r}) \right] \Psi_i(\vec{r}) = \varepsilon_i \Psi_i(\vec{r}) \tag{2.12}$$

where $\Psi_i(\vec{r})$ are four-component wave functions with corresponding single particle energies ε_i, α and β are the standard 4x4 Dirac matrices, and the effective potential V_{eff} contains the external contributions. The effective magnetic field is given by:

$$\vec{B}_{eff}(\vec{r}) = \vec{B}_{ext}(\vec{r}) + \frac{\partial E_{xc}[n,\vec{m}]}{\partial\vec{m}(\vec{r})} \tag{2.13}$$

where E_{xc} is the exchange and correlation energy which depends on the particle density n and spin magnetization density m. Within the multiple-scattering formalism the electronic Green's function for an ordered system with many atom sites per unit cell is given by:

$$G(\vec{r},\vec{r}',E) = \sum_{\Lambda,\Lambda'} Z_\Lambda^q(\vec{r},E)\tau_{\Lambda\Lambda'}^{nqn'q'}(E)Z_{\Lambda'}^{q'\times}(\vec{r}',E) - $$
$$- \sum_\Lambda \left[Z_\Lambda^q(\vec{r},E)J_\Lambda^{q\times}(\vec{r}',E)\Theta(r'-r) + J_\Lambda^q(\vec{r},E)Z_\Lambda^{q\times}(\vec{r}',E)\Theta(r'-r) \right]\delta_{nn'}\delta_{qq'} \tag{2.14}$$

where $\vec{r}(\vec{r}')$ is assumed to be within the unit cell $n(n')$ and atomic site $q(q')$ and $\tau_{\Lambda\Lambda'}^{nqn'q'}(E)$ is the scattering path operator with the combined index $\Lambda=(\kappa,\mu)$ standing for the spin-orbit and magnetic quantum numbers κ and μ, respectively. The four-component wave functions Z_Λ^q and J_Λ^q are the properly normalized regular and irregular solutions to the single-site Dirac equation for the atomic site q. The scattering path operator [95] transfers a wave with spin angular

character Λ' coming in at site q' into a wave outgoing from site q with character Λ taking into account in a consistent way all possible multiple scattering events in a many-atom system. In the case of ordered infinite systems, $\tau_{\Lambda\Lambda'}^{qq'}(E)$ for one atom per unit cell is obtained from the Brillouin-zone integral:

$$\tau_{\Lambda\Lambda'}^{qq'}(E) = \frac{1}{\Omega_{BZ}} \int_{\Omega_{BZ}} d^3k \left[t^{-1}(E) - \underline{G}(\vec{k},E) \right]_{\Lambda\Lambda'}^{-1} \exp\left[i\vec{k}\left(\vec{R}_q - \vec{R}_{q'} \right) \right] \tag{2.15}$$

where the single site t-matrix is fixed by the solutions to the single-site Dirac equation for site q, $\vec{R}_{q(q')}$ denotes the lattice vector for site $q(q')$ and $\underline{G}(\vec{k},E)$ is the relativistic k dependent structure constant matrix.

The charge density and spin magnetization are obtained by:

$$n(\vec{r}) = -\frac{1}{\pi} \Im Trace \int^{E_F} dE G(\vec{r},\vec{r}',E)$$

$$m(\vec{r}) = -\frac{1}{\pi} \Im Trace \int^{E_F} dE \beta \sigma_z G(\vec{r},\vec{r}',E) \tag{2.16}$$

By using an appropriate algorithm the potential functions V and B are recalculated until self-consistency is achieved. Most electronic properties, such as the spin and orbital magnetic moments, can be obtained from the Green's function:

$$\mu_{spin}(\vec{r}) = -\frac{\mu_B}{\pi} \Im Trace \int^{E_F} dE \int_V d^3r \beta \sigma_z G(\vec{r},\vec{r}',E)$$

$$\mu_{orb}(\vec{r}) = -\frac{\mu_B}{\pi} \Im Trace \int^{E_F} dE \int_V d^3r \beta l_z G(\vec{r},\vec{r}',E) \tag{2.17}$$

One of the greatest advantages of the SPRKKR package is the calculation of component-resolved results, which were found to be in very satisfying agreement with the experimental results [96].

Also spectroscopic properties, such as valence-band x-ray photoemission spectra, can be calculated by the SPRKKR programs, from the site-diagonal energy dependent scattering path operator $\tau_{\Lambda\Lambda'}^{qq'}(E)$. The correlation of computed and measured XPS valence band spectra provides further insight on the electronic structure of the investigated systems.

Chapter 3

Electronic structure and magnetic properties
of Mn$_{1-x}$Al$_x$Ni$_3$ alloys [97-99]

This chapter presents the effects of substitution of Al for Mn in MnNi$_3$, investigated by X-ray diffraction, magnetic measurements, X-ray photoelectron spectroscopy (XPS), and band structure calculations. Aluminum brings three electrons per atom in the conduction band, so it is expected to observe changes in the electronic and magnetic structures.

The compounds MnNi$_3$ and AlNi$_3$ are isostructural and crystallize in the AuCu$_3$ structure type. They form solid solutions in the whole range of concentrations. The ternary phase diagram of Ni-Mn-Al alloys, at T=1273K is shown in Fig. 3.1. The back areas denote the range of solid solubility.
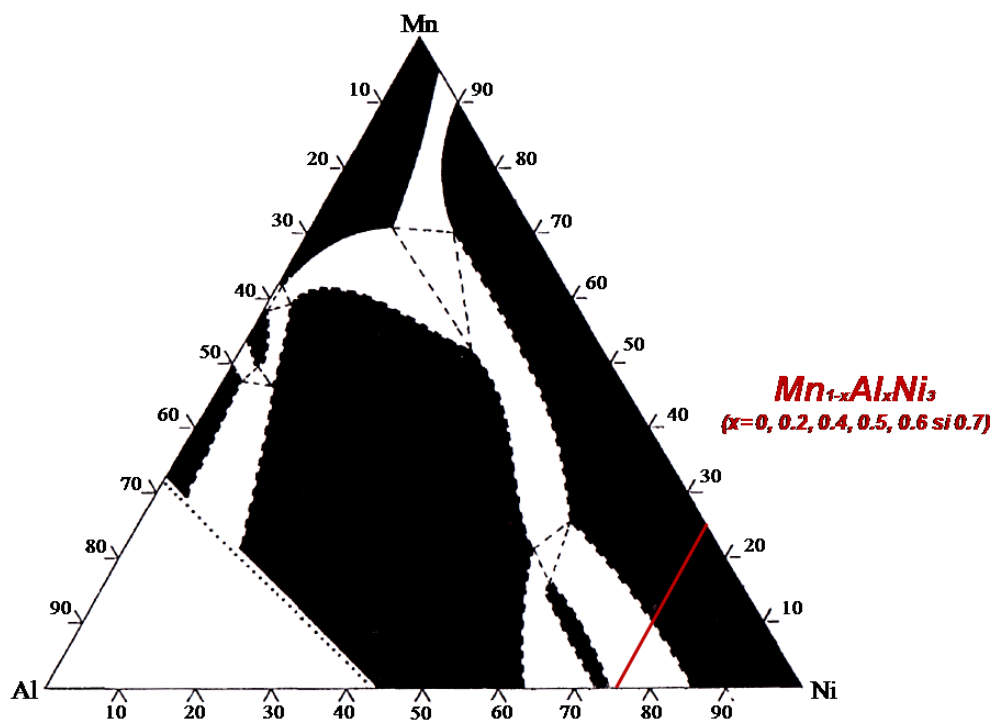
Fig. 3.1. Ternary phase diagram of Ni-Mn-Al alloys at T=1273K

Earlier studies have shown that the crystallographic disorder degree of MnNi$_3$, defined as the ratio between the Ni sites occupied by the Mn atoms and total number of Mn atoms in the lattice, depends on the preparation method and thermal treatment [100]. The magnetic properties of MnNi$_3$ are strongly influenced by the disorder degree, e.g., the Curie temperatures of ordered and disordered MnNi$_3$ have the values: 770 K and 132 K, respectively [101, 102] and the values of

the magnetizations are quite different. In the disordered $MnNi_3$ compound, since the near-neighbour Mn-Mn interactions are antiferromagnetic, a number of Mn magnetic moments do not contribute to the magnetization. As the compound becomes ordered, the ferromagnetic Mn-Ni interactions are dominant and an increase in the magnetization is observed. A fully ordered $MnNi_3$ compound was obtained only after a thermal treatment of 32 days in the 673 K – 828 K temperature range [103]. The magnetic properties of $AlNi_3$ have been of considerable interest since the compound was reported as a Stoner-Wohlfarth weak-itinerant ferromagnet, with T_C = 41.5K [104]. The magnetic properties of $Mn_{1-x}Al_xNi_3$ alloys have been studied only for a limited range of Al concentration, namely for $x \geq 0.7$ [105, 106]. The investigated samples were crystallographically ordered after a thermal treatment at 1323 K for 2 days [106] and at 1123 K for 24 h [105], respectively. It was shown that Al replaces Mn in the crystallographically ordered $Mn_{1-x}Al_xNi_3$ alloys. There is no systematic investigation concerning the magnetic behaviour of the $MnNi_3$ - $AlNi_3$ solid solution system in correlation with XPS measurements.

3.1 Structural characterization

Six samples from the $Mn_{1-x}Al_xNi_3$ system (x=0.0, 0.2, 0.4, 0.5, 0.6, 0.7) were prepared. In order to study the influence of Al on the crystallographic order, no thermal treatment was made after the cooling of the samples. The XRD measurements were performed on polished surfaces, due to the hardness of the samples. The XRD patterns are shown in Fig. 3.2 together with the theoretical spectra of $MnNi_3$ and $AlNi_3$ generated using PowderCell program.
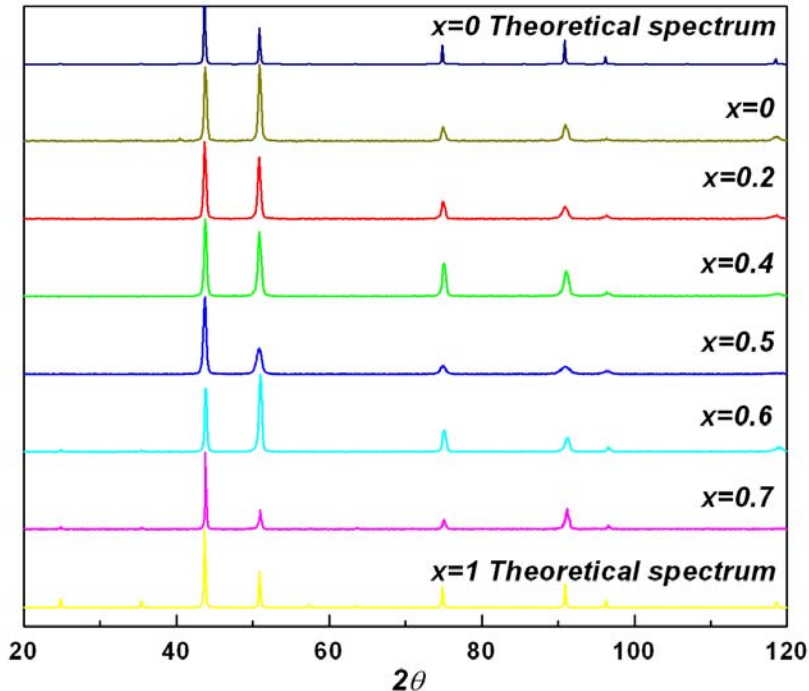
Fig. 3.2. X-ray diffraction pattern of $Mn_{1-x}Al_xNi_3$ alloys and the theoretical spectra of $MnNi_3$ and $AlNi_3$

All the investigated alloys are single phases with the same crystallographic structure type as the parent compound $MnNi_3$ (Fig. 3.3a).

The lattice parameters, estimated using the PowderCell program, decreases monotonically with Al concentration from a = 3.5854 Å for $MnNi_3$ to a = 3.5770 Å for $Mn_{0.3}Al_{0.7}Ni_3$ (Fig. 3.3b). The lattice parameter of $MnNi_3$ is very close to that reported in literature [107].
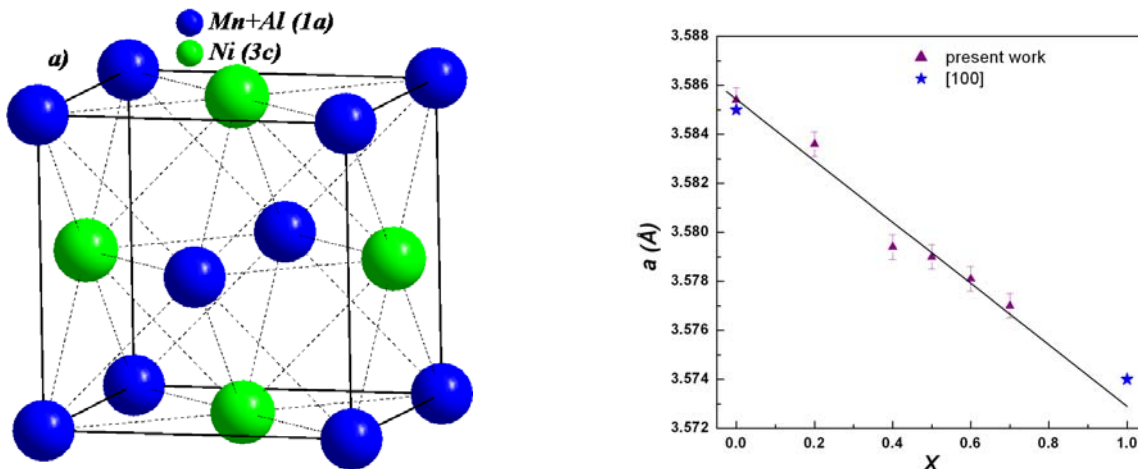
Fig.3.3. (a) Elementary cell of $Mn_{1-x}Al_xNi_3$ crystallographic ordered alloys and

(b) the variation of the lattice parameter with Al content

3.2 XPS Spectra

To illustrate the quality of the samples, in Fig. 3.4 is shown the survey spectrum of $Mn_{0.5}Al_{0.5}Ni_3$ alloy with the identification of core levels and Auger lines. Contamination is almost absent.
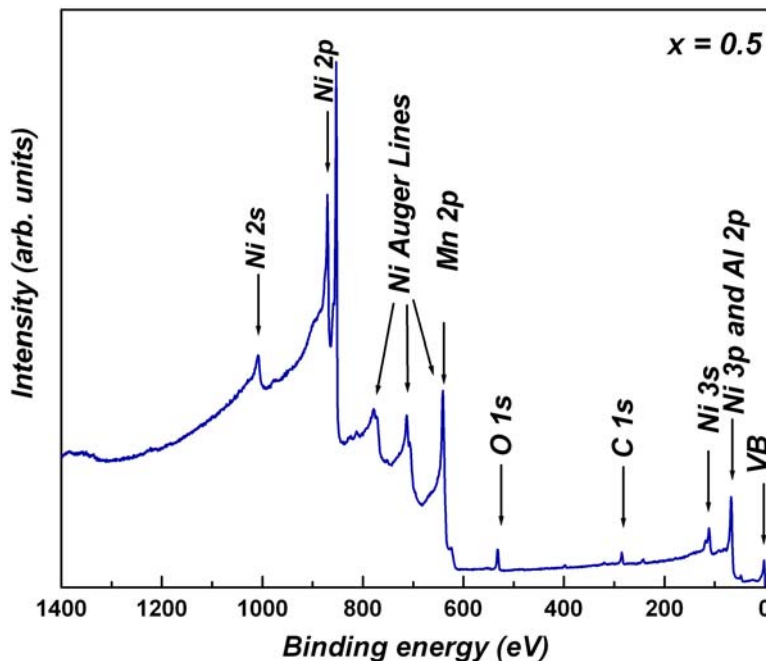
*Fig. 3.4. **S**urvey spectra of $Mn_{0.5}Al_{0.5}Ni_3$*

54

XPS valence band spectra of the $Mn_{1-x}Al_xNi_3$ alloys and pure Ni are shown in Fig. 3.5. For Al K_α radiation, the Ni 3d cross section is about four times larger than the Mn 3d cross section [108]. Taking also into account the ratio between the contents of Ni and Mn in the alloys, one can say that the valence-bands of $Mn_{1-x}Al_xNi_3$ alloys are dominated by the Ni 3d states, which are preponderant at the Fermi level as in metallic Ni. The Mn 3d states are concentrated at the bottom of the valence band in the region around 3 eV binding energy, as was found experimentally and proved by band structure calculations in many alloys and intermetallic compounds based on Mn [109-111]. The XPS valance band spectra of investigated samples present satellite structures at about 6.5 eV, which decreases in intensity with the increase of Al content. The valence band centroids are shifted towards higher binding energies and the density of states (DOS) at Fermi level decreases as the Al concentration increases, suggesting a partial filling of the Ni 3d band due to hybridization of the Al 3sp and Ni 3d states. In d-band metals and alloys the 3d states are shifted gradually to higher binding energy with the increase in the d-state occupancy and consequently a decrease in the density of states at the Fermi level occurs.
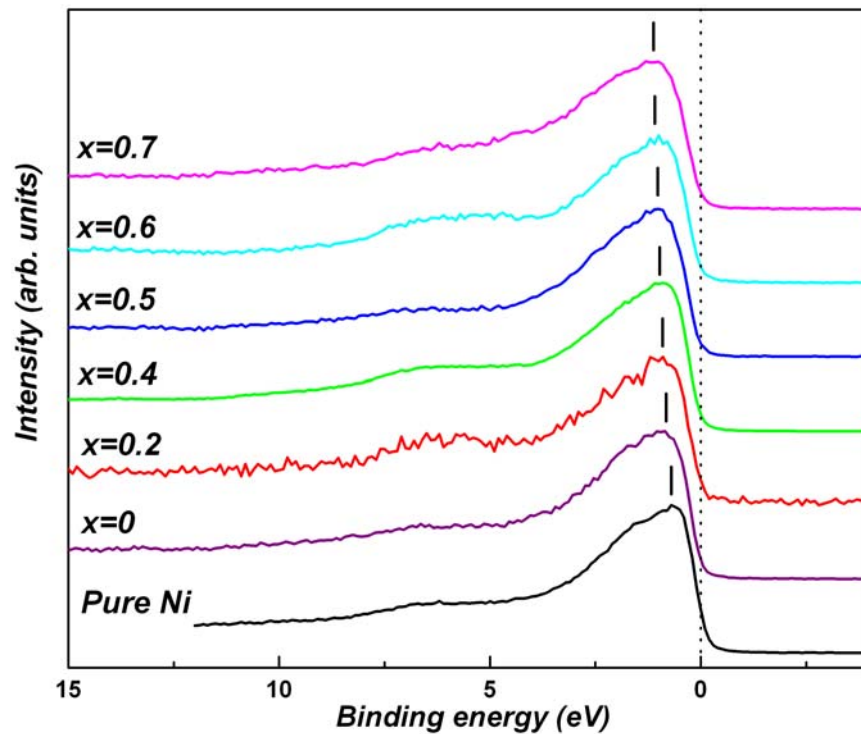
Fig. 3.5. XPS valence band spectra of pure metallic Ni and $Mn_{1-x}Al_xNi_3$ alloys. The dotted line and the bars indicate the Fermi level and the position of the valence band centroids

The Ni 2p XPS spectra of pure metallic Ni and investigated alloys are shown in Fig. 3.6. Like in the case of pure metallic Ni, the Ni $2p_{3/2}$ core level spectra of $Mn_{1-x}Al_xNi_3$ alloys exhibit satellite structures at about 6.5 eV higher binding energy than the main line.
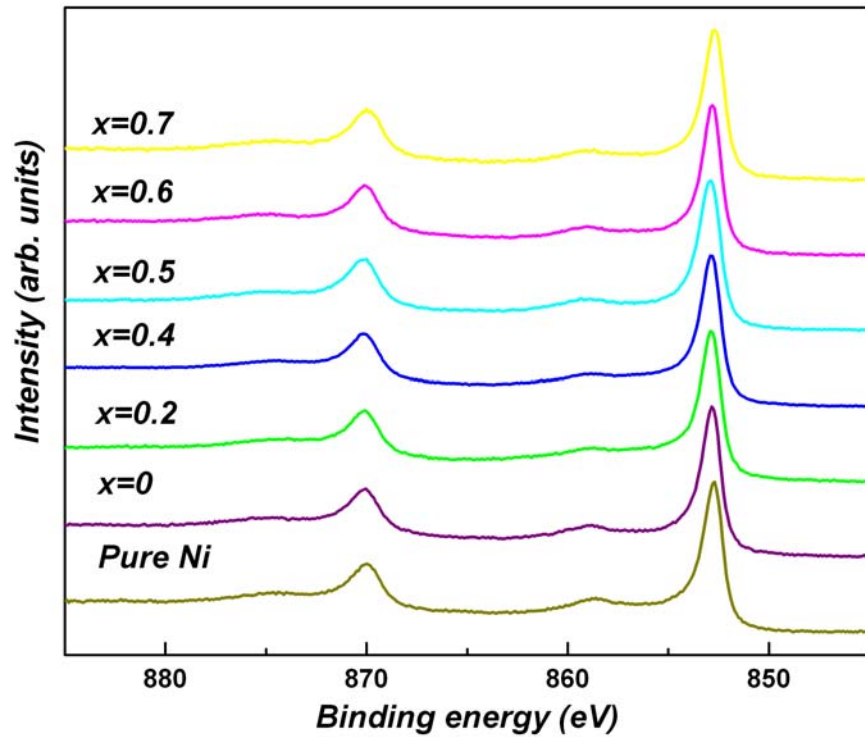
Fig .3.6. Ni 2p XPS spectra of $Mn_{1-x}Al_xNi_3$ alloys and pure metallic Ni

The observation of satellites proves that the Ni 3d band is not completely filled. The relative intensity of the satellite structure is proportional to the unoccupied Ni 3d states. In order to see the influence of the Al concentration on the unoccupied Ni 3d states the Ni 2p spectra of $Mn_{1-x}Al_xNi_3$ alloys were fitted with four components corresponding to Ni $2p_{3/2}$, Ni $2p_{1/2}$ and two satellite lines (Fig. 3.7).
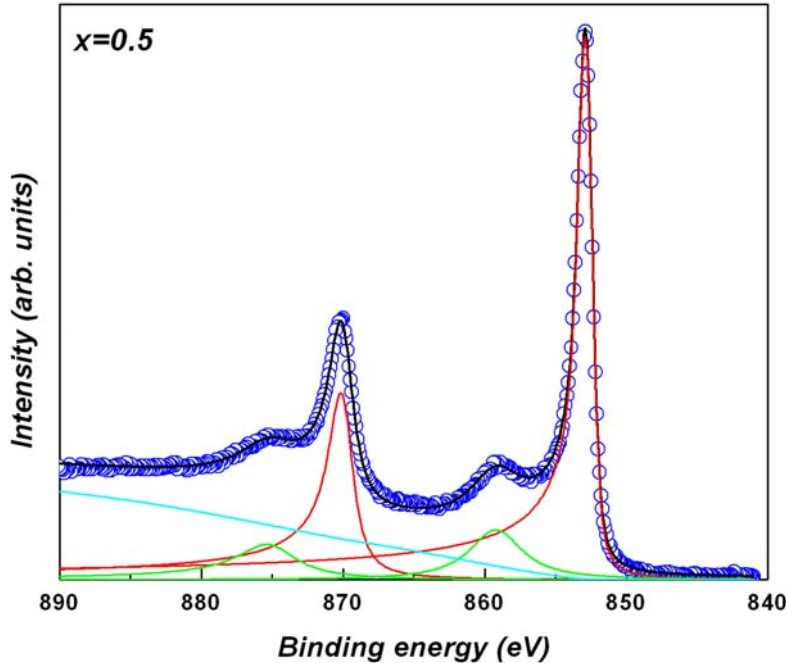
Fig .3.7. Ni 2p curve fitting results of $Mn_{0.5}Al_{0.5}Ni_3$ alloy

The satellite intensity decreases with the Al concentration. This confirms the partial filling of the Ni 3d band due to the hybridization with the Al 3sp states.

There is an overlapping between Mn2p XPS line and Ni $L_2M_{23}M_{45}$ Auger line (Fig. 3.8). The subtraction of the Ni Auger line was made in two steps. First the survey spectrum of pure Ni metal was normalized to 1 in order to see the relative intensity of the Ni Auger line and Ni 2p line. Using this ratio, in the normalized survey spectrum of the investigated alloys (again the most intense line is Ni 2p), the relative intensity of the Ni Auger line and the total measured line (Mn 2p+Ni Auger) line was estimated. Then the high resolution lines of Ni Auger from Ni metal and measured spectrum (Ni Auger+Mn2p) were normalized to this relative intensity. In the second step a superposition of the Ni Auger line and measured spectrum, in the 637-634 eV region was considered; in this region the only contribution to the measured spectrum comes from Ni Auger line (see Fig. 3.8).

Fig .3.8 Mn 2p XPS spectra of $Mn_{1-x}Al_xNi_3$ alloys before the subtraction of the Ni Auger Line

After the Ni Auger line subtraction and background removal, using a Shirley-type background shape, we have also fitted the Mn $2p_{3/2}$ core-level spectra for some of the investigated alloys with four components and a satellite line situated at binding energy around 644.5 eV. The curve fitting results for $Mn_{0.3}Al_{0.7}Ni_3$ is given in Fig. 3.9, with the mean energy separation $\Delta_{ex}\approx1.1$ eV. This is a clear evidence of the existence of local moments confined on Mn sites.
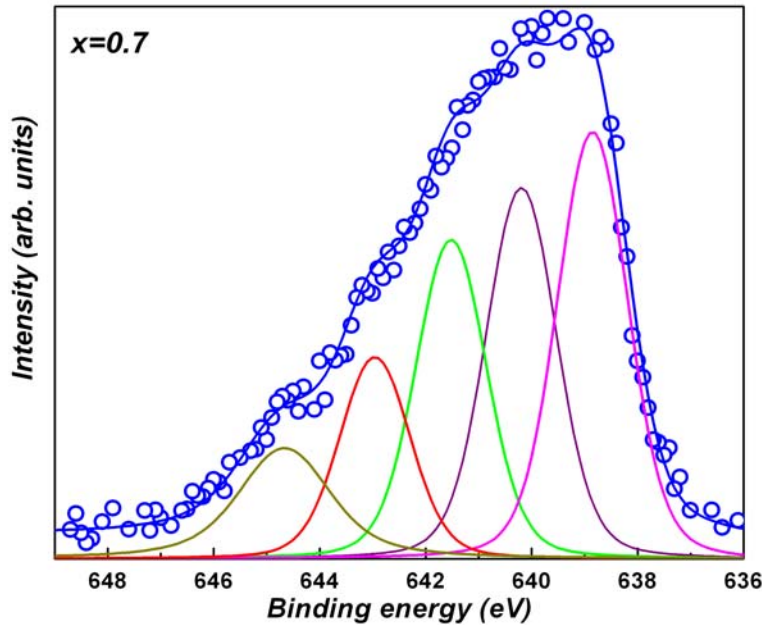
Fig .3.9. Mn 2p$_{3/2}$ curve fitting results of Mn$_{0.3}$Al$_{0.7}$Ni$_3$ alloy

3.3 Magnetic measurements

The values of the spontaneous magnetization, for each temperature, were determined from M(H) curves by extrapolation the linear dependence at H→0. The temperature dependence of the spontaneous magnetization of Mn$_{1-x}$Al$_x$Ni$_3$ alloys is shown in Fig. 3.10.
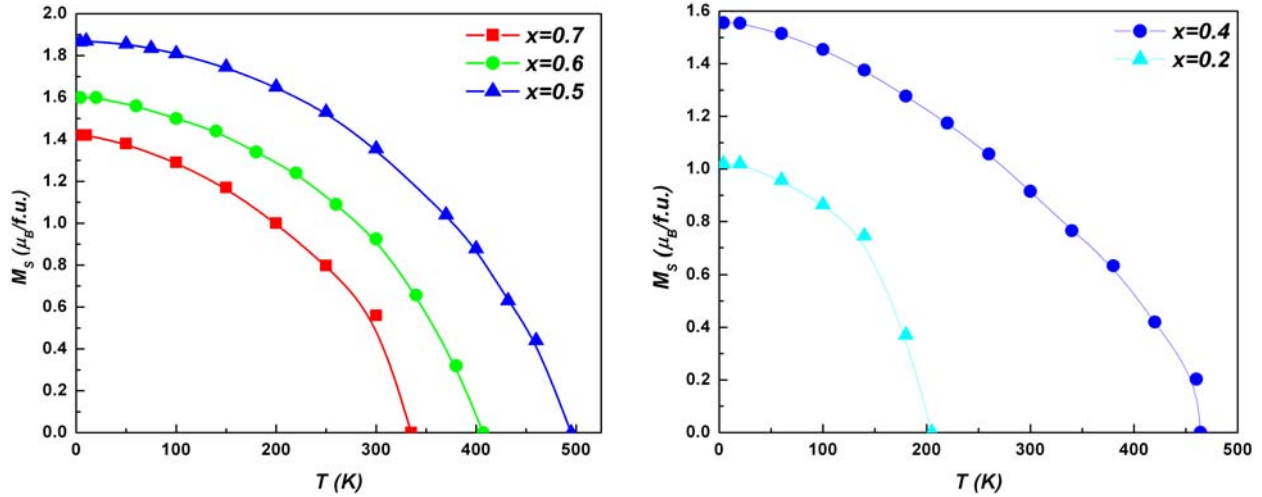
Fig. 3.10. Temperature dependence of spontaneous magnetization of Mn$_{1-x}$Al$_x$Ni$_3$ alloys

The variations of magnetization with magnetic field (Fig. 3.11) and temperature suggest that the investigated alloys have a ferromagnetic behaviour, below the corresponding Curie temperatures. Nevertheless, the values of the spontaneous magnetizations show that for high Mn concentrations appear Mn-Mn antiferromagnetic pairs which leads to smaller values of the spontaneous magnetization per unit formula.
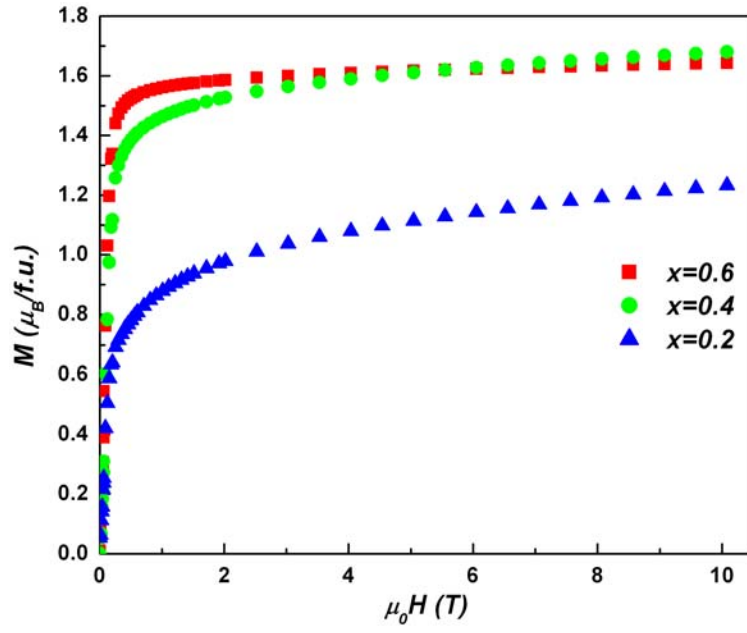
Fig. 3.11. Magnetic field dependence of magnetization at T=4K of Mn$_{0.4}$Al$_{0.6}$Ni$_3$, Mn$_{0.6}$Al$_{0.4}$Ni$_3$ and Mn$_{0.8}$Al$_{0.2}$Ni$_3$ alloys.

The Curie temperatures were determined from the Arrot plots (Fig.3.12) using the relation:

$$T_C = \frac{T_2\left(\dfrac{H}{M_C} - \dfrac{H}{M_1}\right) + T_1\left(\dfrac{H}{M_2} - \dfrac{H}{M_C}\right)}{\dfrac{H}{M_2} - \dfrac{H}{M_1}}$$
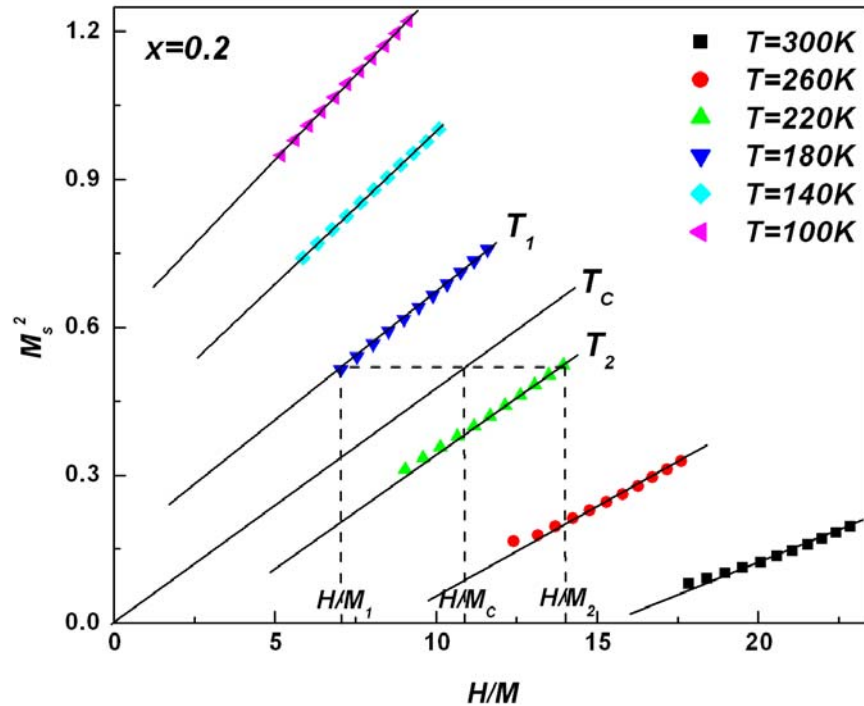
Fig. 3.12. The Arrot plots representation of Mn$_{0.8}$Al$_{0.2}$Ni$_3$ alloy at different temperatures.

Fig. 3.13 shows the temperature dependence of the reciprocal susceptibility of $Mn_{1-x}Al_xNi_3$ alloys in the paramagnetic state. In the high temperature range the magnetic susceptibilities of all investigated samples obey the Curie-Weiss law, $\chi = C / (T-\theta)$. The magnetic susceptibility of ferrimagnetic materials follows a Néel-type hyperbolic law. However, the high temperature asymptote to the hyperbola is of Curie-Weiss form.

The transition Curie temperatures, the paramagnetic Curie temperatures and magnetic moments both in the ordered and paramagnetic state are given in Table 3.1.
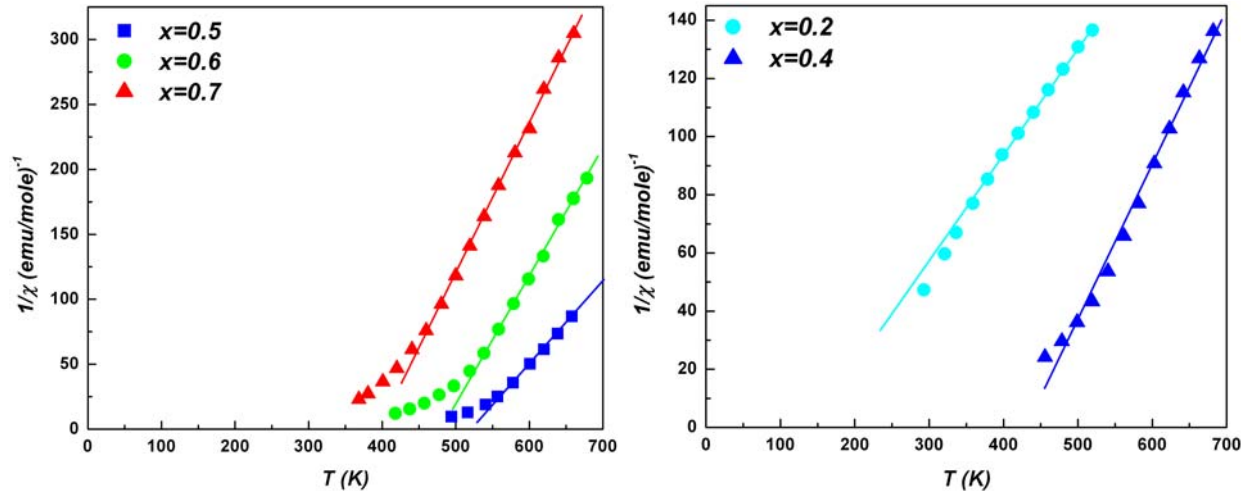
Fig. 3. 13. Reciprocal susceptibility versus temperature of $Mn_{1-x}Al_xNi_3$ alloys

Table 3.1. Curie temperatures T_c , paramagnetic Curie temperatures θ , magnetic moments in the ordered magnetic state (μ_s) and paramagnetic state (μ_{eff}) of $Mn_{1-x}Al_xNi_3$ alloys

Compound	T_C (K)	μ_s (μ_B/f.u.)	θ (K)	μ_{eff} (μ_B/f.u.)
$Mn_{0.8}Al_{0.2}Ni_3$	205	1.02	137	4.7
$Mn_{0.6}Al_{0.4}Ni_3$	464	1.56	426	3.9
$Mn_{0.5}Al_{0.5}Ni_3$	495	1.86	518	3.6
$Mn_{0.4}Al_{0.6}Ni$	407	1.6	477	2.9
$Mn_{0.3}Al_{0.7}Ni_3$	335	1.42	397	2.6

In Fig. 3.14, the values of the Curie temperature T_C and paramagnetic Curie temperature θ obtained in the present work are plotted together with the values of T_C from earlier magnetic measurements, versus Al content for $Mn_{1-x}Al_xNi_3$ alloys.
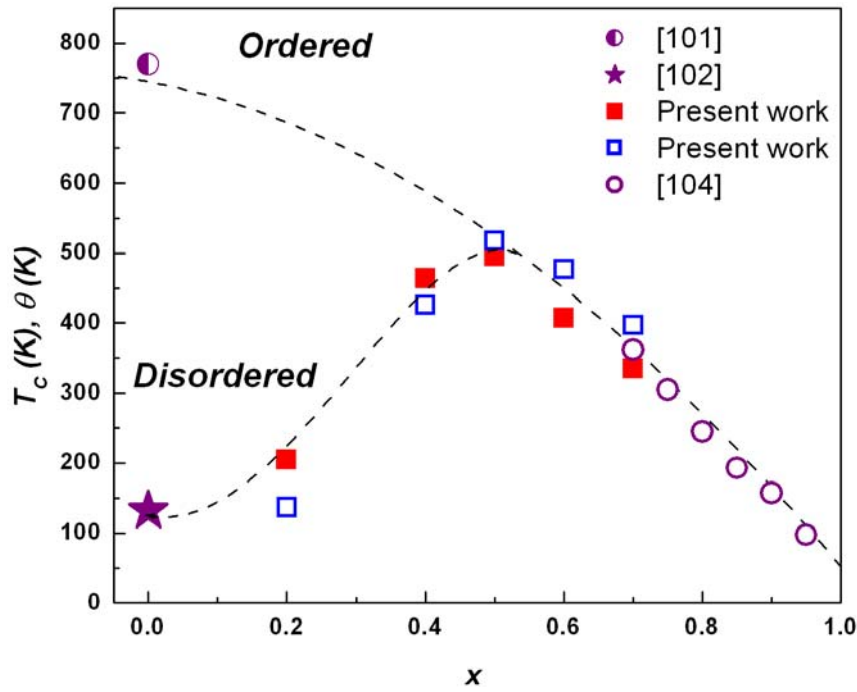
Fig. 3.14. Curie temperatures T_C and paramagnetic Curie temperatures θ of $Mn_{1-x}Al_xNi_3$ alloys as a function of Al content. The broken lines are guides for the eyes.

There is a good agreement between our results concerning the Curie temperatures T_C for $x \geq 0.5$ and those reported earlier on crystallographically ordered samples. On the other hand, the Curie temperatures for $x < 0.5$ are smaller than the expected values for ordered alloys (the upper broken line in Fig. 3.14). These results suggest an increase in the crystallographic ordering of $Mn_{1-x}Al_xNi_3$ alloys as the Al content increases. The monotonic decrease of T_C with Al concentration in the ordered state may be explained by the reduction of the number of ferromagnetic Mn - Ni pairs. On the contrary, in the disordered state T_C increases with Al content due to the decrease in the number of antiferromagnetic Mn - Mn pairs. The paramagnetic Curie temperatures θ for ordered alloys are higher than the transition Curie temperatures T_C, as is expected for a ferromagnetic material, while in the disordered state, $\theta < T_C$, characteristic for a ferrimagnetic behaviour.

The correlation of XPS data and magnetic measurements for ordered and paramagnetic states suggests the existence of local magnetic moments on the Mn and Ni sites in $Mn_{1-x}Al_xNi_3$ alloys. The compound $AlNi_3$, which is known as a spin fluctuation system, has the Ni 3d band almost filled with a magnetic moment in the ordered state of $\mu = 0.075$ μ_B/Ni [34]. The Mn and Ni magnetic moments in $MnNi_3$ compound, both in ordered and disordered crystallographically state, have the values of 3.2 μ_B and 0.3 μ_B, respectively [103,112]. The band structure calculations on ferromagnetic $Ni_{0.5}Mn_{0.5-x}Al_x$ alloys have shown that the hybridization between

61

the Mn 3d and Al 3sp states is very low and the Mn magnetic moment is not affected by the presence of Al atoms in the lattice [113]. One can assume that the Mn magnetic moment in $Mn_{1-x}Al_xNi_3$ alloys has approximately the same value of 3.2 μ_B as in the parent compound $MnNi_3$. On the other hand, the Ni magnetic moment in Ni-Al alloys decreases linearly with the Al content in the range of solid solubility [114]. With this assumption, when the Al concentration in $Mn_{1-x}Al_xNi_3$ increases, the magnetic moment of Ni atom in the ordered magnetic state would linearly decrease from 0.3 μ_B/Ni in $MnNi_3$ to 0.075 μ_B/Ni in $AlNi_3$. This is also confirmed by our XPS measurements. The disorder degree D in $Mn_{1-x}Al_xNi_3$ alloys can be calculated in this way from the values of the magnetic moments in the ordered magnetic states μ_s. In the paramagnetic state, one can estimate the effective magnetic moment of Ni atoms from the Curie constant, $C_{f.\,u} = C_{Mn} + C_{Ni}$. In Table 3.2 are given the estimated values of the disorder degree and the magnetic moments per Ni atom both in the ordered (μ_s^{Ni}) and paramagnetic state (μ_{eff}^{Ni}).

Table 3.2. Disorder degrees D (%) and magnetic moments of Ni atoms in the ordered state (μ_s^{Ni}) and paramagnetic state (μ_{eff}^{Ni}) of $Mn_{1-x}Al_xNi_3$ alloys

Compound	$Al_{0.2}Mn_{0.8}Ni_3$	$Al_{0.4}Mn_{0.6}Ni_3$	$Al_{0.5}Mn_{0.5}Ni_3$	$Al_{0.6}Mn_{0.4}Ni_3$	$Al_{0.7}Mn_{0.3}Ni$
D (%)	45	15	10	7	0
μ_s^{Ni} (μ_B)	0.25	0.21	0.19	0.16	0.14
μ_{eff}^{Ni} (μ_B)	1.70	1.32	1.23	0.75	0.74

The inequality $p_c > p_s$ between the numbers of spins per Ni atom in the paramagnetic state p_c and ordered magnetic state p_s is valid for all investigated alloys and the ratio p_c / p_s decreases with the Al content. We may explain the contribution of Ni atoms to the measured susceptibility in $Mn_{1-x}Al_xNi_3$ alloys in terms of the self-consistent renormalization theory of spin fluctuations [34]. This theory has revealed that only a small-q part of the wave-number-dependent susceptibility χ_q contributes to the temperature dependence of χ in nearly ferromagnetic metals (exchange-enhanced Pauli paramagnets). The average amplitude of the local spin fluctuations on Ni sites $<S_L^2> = 3k_BT\sum_q \chi_q$ increases with temperature until it reaches an upper limit determined by the charge neutrality condition. The temperature dependence of χ at low temperatures is the result of the increase of local moments with increasing temperature. The amplitude $<S_L^2>$ of thermally excited longitudinal spin fluctuations saturates at certain temperature T* above which the susceptibility is governed by local moment type fluctuations and therefore a Curie-Weiss behaviour is observed. The partial filling of the Ni 3d band with the

increase of Al concentration   leads to a decrease of the spin fluctuations amplitude and consequently a reduction of the ratio p_c / p_s is observed.

3.4 Electronic structure calculations

In the following pages are presented the Band structure calculations of $Mn_{1-x}Al_xNi_3$ alloys ($0 \leq x \leq 0.8$) in order to evidence the effects of the Mn substitution by Al on the local Mn and Ni magnetic moments and to compare these values with the experimental ones. The disorder degree influence on the magnetic moments of the $Mn_{1-x}Al_xNi_3$ alloys is also investigated. The XPS valence band spectra and the density of states were calculated and compared to the experimental results.

Band structure calculations in ferromagnetic spin configuration (with all Mn and Ni magnetic moments parallel) have been performed for $Mn_{1-x}Al_xNi_3$ alloys in order to determine the dependence of the magnetic moments on the disorder degree and the Al content. The variation of Mn and Ni magnetic moments with the Al content is presented in Fig. 3.15.

The magnetic moments of Mn and Ni on their proper sites (1a and 3c, respectively) are different affected by the Mn substitution with Al and by the disorder degree in the system, respectively. On can observe that the calculated magnetic moments of Ni (3c) atoms decrease when Al concentration increases, whilst the calculated magnetic moments per Mn (1a) atoms suffer minor changes. The disorder degree has opposite influence on the magnetic moment of Mn 1a and Ni 3c sites: the Mn1a magnetic moments decrease when the disorder degree increases, for all $Mn_{1-x}Al_xNi_3$ alloys, whilst the Ni 3c magnetic moments increase with the disorder degree. The variation of the Mn 1a magnetic moments with Al content and with the disordered degree is small (about 5% when Al content increases from x = 0 to 0.8 and ~ 8% when D increases from 0 to 0.45, respectively). More pronounced is the effect of the Mn substitution by Al on Ni 3c magnetic moment: the Ni 3c magnetic moment in ordered compound decrease from 0.48 to almost zero when Al content increase to x = 0.8. The disorder increases the Ni 3c magnetic moment, i.e. in $Mn_{0.8}Al_{0.2}Ni_3$ for D = 0.45, μ_{Ni3c} is about 20% larger compared with the value of ordered alloy. We expect that the decrease of the magnetic moments of Ni 3c with Al content is a consequence of the partial filling of the Ni 3d band due to hybridization between Ni 3d and Al 3sp states, this effect being much less pronounced for Mn 3d bands.
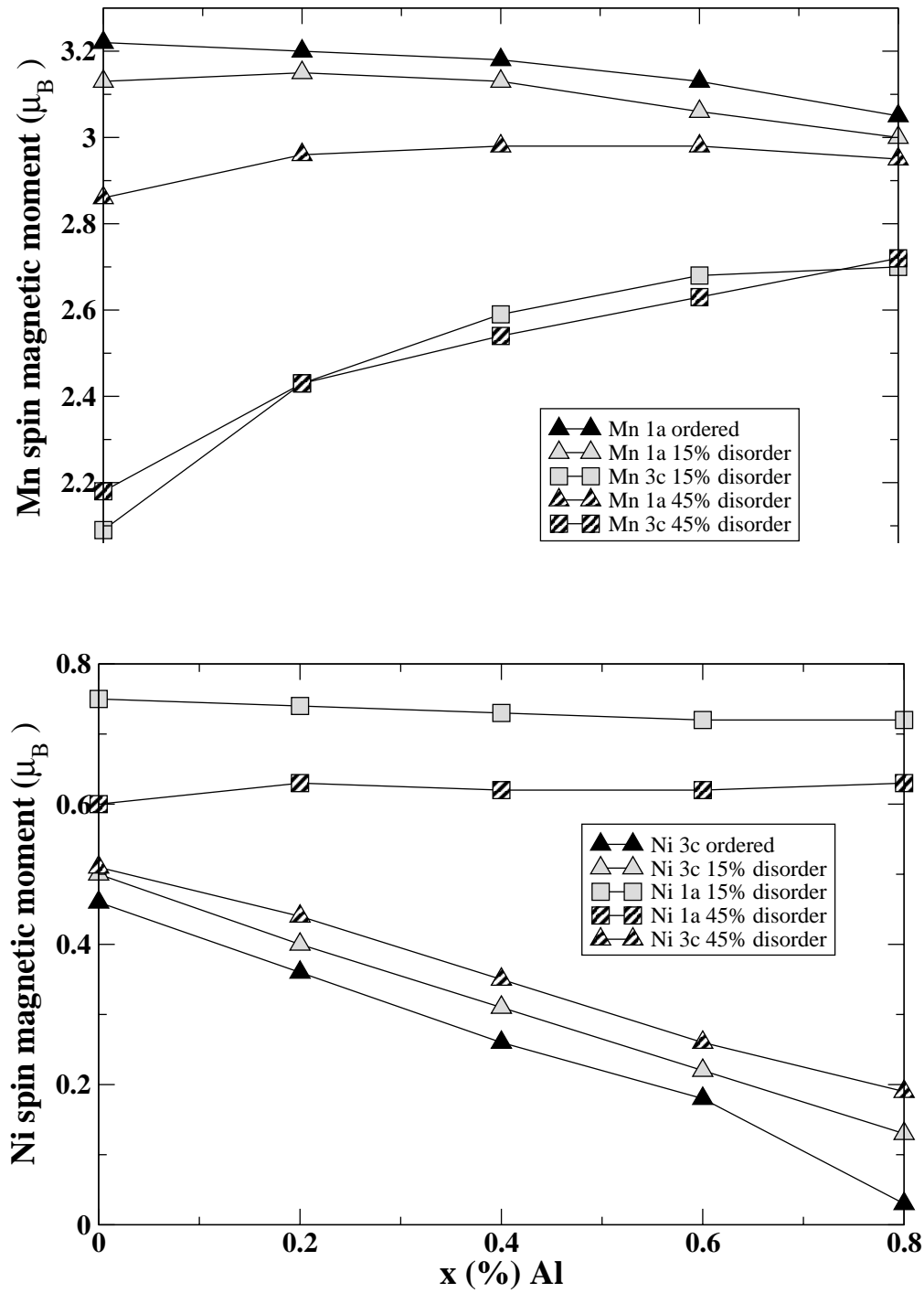
Fig.3.15. Calculated magnetic spin moments of Mn and Ni atoms in $Mn_{1-x}Al_xNi_3$ alloys, using different disorder degrees.

Furthermore, the Mn and Ni magnetic moments on antisites (Mn 3c and Ni 1a, respectively) are much different from the corresponding magnetic moments of Mn and Ni sitting on their proper positions. The Mn magnetic moments are smaller when Mn atoms are on antisites due to the decrease of Mn-Mn distance ($d_{Mn1a-Mn3c} \approx 2.53$ Å), which leads to the increase of the delocalization degree of the Mn 3d electrons. On the other hand, the Mn 3c magnetic

moments increase with the Al content. The influence of the crystallographic disorder on the Mn magnetic moment on antisite is negligible. The 3d band width $\Delta \approx Z^{1/2}J_h$ depends on the number of near-neighbours Z with d orbitals and the hopping integral J_h, which is very sensitive to the distance between the atoms. In case of Mn (3c) atoms the number of near-neighbours having d orbital decreases when Al concentration increases. This means that the 3d band becomes narrower, 3d electrons are more localized, and all these leads to an increase of Mn magnetic moment.

Also, the Ni magnetic moment on antisite is much higher than the Ni sitting on the proper site but is less influenced by the Al content. This could be assign to the fact that Ni 1a atoms do not have Al atoms in their first vicinity. In the case of $Mn_{0.8}Al_{0.2}Ni_3$ alloy, with high D values, there is a significant influence of the disorder degree on the Ni 1a magnetic moment (Fig.3.15). The orbital magnetic moment is not completely quenched by the crystal field, but his contribution to the total magnetic moment is very small.

The Mn and Ni magnetic moments in the $Mn_{1-x}Al_xNi_3$ alloys, using the disorder degree D determined by experiment, are presented in Table 3.3.

In Fig. 3.16 are shown the calculated and experimental magnetic moments per unit cell in $Mn_{1-x}Al_xNi_3$ alloys.

Table 3.3. The calculated Mn and Ni magnetic moments in the $Mn_{1-x}Al_xNi_3$ alloys using the experimental determined disorder degrees

		$Mn_{0.8}Al_{0.2}Ni_3$ D=0.45	$Mn_{0.6}Al_{0.4}Ni_3$ D=0.15	$Mn_{0.5}Al_{0.5}Ni_3$ D=0.12	$Mn_{0.4}Al_{0.6}Ni_3$ D=0.07	$Mn_{0.3}Al_{0.7}Ni_3$ D=0
Mn 1a	spin	2.96	3.13	3.11	3.13	3.04
	orbit	0.02	0.02	0.02	0.02	0.02
Ni 1a	spin	0.63	0.73	0.72	0.72	
	orbit	0.07	0.11	0.12	0.13	
Al 1a	spin	-0.05	-0.05	-0.04	-0.03	-0.03
	orbit	0	0	0	0	0
Mn 3c	spin	2.43	2.59	2.65	2.70	
	orbit	0.02	0.02	0.02	0.02	
Ni 3c	spin	0.44	0.31	0.26	0.18	0.15
	orbit	0.03	0.02	0.01	0.01	0.01
Total/f.u	spin	3.55	2.78	2.30	1.84	1.34
	orbit	0.11	0.08	0.05	0.04	0.02
μs experimental		1.02	1.56	1.86	1.6	1.42
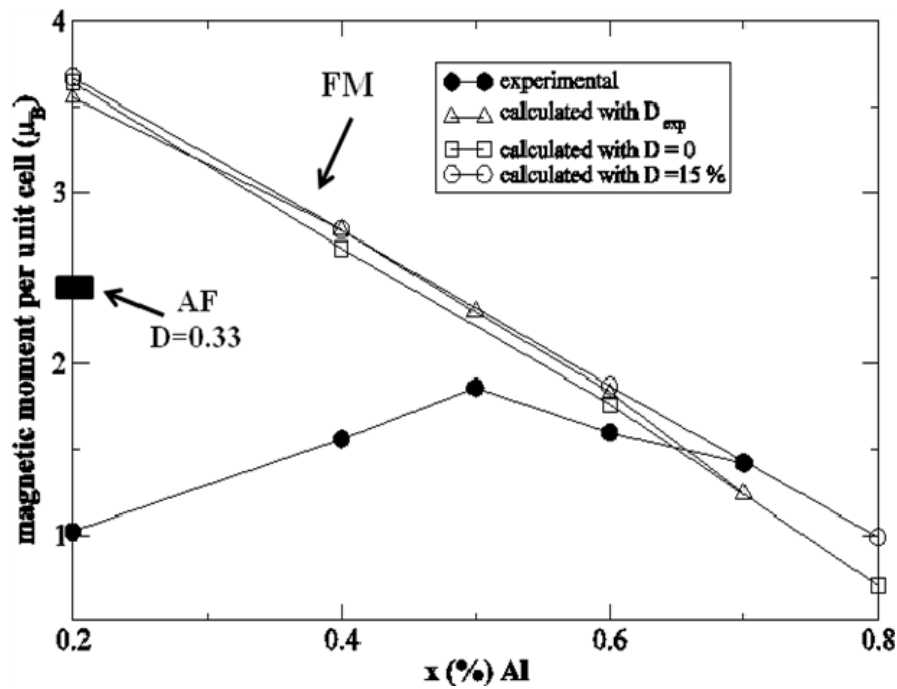
Fig.3.16. The magnetic moments per unit cell in $Mn_{1-x}Al_xNi_3$ alloys

The calculated total magnetic moment per unit cell, using the experimental determined disorder degrees is in reasonable agreement with the magnetic moment per unit cell determined from magnetization measurements, only for $x \geq 0.5$. The change of the disorder degree in the theoretical calculations doesn't improve this agreement.

The measured values of the magnetic moments per unit cell for $x \leq 0.4$ are much smaller than those predicted by the ferromagnetic spin configuration, confirming the existence of Mn-Mn pairs antiferromagnetically coupled. This is in good agreement with experimental results where ferrimagnetic behaviour of the alloys in this concentration range was evidenced. In Fig. 3.16 is given also the value of the calculated magnetic moment per unit cell for x=0.2 and a disorder degree D=0.33, considering the antiferromagnetic coupling between the Mn1a and Mn3c atoms. Higher values of the disorder degree lead to smaller magnetic moments per unit cell, in good agreement with our experimental findings.

The XPS valence band spectra were also calculated with the Munich SPR-KKR package in order to allow a direct comparison of the computed and experimental XPS valence band spectra. The calculated and experimental XPS valence band spectra of $Mn_{1-x}Al_xNi_3$ alloys are presented in Fig. 3.17. At Al K_α radiation, the Ni 3d cross section is about four times larger than the Mn 3d cross section, and also the Ni atomic concentration is at least 3 times larger than Mn concentration, i.e., the XPS valence band spectra for all $Mn_{1-x}Al_xNi_3$ alloys and compounds is dominated by the Ni 3d states (see Fig. 3.17). The Mn contribution to the XPS spectra has a

maximum at about 4 eV binding energy, which is visible in some of the spectra by a shoulder in the total intensity. The satellite structures at about 6.5 eV are caused by the enhanced electron correlation in the Ni 3d band, providing an evidence for the unoccupied states in the Ni 3d band. The decrease of the Ni 2p satellite intensity with increasing the Al content confirms the partial filling of the Ni 3d band by hybridization with the Al 3sp states. The correlation effects have not been implemented in the theoretical framework and this feature is absent in the theoretical spectra. The calculated XPS valence band spectra describe the main characteristics of the experimental ones. The contribution of the Mn 3c and Ni 1a in the calculated XPS valence band
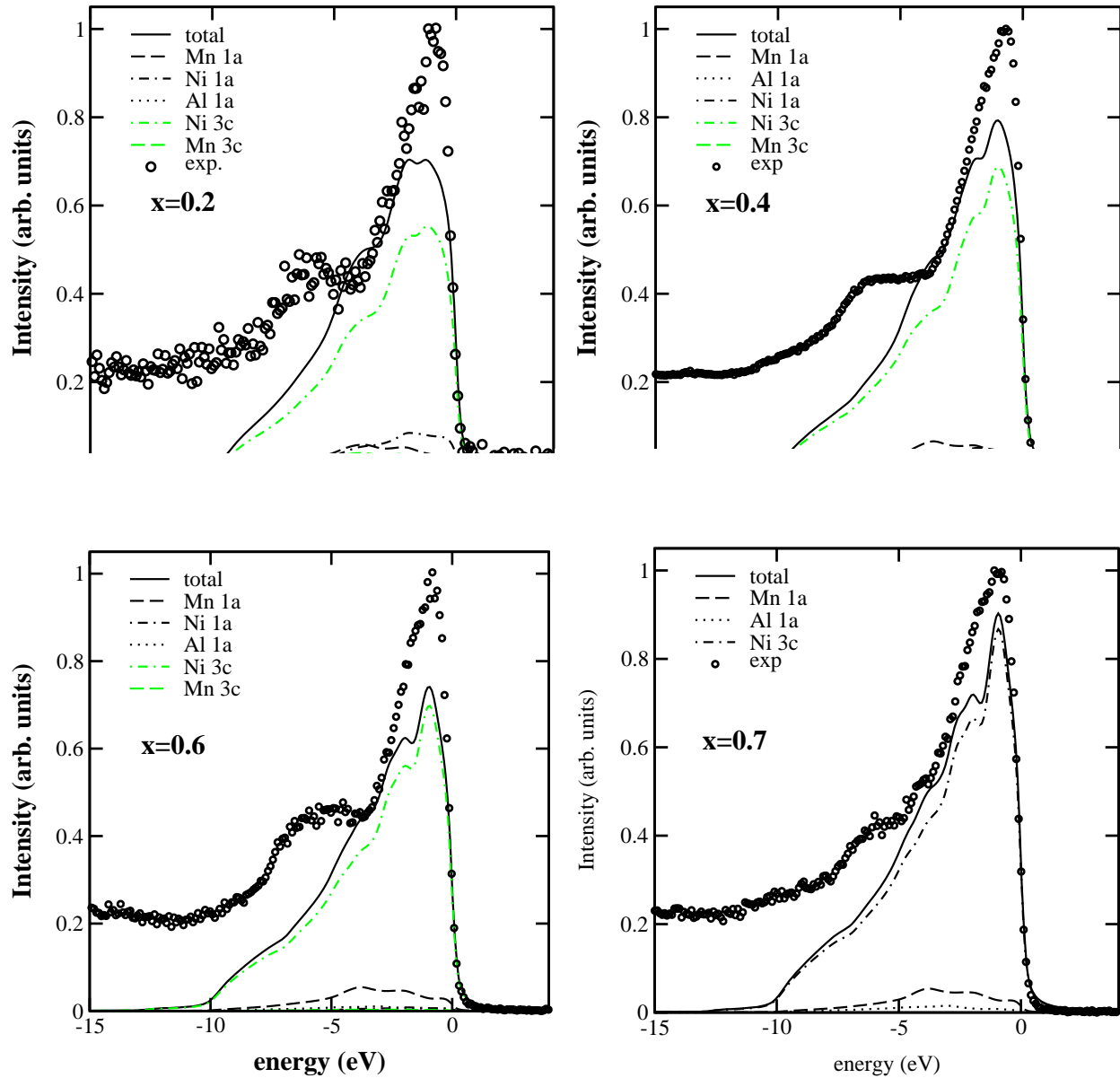
Fig.3.17. Calculated (lines) and experimental (circles) XPS valence band spectra of Mn$_{1-x}$Al$_x$Ni$_3$ alloys for x = 0.2, 0.4, 0.6 and 0.7.

The total DOS calculations for investigated alloys are presented in Fig. 3.18. On can see that there are no changes on the DOS at Fermi level in the spin-up band but there is a significant decrease of DOS in the spin-down band when Al concentration increases, suggesting a partial filling of the Ni 3d band due to the hybridization between Ni 3d and Al 3sp states.
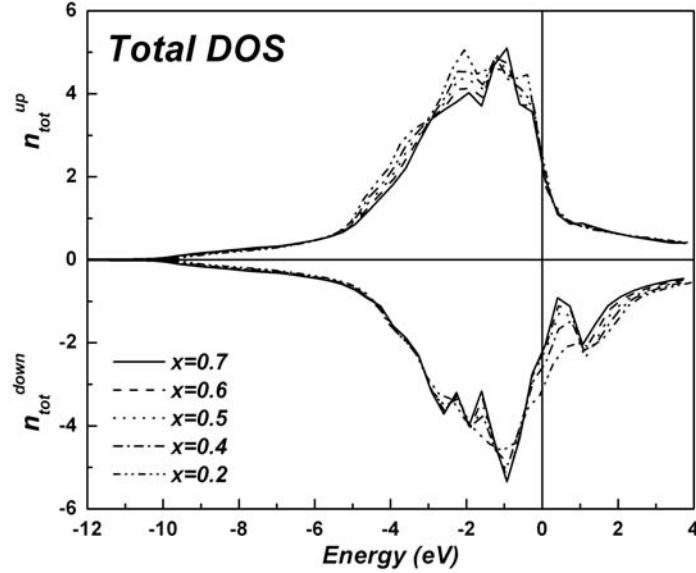
Fig.3.18. Total spin resolved DOS of $Mn_{1-x}Al_xNi_3$ alloys

3.5 Conclusions

➢ The substitution of Al for Mn in $MnNi_3$ leads to significant changes in the crystallographic order with remarkable effects on the magnetic properties and electronic structure of $Mn_{1-x}Al_xNi_3$ alloys.

➢ The as-prepared alloys are crystallographically disordered for $x \leq 0.5$, but the crystallographic disorder degree decreases quickly for higher Al concentration.

➢ Aluminum plays an important role in stabilizing the crystallographic ordered structure in $Mn_{1-x}Al_xNi_3$ alloys.

➢ XPS spectra and magnetic measurements pointed out the existence of local magnetic moments on Mn and Ni sites in both crystallographically ordered and disordered $Mn_{1-x}Al_xNi_3$ alloys.

➢ The hybridization between the 3d Ni and 3sp Al states leads to a partial filling of the Ni 3d band, as indicated by the XPS core level and valence band spectra.

➢ The temperature dependence of the reciprocal susceptibility of the investigated alloys may be explained in terms of the self-consistent renormalization theory of spin fluctuations.

- The effective magnetic moment induced by the spin fluctuations decrease with the gradually filling of Ni 3d band.
- The Mn and Ni magnetic moments in $Mn_{1-x}Al_xNi_3$ alloys, calculated with the spin polarized relativistic Korringa-Kohn-Rostocker method, depend on the disorder degree.
- The calculated magnetic moment of Ni (3c) atoms decreases when Al concentration increases, whilst the magnetic moments of Mn (1a) atoms suffer minor changes, confirming the experimental assumptions.
- The magnetic moments of Mn 3c are almost independent on the disorder degree, whilst the Ni 1a magnetic moments decrease with the disorder degree.
- The lower values of the saturation magnetization determined by measurements are associated with AF coupling of the Mn-Mn pairs.
- The XPS spectra and the total DOS calculations confirmed the partial filing of the Ni 3d band when Mn is replaced by Al.
- The valence band of $Mn_{1-x}Al_xNi_3$ alloys is dominated by the Ni 3d states and there is a good agreement between calculated and measured XPS valence band spectra.

Chapter 4

Electronic structure and magnetic properties
of $Mn_{1-x}Al_xNi$ alloys [115]

MnNi has one of the highest Néel temperature (T_N =1073K), a magnetic moment of 4 μ_B/Mn [116] and is used in the spin electronic devices as a pinning layer in the spin-valve structures [117]. AlNi is a Pauli paramagnet with the Ni 3d band completely filled at room temperature [118].

The magnetic properties of $Mn_{1-x}Al_xNi$ alloys have been studied only for a limited range of Al concentration, namely for x=0.4 [119, 120] and 0.5 [121]. For $MnAlNi_2 \equiv Mn_{0.5}Al_{0.5}Ni$ Heusler alloy was pointed out the coexistence of antiferromagnetism and ferromagnetism [121]. The $Mn_{0.6}Al_{0.4}Ni$ alloy, thermal treated for three days at 1273 K, exhibits the B2-10M martensitic transformation [120]. It was also shown that in the furnace-cooled specimen of the $Mn_{0.6}Al_{0.4}Ni$ alloy, the $L2_1$ structure appears and the B2-10M martensitic transformation is suppressed.
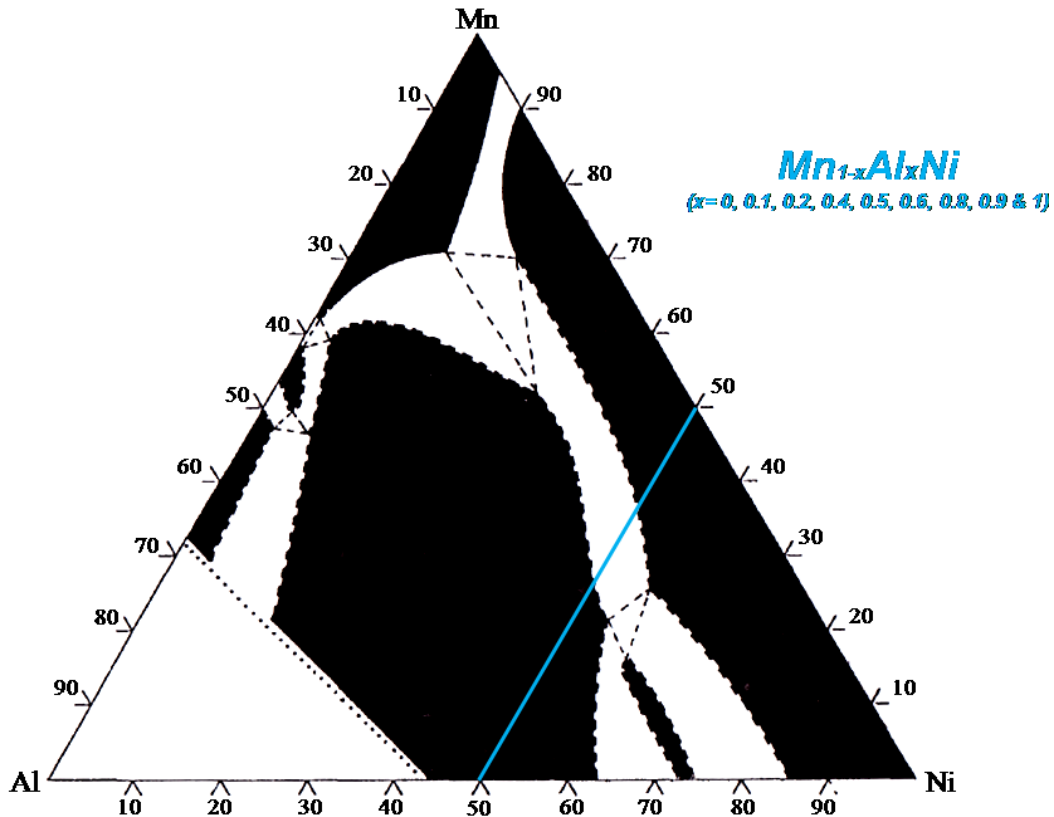
Fig. 4.1. Thernary phase diagram of Ni-Mn-Al alloys at T=1273K

According to the phase diagram of Al-Mn-Ni alloys (Fig. 4.1) there are two different regions of solid solubility for $Mn_{1-x}Al_xNi$ alloys (the blue line in the phase diagram); one in the small x region (x=0, 0.1, 0.2) and another in the high x region (x=0.5, 0.6, 0.8, 0.9, 1). The alloy corresponding to x=0.4 is in between, fact confirmed by XRD measurements (the alloy is not single phase).

The aim of this chapter is to extend the magnetic measurements to whole range of concentrations and to correlate the magnetic data with XPS spectra.

4.1 Structural characterization

Nine samples from the $Mn_{1-x}Al_xNi$ system (x= 0, 0.1, 0.2, 0.4, 0.5, 0.6, 0.8, 0.9, 1) were prepared. XRD measurements were performed on polished surfaces due to the hardness of the samples. The broad character of the peaks indicates the presence of the strains in the samples.
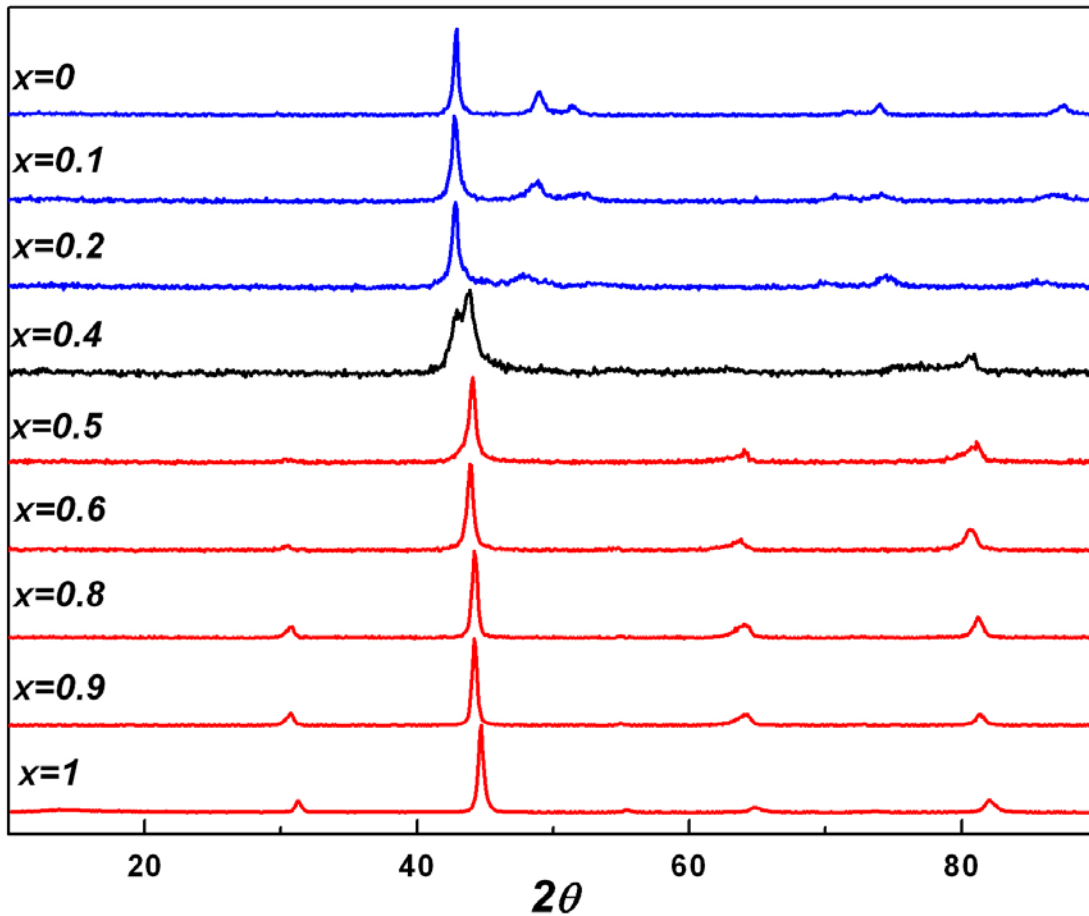
Fig. 4.2. X-ray diffraction pattern of $Mn_{1-x}Al_xNi$ alloys.

These measurements revealed a change in the crystallographic structure around x = 0.4 from CuAuI to CsCl (B2) structure type. In Fig. 4.2 are shown the XRD patterns for all investigated samples. $Mn_{0.6}Al_{0.4}Ni$ appears as a mixture of these two structures. The B2 phase has the same

structure with the L2$_1$ phase of Heusler alloys, having the unit cell equals with the 8-th part from the last one (see Fig. 4.3). In the B2 phase of Mn$_{1-x}$Al$_x$Ni alloys, the Mn and Al atoms are randomly arranged, thus the near-neighbor Mn-Mn distance is about 0.29 nm. In the L2$_1$ structure, where the Mn atoms are separated by Al atoms, the shortest Mn-Mn distance is 0.41 nm.
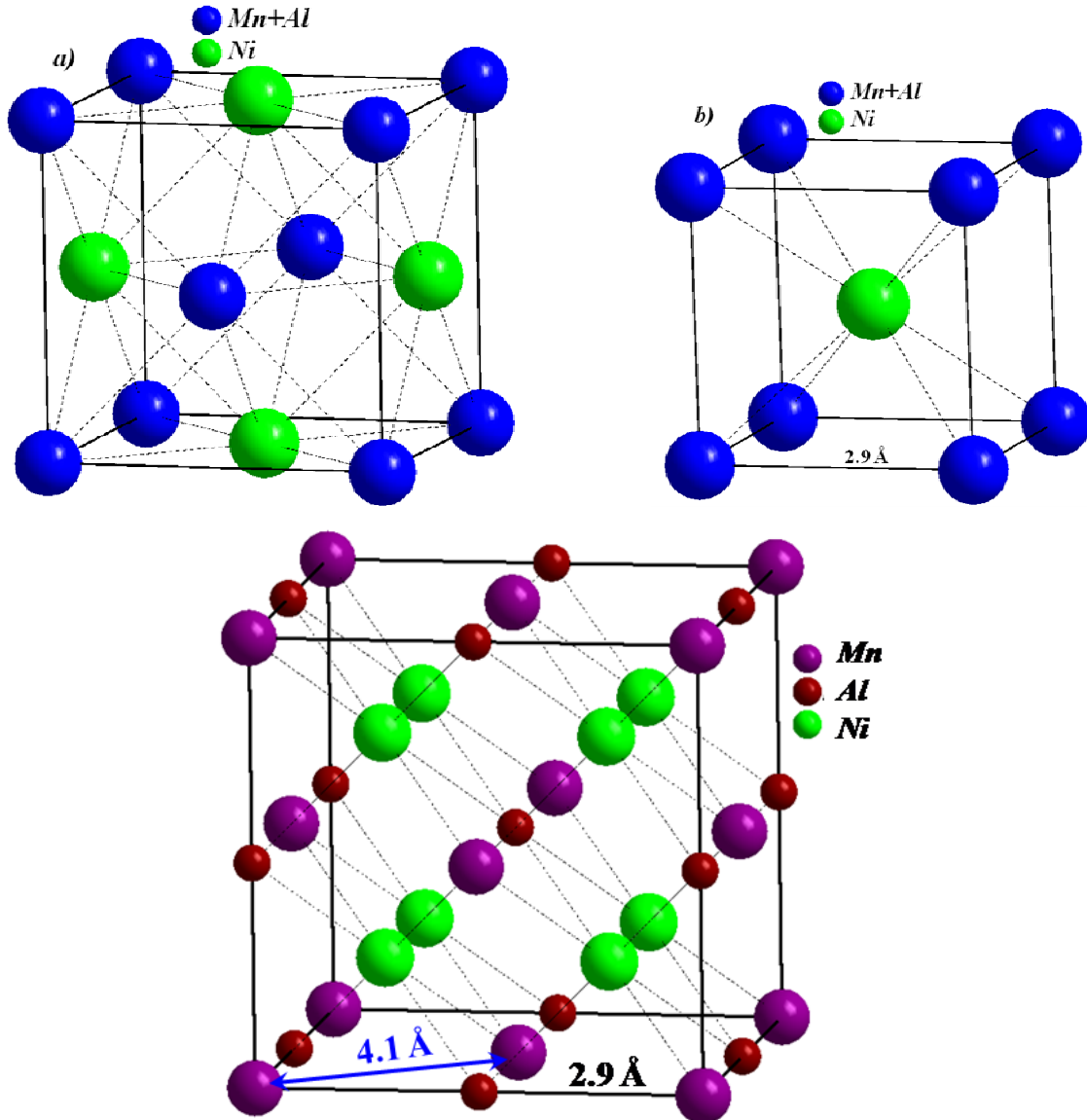
Fig.4.3. Representation of AuCu (a),ClCs (b) and Heusler (c) structure type

4.2 XPS Spectra

The samples were cleaved in situ. The surface cleanness was checked by monitoring the O 1s and C 1s core levels in the survey spectra (Fig. 4.4). The small content of oxygen and carbon in the samples is due to the contamination of the freshly cleaved surface.
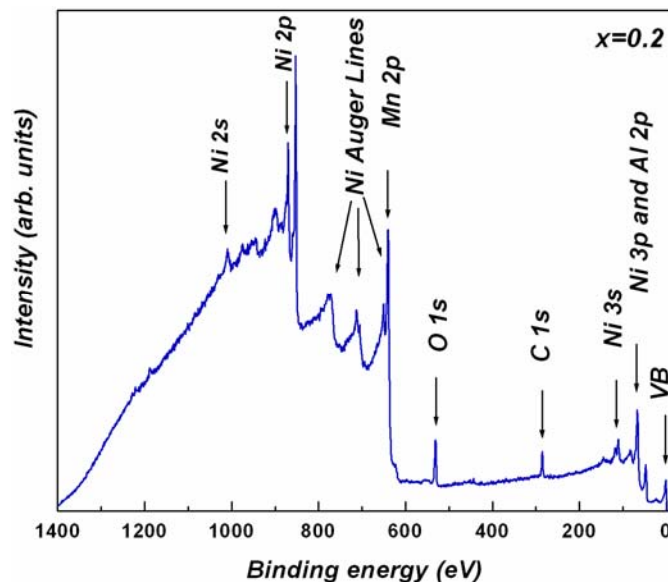
*Fig. 4.4 **S**urvey spectra of $Mn_{0.8}Al_{0.2}Ni$*

The Mn 3s spectra for MnNi, $Mn_{0.9}Al_{0.1}Ni$ and $Mn_{0.8}Al_{0.2}Ni$ are shown in Fig. 4.5. The shoulder around 79 eV corresponds to the Ni 3p satellite situated at about 12 eV higher binding energy from the main line [122].
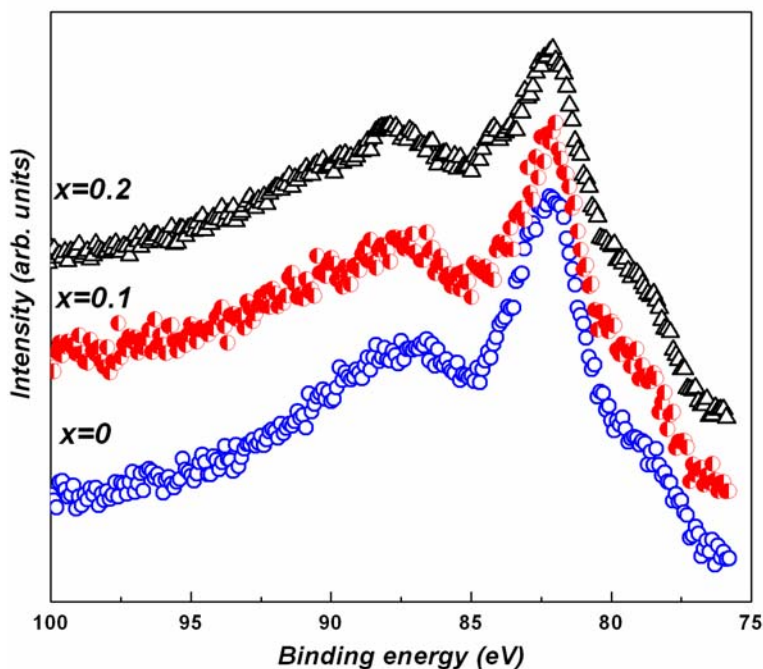
Fig. 4.5. Mn 3s XPS spectra of $Mn_{1-x}Al_xNi$ alloys

The experimental spectra were fitted with two components corresponding to Mn 3s exchange splitting, the Ni 3p satellite and a Shirley background type. Fig. 4.6 presents the curve fitting results of MnNi compound, after background and Ni 3p satellite subtraction. Similar results were obtained for the other two alloys $Mn_{0.9}Al_{0.1}Ni$ and $Mn_{0.8}Al_{0.2}Ni$. All spectra exhibit a well-defined magnetic exchange splitting of about 5 eV, arising from the exchange interactions

73

between the 3s core hole and open Mn 3d shell. This splitting corresponds to a spin S≈2 and a magnetic moment of $4\mu_B$/Mn, suggesting that Mn 3d band is not affected by the hybridization with Al sp states. This splitting is a direct evidence for the existence of local magnetic moment confined on Mn sites.
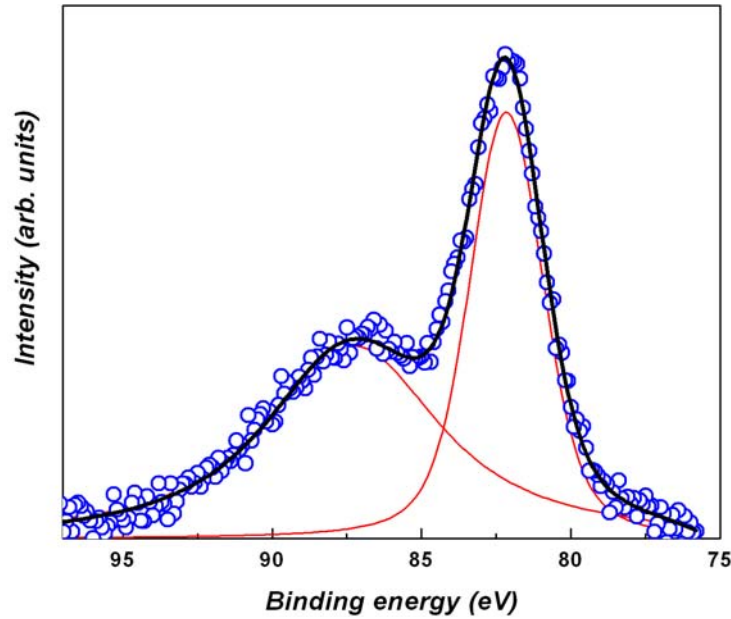
Fig. 4.6. Mn 3s curve fitting results of MnNi compound

There is an overlapping between Mn2p XPS line and Ni $L_2M_{23}M_{45}$ Auger line (Fig. 4.7). In order to see the multiplet splitting of Mn $3p_{3/2}$ line the Auger line was subtracted.
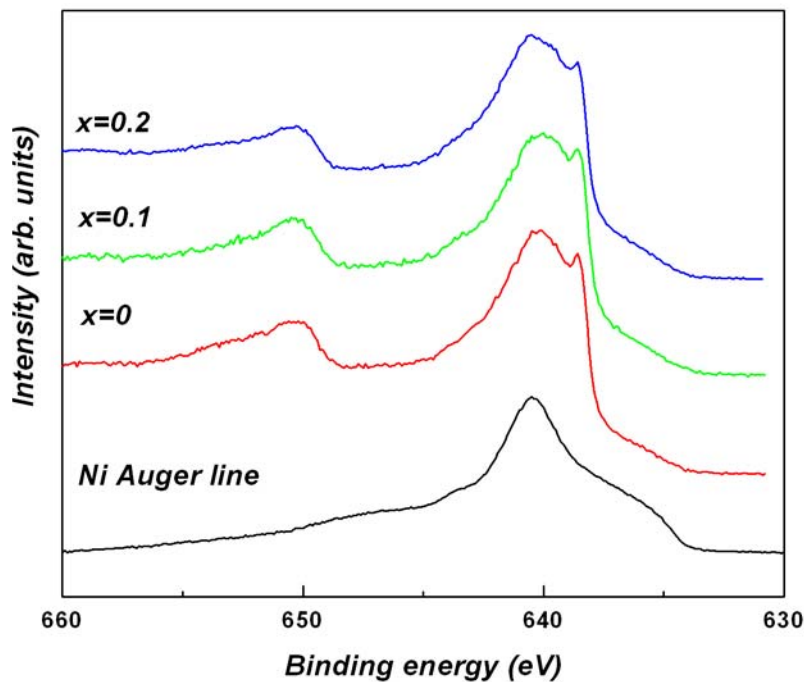
Fig. 4.7. Mn 2p XPS spectra of $Mn_{1-x}Al_xNi$ alloys and Ni Auger line

The subtraction of the Ni Auger line was made in two steps. First the survey spectrum of pure Ni metal was normalized to 1 in order to see the relative intensity of the Ni Auger line and Ni 2p line. Using this ratio, in the normalized survey spectrum of the investigated alloys (again the most intense line is Ni 2p), the relative intensity of the Ni Auger line and the total measured line (Mn 2p+Ni Auger) line was estimated. Then the high resolution lines of Ni Auger from Ni metal and measured spectrum (Ni Auger+Mn2p) were normalized to this relative intensity. In the second step a superposition of the Ni Auger line and measured spectrum, in the 637-634 eV region was considered; in this region the only contribution to the measured spectrum comes from Ni Auger line (see Fig. 4.7). The Mn 2p core-level spectra for MnNi, $Mn_{0.9}Al_{0.1}Ni$ and $Mn_{0.8}Al_{0.2}Ni$ after the subtraction of Ni Auger line are given in Fig. 4.8. The first vicinity of Mn atoms in the $Mn_{1-x}Al_xNi$ alloys does not change by alloying, what explains the lack of the chemical shift in the Mn 2p spectra.
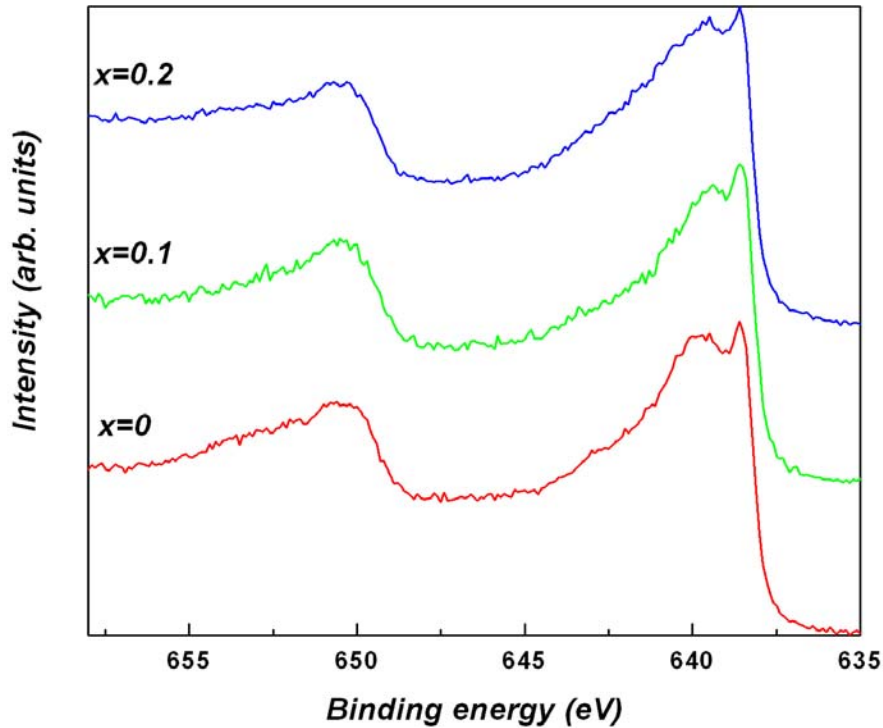
Fig. 4.8. Mn 2p XPS spectra of $Mn_{1-x}Al_xNi$ alloys after the subtraction of the Ni Auger Line

The observed spin orbit splitting, which can be identified in the distance between the two centers of energy of the $2p_{3/2}$ and $2p_{1/2}$ state is $\Delta_{so} \approx 11.5$ eV. Both these states are accompanied by broad features at about 5 eV towards higher binding energies. The whole spectrum can be explained if we assume more than one $3d^n$ final state configuration. The ground state is mainly the $3d^6$ state with a small admixture of $3d^5$ configuration, representing states of local moments in the Anderson's model. Upon creation of a 2p hole one may expect thus a well-screened state

$2p^53d^6$ and a poorly screened $2p^53d^5$ final state. Focusing on the states associated with $2p_{3/2}$ ionization, there are structures between 638 and 642 eV and a broad feature at about 644.5 eV. Similar results were reported for Mn 2p core level photoelectron spectra of Mn films deposited on Ag (100) [123], Ni (110) [124], Cu (100) [125], Pd(100) [126] and of Mn-Pd alloys and compounds [127]. A large magnetic moment was derived for Mn (about 4 μ_B) in all these systems, similar to those found for Mn in $Mn_{1-x}Al_xNi$ alloys. In all these cases, the 5 eV satellite located at about 645 eV was assigned to a $2p^53d^5$ final state configuration, whereas the main line centered at about 639 eV was associated with a $2p^53d^6$ final state configuration. The line shapes of 2p core-level photoemission spectra for 3d metals are strongly influenced by the simultaneous occurrence of spin-orbit coupling and exchange splitting between the core hole and the valence electrons. The theoretical approach to the problem of core-level photoemission is done within a fully relativistic generalization of the one-step model of photoemission. Ebert et al. found in the calculated spectra a splitting of $2p_{3/2}$ and $2p_{1/2}$ states into four and respectively two sublevels [128]. Due to the presence of the spin polarization, the 2p sublevels of 3d metals posses no unique total angular-moment character, i.e., j is no longer a good quantum number. Because the effect of the exchange splitting is small compared to that of spin-orbit splitting, the 2p subsheels can still be labeled as $2p_{1/2}$ and $2p_{3/2}$. In this case, the magnetic quantum number μ is still left as a good quantum number and the 2p sublevels are μ=-1/2, +1/2 for $2p_{1/2}$ and μ=-3/2, -1/2, +1/2, +3/2 for $2p_{3/2}$ [129].
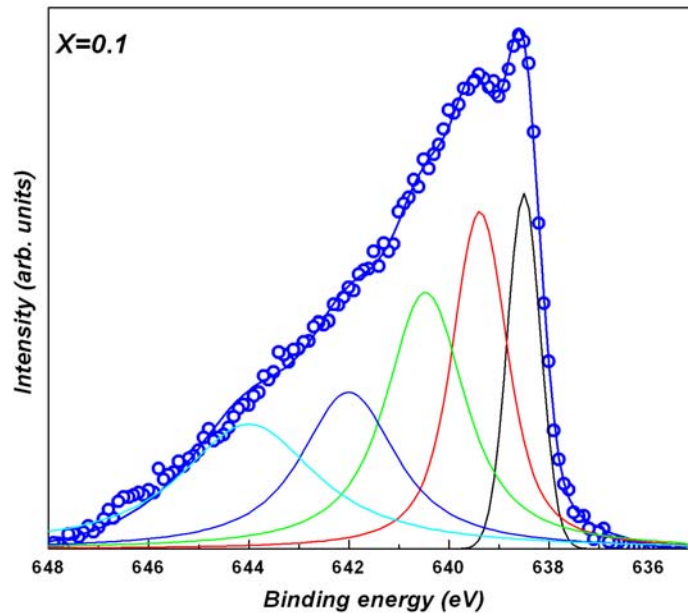
Fig. 4.9. Mn $2p_{3/2}$ curve fitting results of $Mn_{0.9}Al_{0.1}Ni$ alloy

By using the fully relativistic photoemission calculations for Mn-based Heusler alloys, Plogmann *et* al. found a splitting of the $2p_{3/2}$ states into four sublevels, with an energy separation

of 1.0-1.5 eV for all the alloys [130, 131]. After background removal, using a Shirley-type background shape [132], we have also fitted the Mn $2p_{3/2}$ core-level spectra for some of the investigated alloys with four components and a satellite line situated at binding energy around 644.5 eV. The curve fitting results for $Mn_{0.9}Al_{0.1}Ni$ is given in Fig. 4.9, with the mean energy separation $\Delta_{ex}\approx1.1$ eV. This gives further evidence of the existence of local moments confined on Mn sites.

The Ni 2p core-level spectra of $Mn_{1-x}Al_xNi$ alloys are shown in Fig. 4.10. The Ni $2p_{3/2}$ core level spectra for x≤0.8 exhibit satellite structures situated at about 6.5 eV higher binding energy than the main line.
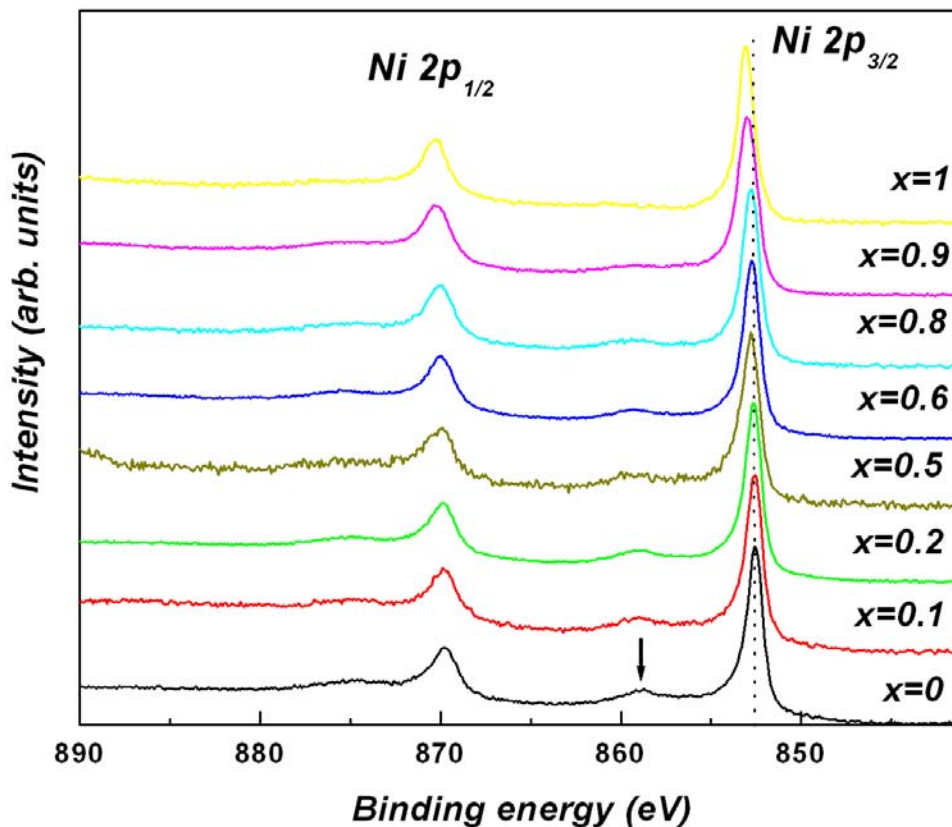
Fig .4.10. Ni 2p XPS spectra of $Mn_{1-x}Al_xNi$ alloys

The observation of satellites implies the presence of d character in the unoccupied bands. The satellite structure intensity decreases as the Al content increases, indicating a gradual filling of the Ni 3d band. This is due to a strong hybridization between Ni 3d and Al 3sp states.

For a better illustration of the satellite structure, in Fig. 4.11, the Ni 2p line of MnNi compound was fitted with four components: two corresponding to the spin-orbit splitting doublet (Ni $2p_{3/2}$ and Ni $2p_{1/2}$) and other two assign to the satellite structures.
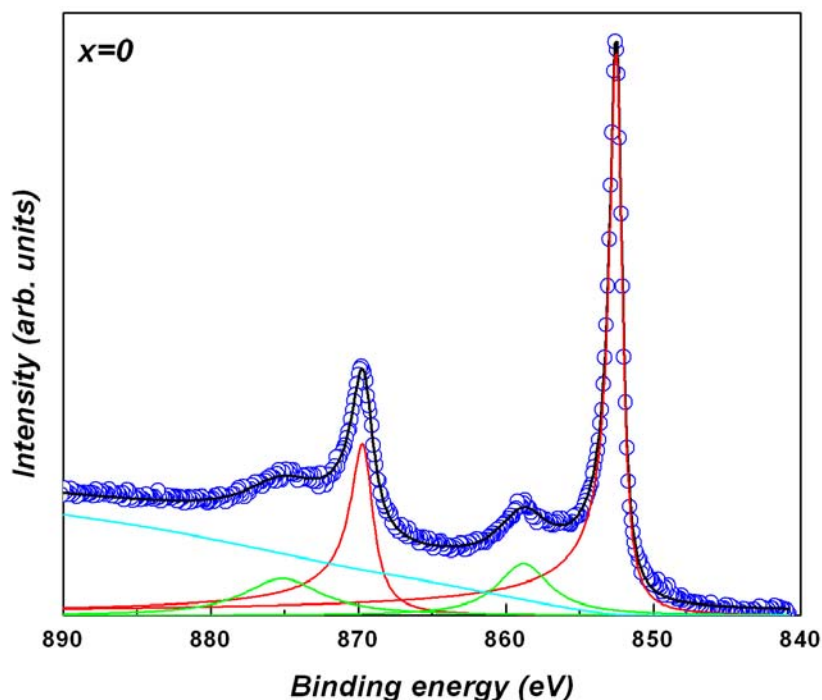
Fig .4.11. Ni 2p curve fitting results of MnNi compound

The complete filling of the Ni 3d band, at room temperature, for AlNi Pauli paramagnet is confirmed by the absence of the satellite structures. The presence of the satellite structures suggests that Ni atoms could carry a small magnetic moment, but previous studies have shown that in MnNi the Ni atoms have no magnetic moments [133]. This means that even in the presence of some unoccupied states in the Ni 3d band the Anderson condition for the existence of the local moment at the Ni site in the ordered magnetic state is not fulfilled. As the Al concentration increases, the Ni 2p core-level lines are shifted to higher binding energy. These small chemical shifts are due to the change in the filling degree of the Ni 3d band, which leads to an increase in the electronic density around the Ni 2p shell.

The XPS valence band spectra of $Mn_{1-x}Al_xNi$ alloys are shown in Fig. 4.12. The Ni 3d cross section for Al K_α radiation is about four times larger than the Mn 3d cross section, i. e., the valence bands of $Mn_{1-x}Al_xNi$ alloys are dominated by Ni 3d states. The valence band of Pauli paramagnet AlNi results as a superposition of the Ni 3d band, centered at about 2 eV, and the Al sp states in the Fermi level region. The XPS valance band spectra of investigated samples present a small satellite structures at about 6.5 eV, which decreases in intensity with the increase of Al content. The 3d bands are shifted towards higher binding energies as the Al concentration increases, suggesting a gradual filling of the Ni 3d band due to the hybridization of Al 3sp and Ni 3d states.
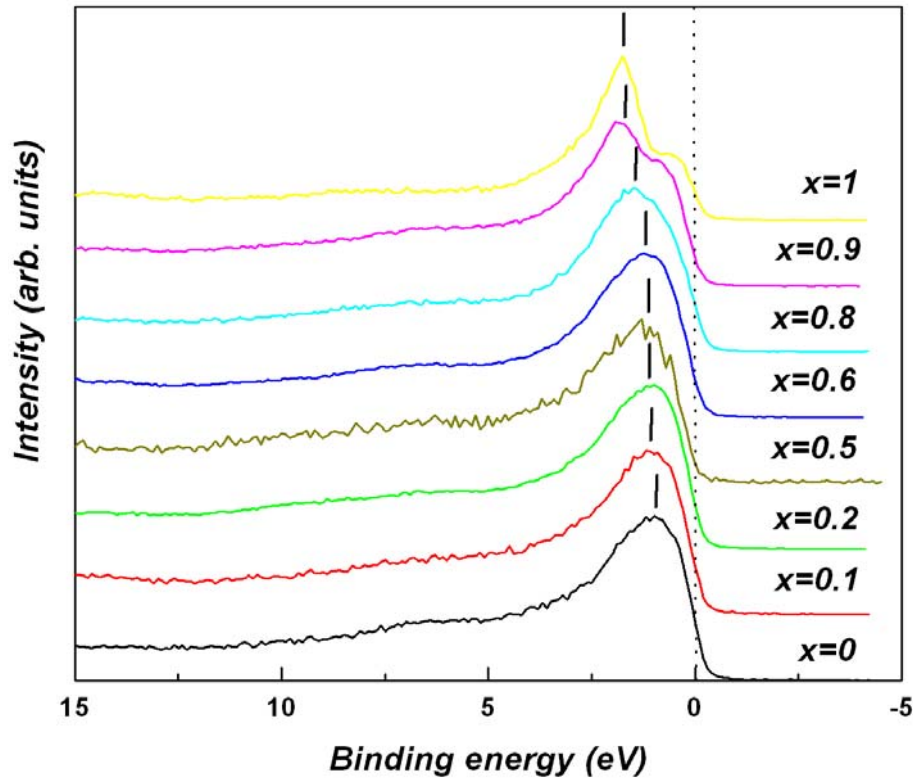
Fig .4.12. XPS valence band spectra of $Mn_{1-x}Al_xNi$ alloys

4.3 Magnetic measurements

Since the Ni atoms do not carry any magnetic moment [121, 133], the interaction Mn-Mn is responsible for the magnetic properties of all investigated alloys.

The alloys $Mn_{1-x}Al_xNi$ for x<0.4 are antiferromagnets with very high Néel temperatures, namely 1073 K for MnNi [116], 1026 K for $Mn_{0.9}Al_{0.1}Ni$ and 820 K for $Mn_{0.8}Al_{0.2}Ni$. For illustration, in Fig. 4.13 is shown the temperature dependence of the measured magnetic susceptibility for $Mn_{0.9}Al_{0.1}Ni$ alloy. The distance between the nearest-neighbor Mn atoms in these alloys, determined from XRD measurements, is about 2.64 Å. It is well known that the Mn-Mn interaction is antiferromagnetic when the distance is smaller than 3 Å [134].

The magnetic field dependence of magnetization at different temperatures for x≥0.5 shows a small curvature (Fig. 4.14), suggesting the presence of a ferromagnetic phase $L2_1$, in which the interaction between the Mn atoms is due to the RKKY coupling [135]. On the other hand, the magnetization does not saturate even at B=10 T, what implies the existence in the alloys of the antifferromagnetic B2 phase.
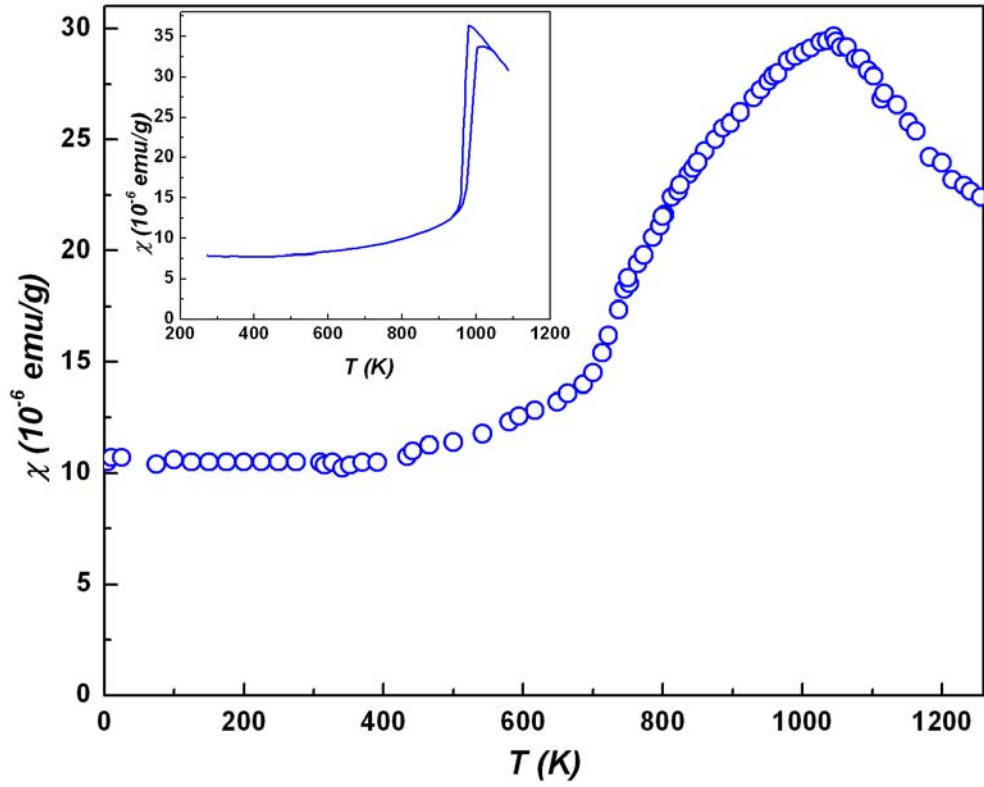
Fig.4.13. Susceptibility versus temperature of $Mn_{0.9}Al_{0.1}Ni$ alloy. In the inset is shown the thermal variation of the susceptibility for MnNi [116].

The alloys $Mn_{1-x}Al_xNi$ for $0.4 < x < 1$ have complex mictomagnetic behavior, with a mixture of antiferromagnetic and ferromagnetic interactions. The coexistence of antiferromagnetism and ferromagnetism in $Mn_{0.5}Al_{0.5}Ni$ alloy was also confirmed in the literature by the susceptibility measurements in field cooled (FC) and zero field cooled (ZFC) [121].
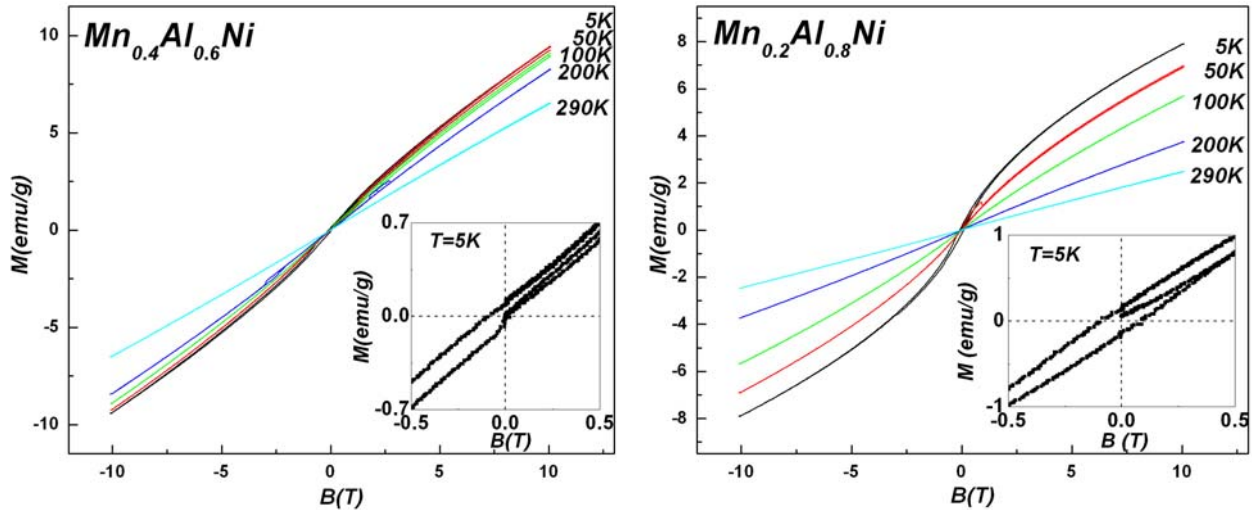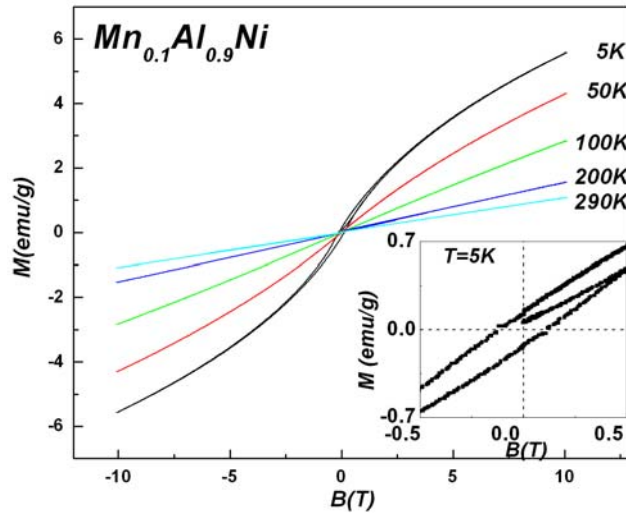
Fig.4.14. Magnetic field dependence of magnetization, at different temperatures, of Mn$_{0.4}$Al$_{0.6}$Ni, Mn$_{0.2}$Al$_{0.8}$Ni and Mn$_{0.1}$Al$_{0.9}$Ni alloys.

The hysteresis loops (see the insets) are shifted to lower negative fields, the effect being more pronounced for x=0.6. The shift in the magnetization of a ferromagnetic component is due to the exchange interaction between the antiferromagnet and ferromagnet at their interface. The ferromagnetic component, which is strongly coupled with the antiferromagnetic one, has its interfacial spins pinned. At lower Mn concentrations, i. e. x = 0.8 and x = 0.9, the amount of antiferromagnetic component decreases (the probability to have Mn-Mn pairs becomes smaller), what explains the almost symmetrical form of the hysteresis loop in this concentration range. The coercive field at T = 5 K increases as Mn concentration decreases, from 0.05 T for x = 0.6 to 0.11 T for x = 0.9. The small values of the coercive field can be explained in the random anisotropy model [136]. The increase of the coercive field as temperature decreases indicates enhancement of the local magnetic anisotropy.

The coexistence of antiferromagnetism and ferromagnetism in Mn$_{1-x}$Al$_x$Ni alloys for 0.6 $\leq$ x < 1 is also revealed by the magnetic measurements in lower magnetic fields. In fig. 4.15 is shown the temperature dependence of FC and ZFC susceptibilities in an applied field of 0.1T. The distinguishing experimental feature of mictomagnetism is that the magnetization drops abruptly at the freezing temperature T$_f$ when the material is cooled in the absence of magnetic field, resulting in a splitting of the FC and ZFC susceptibilities at a certain temperature. The values of this temperature and also the freezing temperature are related to the dilution effect, like in other mictomagnetic systems [137]. The exchange interactions of Mn-Mn type are partially broken when Mn is substituted by Al. The increase of the ZFC susceptibility for x = 0.6 at low temperatures was also observed for x=0.5 [121] and may be due to the conical antiferromagnetic

structure of B2 phase, which has a ferromagnetic component. This conical antiferromagnetic structure was observed in the B2 phase of MnAlNi$_2$ ≡ Mn$_{0.5}$Al$_{0.5}$Ni compound [138].
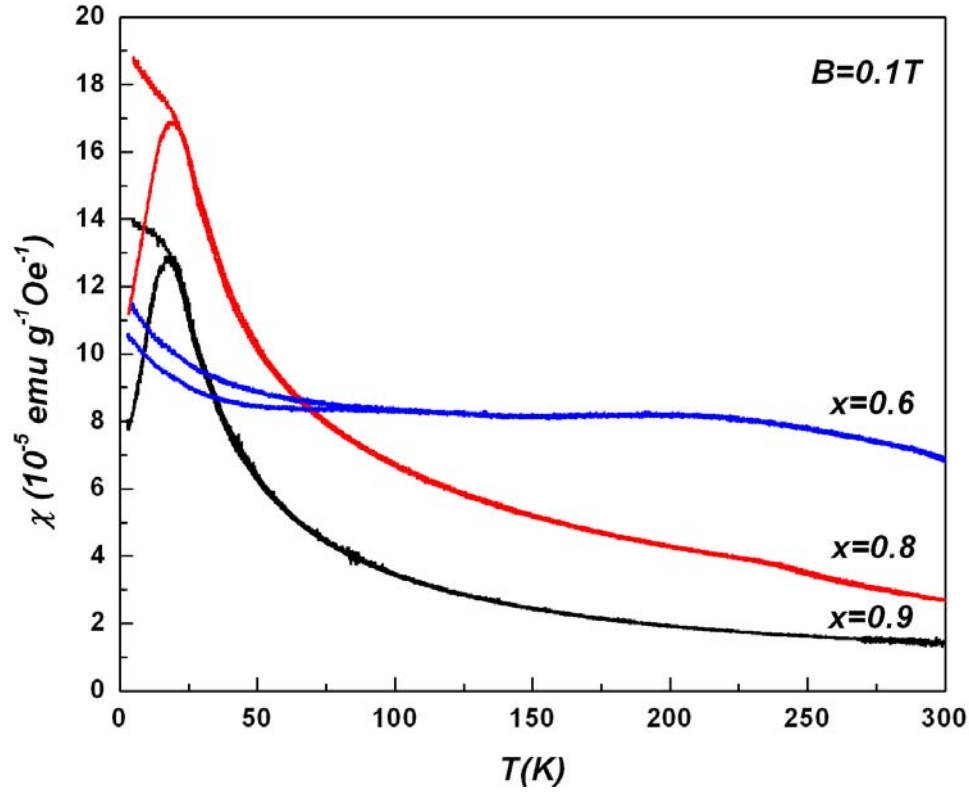
Fig. 4.15. The temperature dependence of the FC and ZFC magnetic susceptibility of Mn$_{1-x}$Al$_x$Ni alloys.

In order to determine the ferromagnetic (FM) and antiferromagnetic contributions to the measured magnetization and to estimate the corresponding Curie and Néel temperatures T$_C$ and respectively T$_N$, we have used the Honda-Arrot plot for each temperature, according to the relation [139]:

$$\chi_m = \chi_{AFM} + M_{FM} / H$$

where χ_m is the measured susceptibility, χ_{AFM} the susceptibility of the antiferromagnetic component, M_{FM} the saturation magnetization of the ferromagnetic component and H the applied magnetic field. A linear dependence of χ_m versus H^{-1} in higher magnetic fields was evidenced for each temperature, showing that in the studied field range, saturation has been obtained. For illustration, in the Fig. 4.16 is shown the dependence χ_m(H^{-1}) for Mn$_{0.4}$Al$_{0.6}$Ni alloy at T = 4 K.

In Figs. 4.17 and 4.18 are shown the temperature dependence of the as determined susceptibility χ_{AFM} and magnetization M_{FM}, respectively. The curves χ_{AFM}(T) present a downward at certain temperatures, referred as the Néel temperatures.
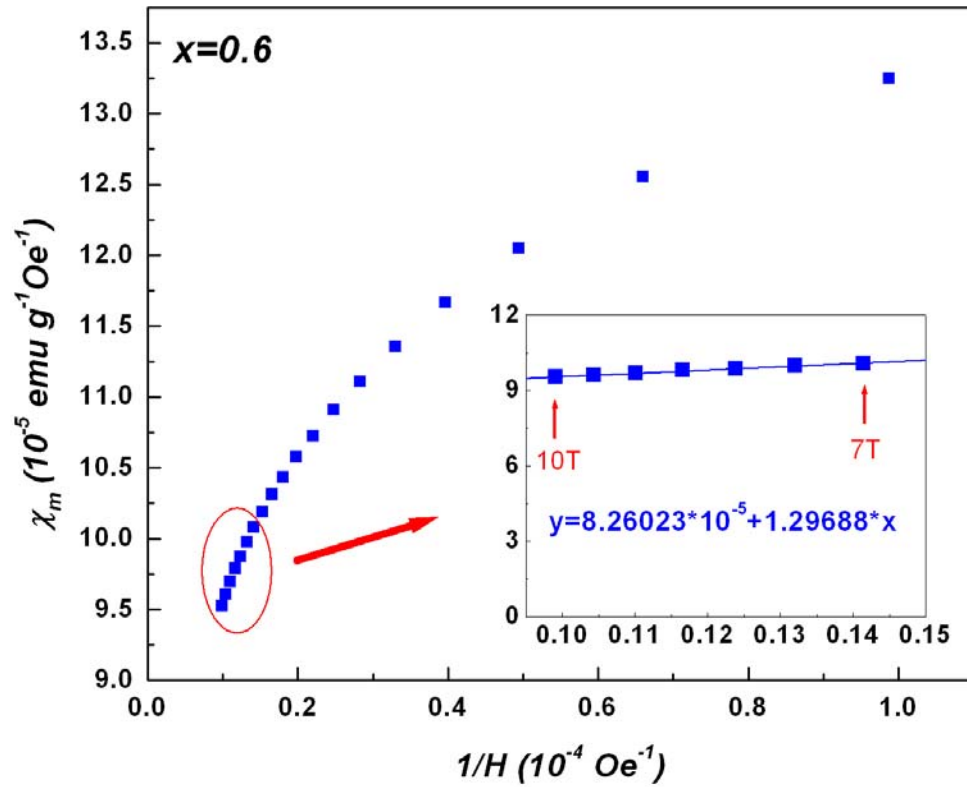
Fig. 4.16. The 1/H dependence of the χ_m for $Mn_{0.4}Al_{0.6}Ni$ alloy at T = 4 K. In the inset is shown the linear dependence at high magnetic fields (7-10) T
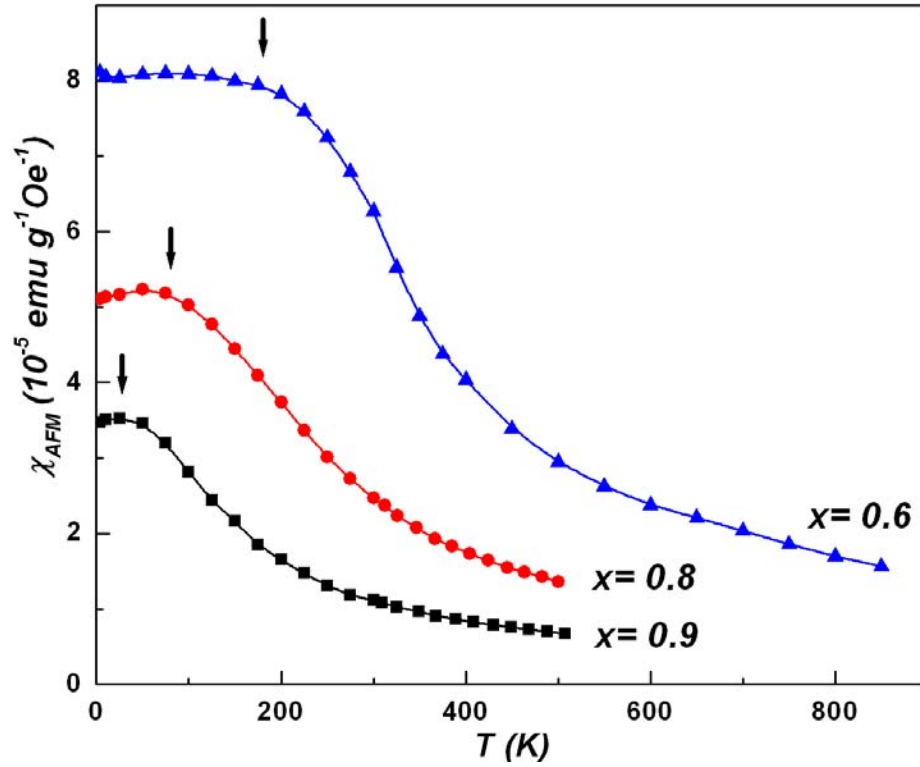
Fig. 4.17. The temperature dependence of the magnetic susceptibility χ_{AFM} of $Mn_{1-x}Al_xNi$ alloys. The arrows indicate the Néel temperatures.
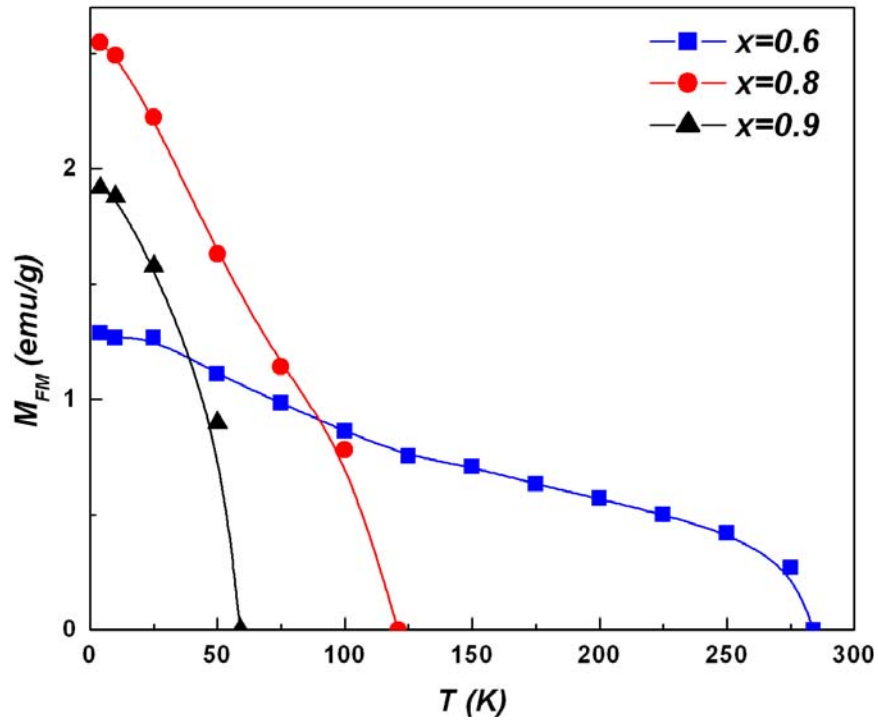
Fig. 4.18. The temperature dependence of the magnetization M_{FM} for $Mn_{1-x}Al_xNi$ alloys.

At about the same temperatures $T \approx T_N$, the curves $M_{FM}(T)$ show a small anomaly in the magnetization of the ferromagnetic component, due to the pinning effect. The Curie temperatures T_C have been determined in the molecular field approximation from the $M_{FM}^2(T)$ dependence. The as determined transition temperatures are given in Table 4.1.
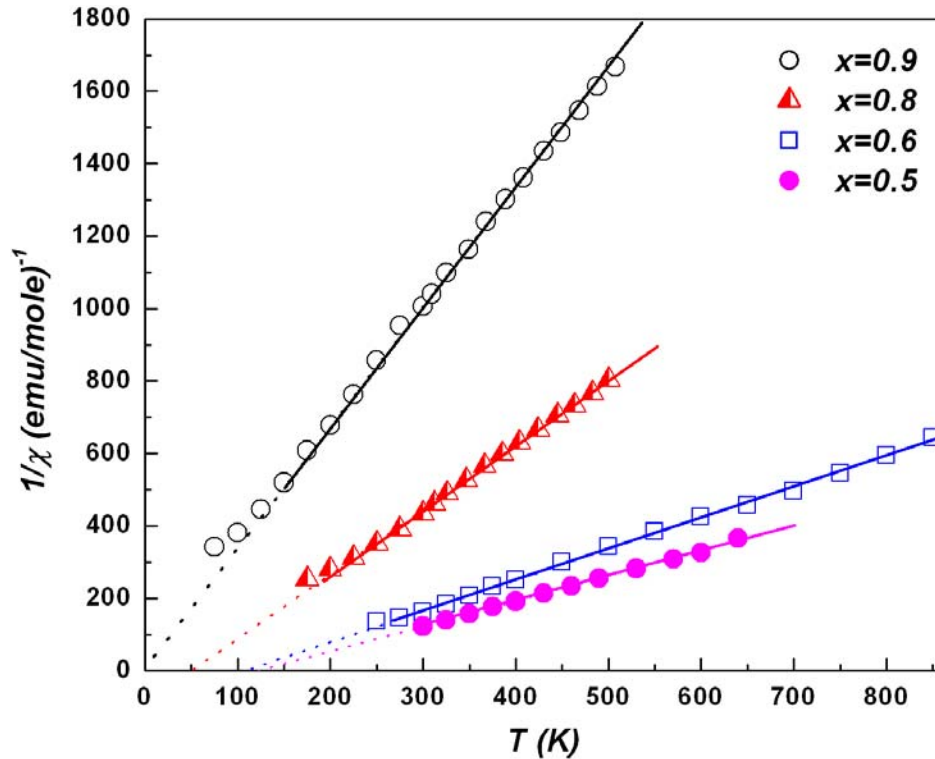
Fig.4.19. Reciprocal susceptibility versus temperature of $Mn_{1-x}Al_xNi$ alloys.

The thermal variation of the reciprocal magnetic susceptibility for the investigated alloys in the high temperature range is shown in Fig. 4.19. The experimental data fit a Curie-Weiss law with a small additional temperature-independent term χ_0, in which the principal contribution is brought by the Pauli susceptibility χ_P of the conduction electrons:

$$\chi=C/(T-\theta) + \chi_0$$

The values of the effective magnetic moments μ_{eff} and of the paramagnetic Curie temperatures θ are given in Table 4.1. The Ni 3d band for $x \geq 0.5$ is almost filed. This assumption is confirmed by the very small intensity of the Ni 2p and valence band satellite. The contribution of the Ni atoms to the total effective magnetic moment is negligible, so the measured effective magnetic moment may be attributed only to the Mn atoms. The effective magnetic moments per Mn atom have approximately the same value, corresponding to a spin $S \cong 2$, like in the parent compound MnNi, showing that the Mn 3d band is not affected by alloying, suggesting that the hybridization between the Mn 3d states and the Al 3sp states is very small. The paramagnetic Curie temperatures θ are much lower than the Curie temperatures T_C. This is due to the contribution of antiferromagnetic part in the measured magnetic susceptibility, which has a negative θ value, and consequently an averaged paramagnetic Curie temperature is observed. The relative proportion of the ferromagnetic and antiferromagnetic parts in the samples is also reflected in the difference between the Curie temperatures T_C and paramagnetic Curie temperatures θ as a function of the Al content. This difference decreases with Al concentration, confirming the decrease of the antiferromagnetic component at lower Mn concentrations.

Table. 4.1. Transition temperatures and effective magnetic moments of $Mn_{1-x}Al_xNi$ alloys

x	T_N (K)	T_C (K)	θ (K)	$\mu_{eff}(\mu_B/f.u.)$	$\mu_{eff}(\mu_B/Mn)$
0.5	313*	375*	123	3.44	4.87
0.6	181	284	108	3.07	4.85
0.8	80	121	50	2.21	4.94
0.9	26	59	-3	1.55	4.90

*data taken from [121]

4.4 Conclusions

- The substitution of Al for Mn in MnNi leads to significant changes in the crystallographic structure with remarkable effects on the magnetic properties and electronic structure of $Mn_{1-x}Al_xNi$ alloys.

- XPS spectra and magnetic measurements pointed out the existence of local magnetic moments on Mn sites in all $Mn_{1-x}Al_xNi$ alloys.

- The investigated alloys are antifferomagnets, but for $x \geq 0.5$ the antiferromagnetism (B2) and ferromagnetism ($L2_1$) coexist.

- The exchange interaction between the antifferomagnetic and ferromagnetic entities at their interfaces leads to different configurational "pinning" of ferromagnetic components.

- The transition temperatures decrease as Al concentration increases.

- The hybridization between Ni 3d and Al 3sp states leads to a gradual filling of the Ni 3d band.

- The Mn 3d band in $Mn_{1-x}Al_xNi$ system is not affected by alloying.

Electronic structure and magnetic properties
of $Ni_{1-x}Mn_xAl$ alloys [140-142]

In the previous two chapters it was studied the influence of the substitution of Mn by Al in the ternary system Al-Mn-Ni, on the electronic, crystallographic and magnetic structure, keeping the Ni atomic concentration constant. In the present chapter the Al atomic concentration will remain the same and we will focus on the effect of the substitution of Ni by Mn.

The phase diagram (Fig. 5.1) indicates, in case of $Ni_{1-x}Mn_xAl$ system, a large region of solid solubility, excepting for the high Mn concentrations. There are no reports about bulk AlMn in a stable phase, but only on $Al_{0.89}Mn_{1.11}$ [143]. In the other side of the concentration range is AlNi, a Pauli paramagnet.
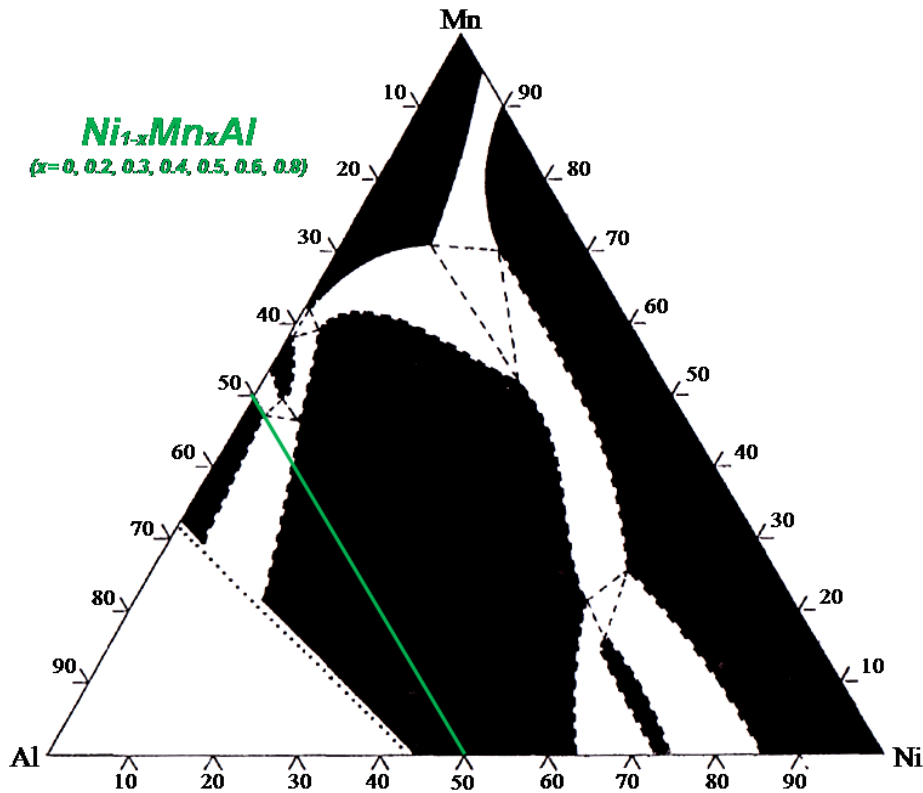
Fig. 5.1. Thernary phase diagram of Ni-Mn-Al alloys at T=1273K

Magnetic properties of the $Ni_{1-x}Mn_xAl$ alloys were reported in literature [144], but there are no explanation regarding the relative small values of the measured magnetic moments per atom, their variation with Ni atoms concentration and if Ni brings or not a contribution in the measured magnetic moments.

The aim of this chapter is to explain the magnetic properties of the investigated alloys by correlating the magnetic measurements, in the ordered and paramagnetic state, with XRD and XPS results.

5.1 Structural characterization

Seven samples from the $Ni_{1-x}Mn_xAl$ system (x=0.0, 0.2, 0.3, 0.4, 0.5, 0.6, 0.8) were prepared. XRD measurements were performed on polished surfaces due to the hardness of the samples. The broad character of the peaks indicates the presence of the strains in the samples. X-ray diffraction pattern of $Ni_{1-x}Mn_xAl$ alloys are shown in Fig. 5.2.
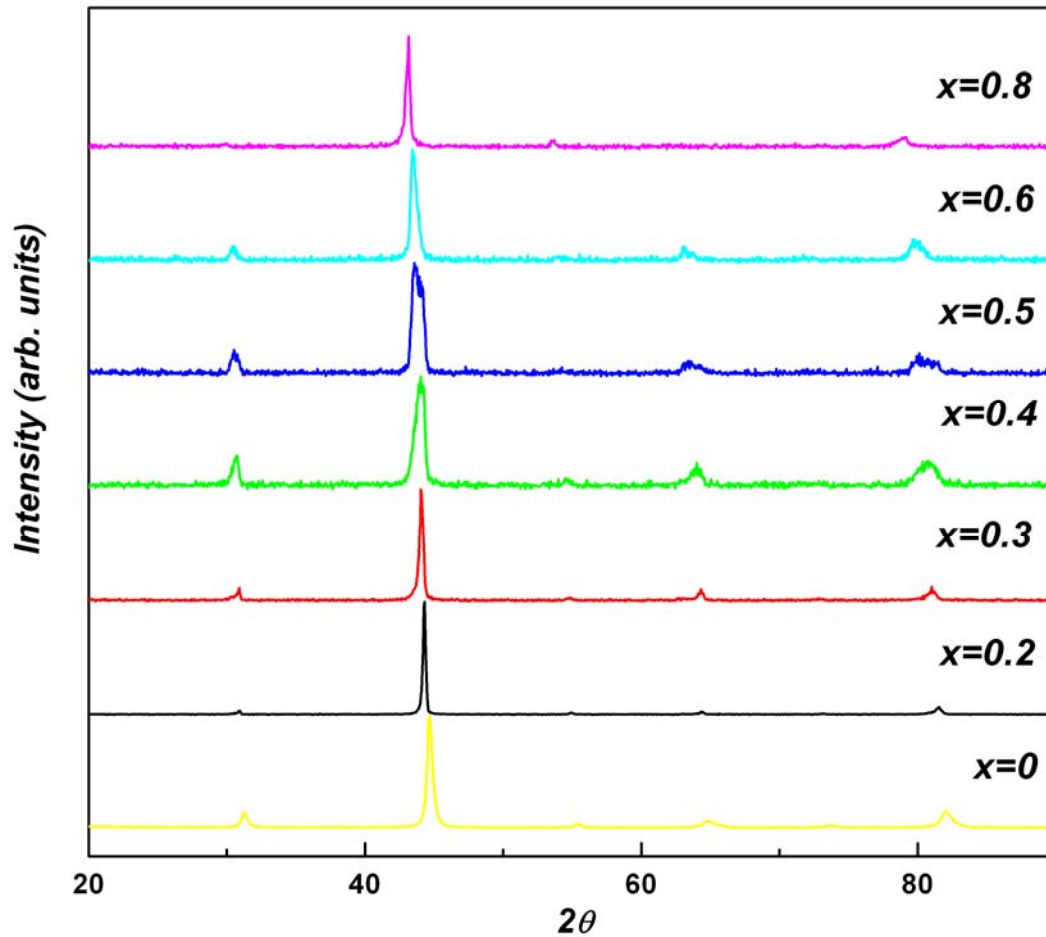
Fig. 5.2. X-ray diffraction pattern of $Ni_{1-x}Mn_xAl$ alloys.

All the investigated alloys are single phases with the same CsCl (B2) structure type (Fig. 5.3a). The lattice parameter, estimated using the Powder Cell program, increases monotonically with Mn concentration from a=2.875 Å for NiAl to a=2.966 Å for $Ni_{0.2}Mn_{0.8}Al$ (Fig. 5.3b).
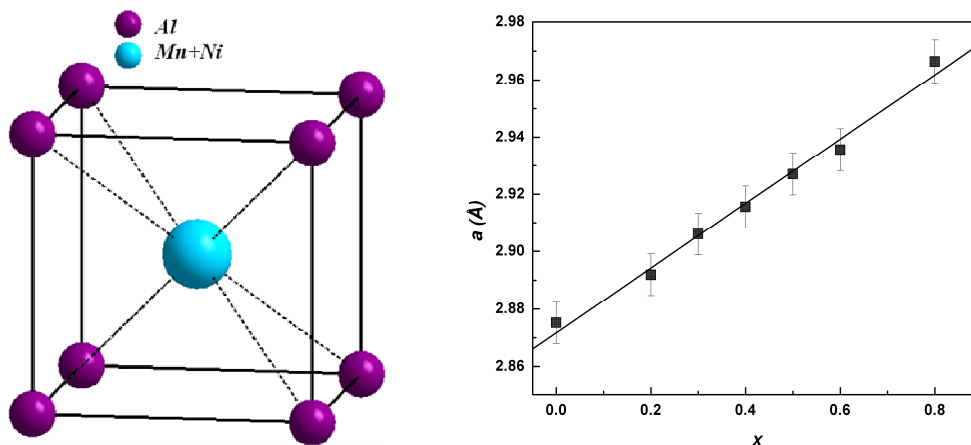
Fig.5.3. Elementary cell of Ni$_{1-x}$Mn$_x$Al alloys (a) and the variation of the lattice parameter with Mn content (b)

5.2 XPS Spectra

The XPS valence band spectra of investigated alloys are shown in Fig. 5.4. The maximum of the Ni 3d band is shifted to a BE of 1.8 eV comparing to the value of 0.6 eV in pure metallic Ni [122]. The shoulder near Fermi level is due to the Al 3sp states. Another contribution to the XPS valence band spectra of Ni$_{1-x}$Mn$_x$Al alloys comes from Mn 3d states, which are concentrated at the bottom of the VB in the 2.5-3eV BE region, as previously demonstrated by band structure calculation and experimental measurements for many alloys and intermetallic compounds based on Mn [109-111]. There is also an appreciable hybridization between the Mn 3d and Al 3sp states which leads, according Mn 3s XPS spectra and magnetic measurements, to a partial filling of the Mn 3d band.
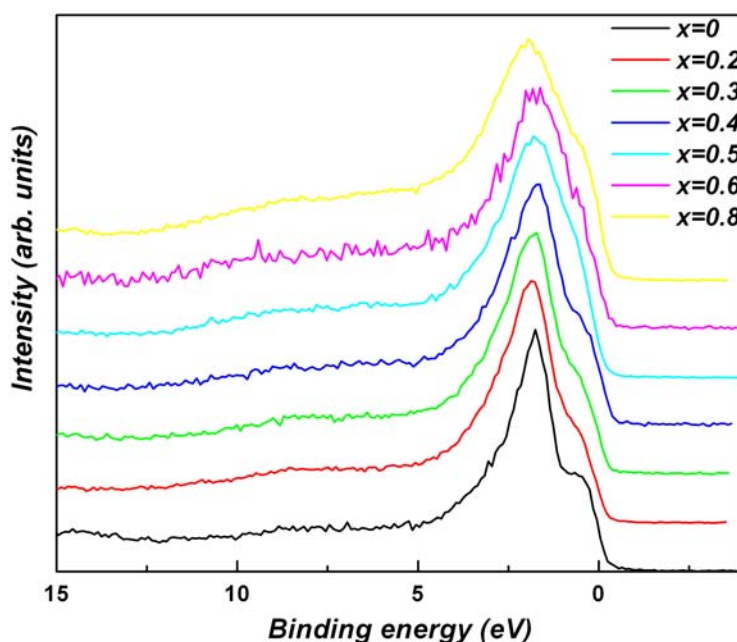
Fig .5.4. XPS valence band spectra of Ni$_{1-x}$Mn$_x$Al alloys

The Ni 2p spectra for all investigated alloys are situated at the same BE, but are shifted to higher BE relative to pure metallic Ni. This also confirms the partial filling of Ni 3d band. The first vicinity of Ni atoms in the $Ni_{1-x}Mn_xAl$ alloys does not change by alloying, what explains the lack of the chemical shift in the Ni 2p spectra.
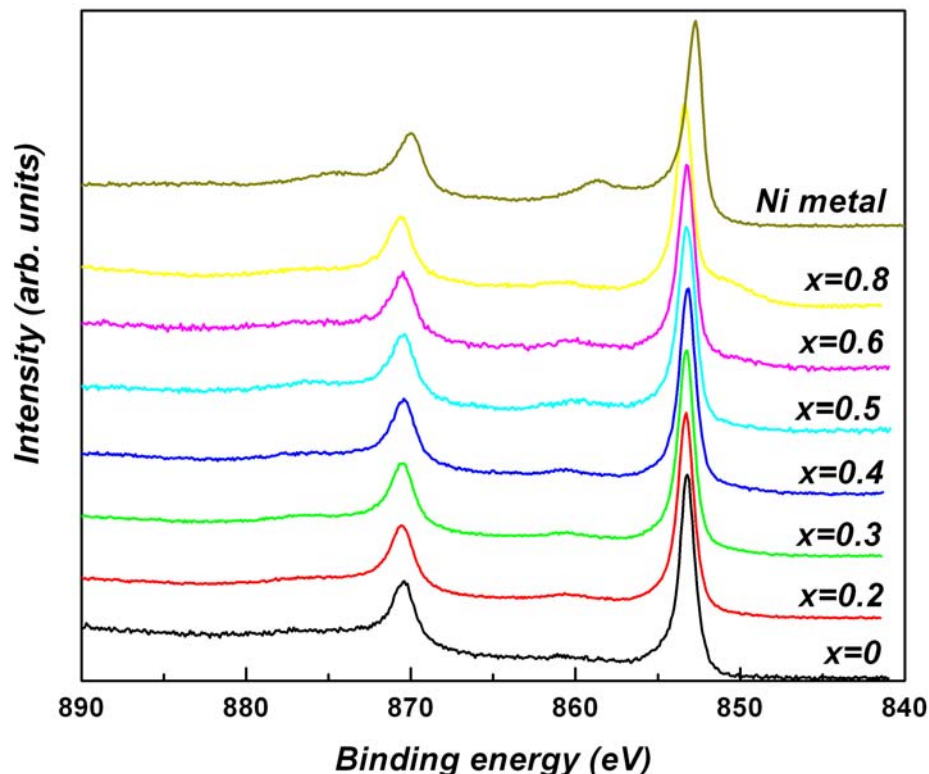
Fig .5.5. Ni 2p XPS spectra of $Ni_{1-x}Mn_xAl$ alloys and pure metallic Ni

In Ni metal the Ni 2p satellite structure, situated at about 6.5 eV higher BE energy, is an evidence for unoccupied 3d states. The intensity of the satellites in $Ni_{1-x}Mn_xAl$ alloys is drastically reduced (see Fig. 5.5) confirming the partial filling of the Ni 3d band of the investigated alloys, except for x=0 where the satellite structure disappears. This confirms the previous magnetic measurements that have shown that NiAl is a Pauli paramagnet with Ni 3d band completely filled, at room temperature, due to the hybridization with Al 3sp states.

The Mn 3s core level spectra show an exchange splitting around 4 eV arising from the exchange interactions between the core hole and the open 3d shell. The exchange splitting in MnNi is about 5.2 eV and the Mn magnetic moment is about 4 μ_B/Mn [116]. The exchange splitting is proportional with the Mn local moment [122]. Fig. 5.6 presents the curve fitting results of $Mn_{0.8}Ni_{0.2}Al$ alloy, after background subtraction, and the similar spectrum of MnNi compound.
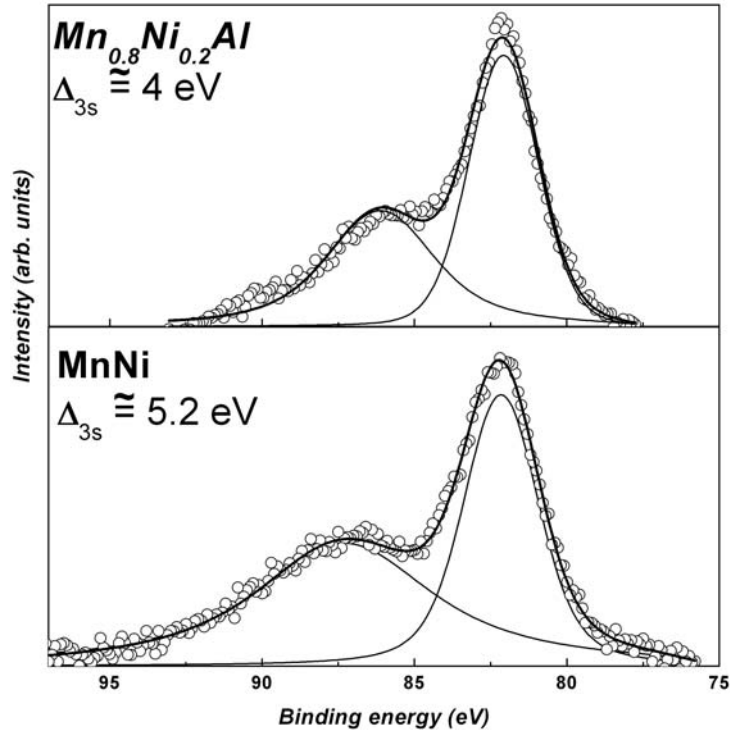
Fig. 5.6. Mn 3s curve fitting results of Mn$_{0.8}$Ni$_{0.2}$Al alloy and MnNi compound

5.3 Magnetic measurements

The values of the spontaneous magnetization, for each temperature, were determined from M(H) curves by extrapolation the linear dependence at H→0. The temperature dependence of the spontaneous magnetization of Ni$_{1-x}$Mn$_x$Al alloys is shown in Fig. 5.7.
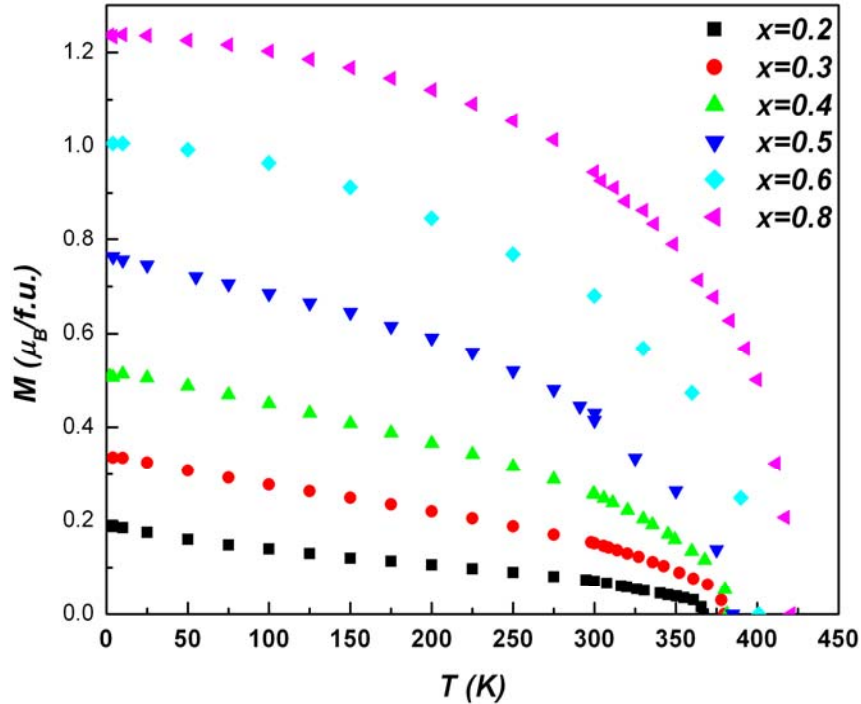
Fig. 5.7. Temperature dependence of spontaneous magnetization of Ni$_{1-x}$Mn$_x$Al alloys

The values and variations of magnetization with magnetic field (Fig. 5.8) and temperature suggest that all the investigated alloys have a ferromagnetic behavior, below the corresponding Curie temperatures.
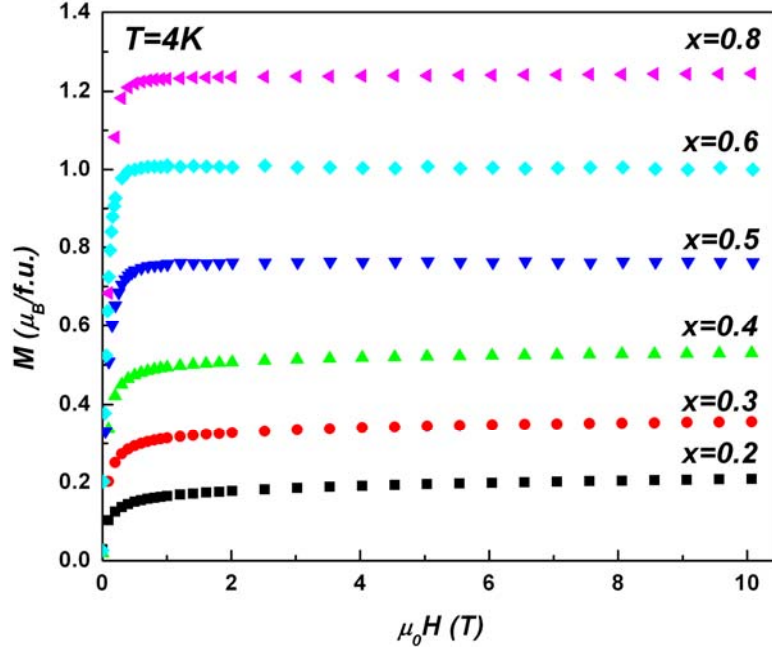
Fig. 5.8. Magnetic field dependence of magnetization at T=4K of Ni$_{1-x}$Mn$_x$Al alloys.

The Curie temperatures T$_C$ have been determined in the molecular field approximation from the M$_{FM}^2$(T) dependence (Fig. 5.9). The values are given in Table 5.1.
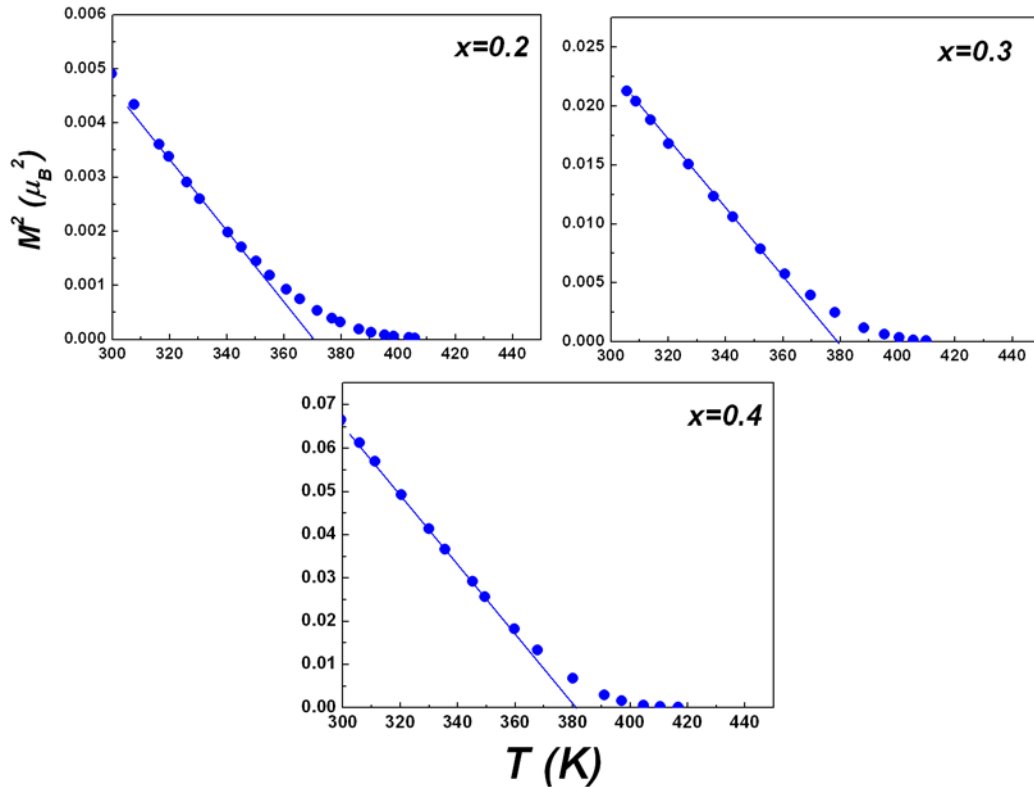
Fig. 5.9. M$_{FM}^2$ as a function of temperature of Ni$_{1-x}$Mn$_x$Al alloys

The thermal variation of the reciprocal magnetic susceptibility for the investigated alloys in the high temperature range is shown in Fig. 5.10. The experimental data fit a Curie-Weiss law with a small additional temperature-independent term χ_0, in which the principal contribution is brought by the Pauli susceptibility χ_P of the conduction electrons:

$$\chi = C/(T-\theta) + \chi_0$$

The values of the effective magnetic moments μ_{eff} and of the paramagnetic Curie temperatures θ are given in Table 5.1. As one can see from Fig. 5.10, the contribution of χ_0 is more pronounced in the measured magnetic susceptibility for smaller Mn concentrations.
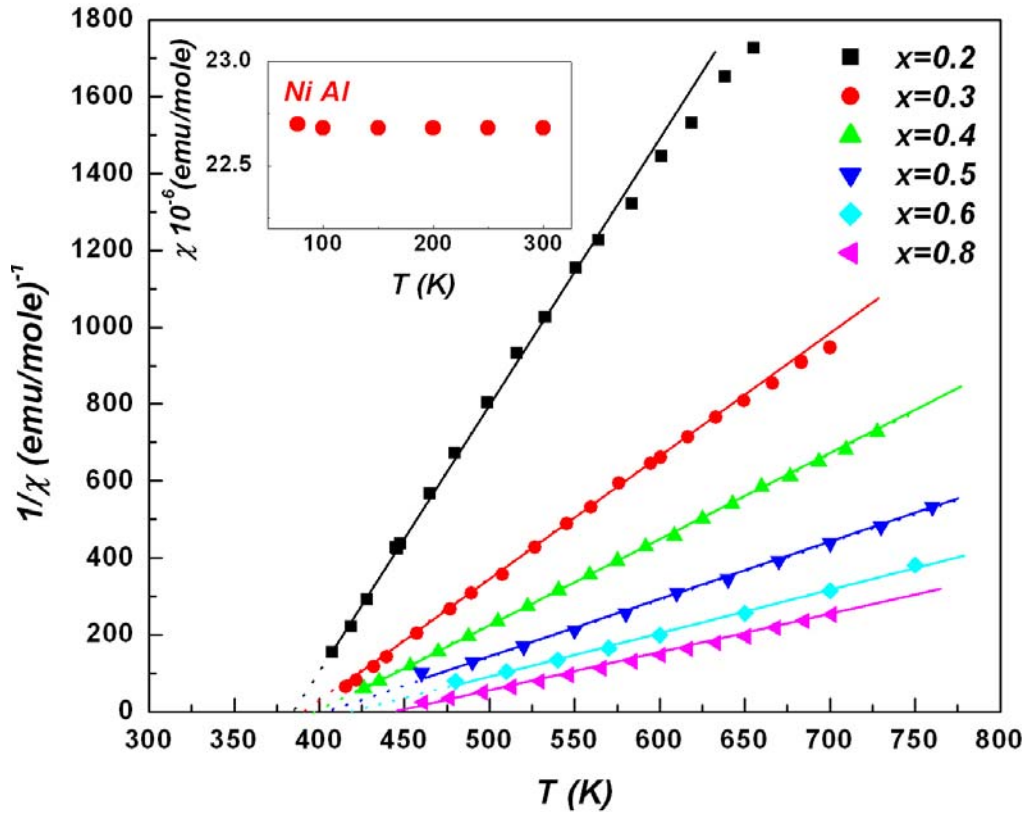
Fig.5.10. Reciprocal susceptibility versus temperature of $Ni_{1-x}Mn_xAl$ alloys. In the inset is given the temperature dependence of magnetic susceptibility of NiAl [145]

The magnetic susceptibility of NiAl does not depend on temperature in the region 80-100K and has the value: $\chi_{NiAl}^{meas} = 0.265 \times 10^{-6}\, emu/g$ [145]. There are three contributions to the total measured susceptibility: $\chi_{NiAl}^{meas} = \chi_p^{meas} + \chi_L + \chi_{dia}$, where χ_p^{meas} is the measured Pauli susceptibility of conduction electrons, χ_L the Landau diamagnetism of the conduction electrons and χ_{dia} the diamagnetism of the atomic cores. The Pauli susceptibility in the free electrons

approximation is given by: $\chi_p^0 = 1.86 \times 10^{-6} \left(\dfrac{M}{\rho} \right)^{2/3} n^{1/3} = 0.3 \times 10^{-6}$ emu/g, where M is the

molecular mass, ρ the density and n the number of s, p and d valence electrons per unit

formula. The Landau diamagnetism is $\chi_L = -\dfrac{1}{3} \chi_p^0 = -0.1 \times 10^{-6}$ emu/g. The diamagnetic

contribution to the magnetic susceptibility is $\chi_{dia} = \chi_{dia}^{Al} + \chi_{dia}^{Ni} = -0.18 \times 10^{-6}$ emu/g [145]. The

measured Pauli susceptibility is $\chi_p^{meas} = \chi_{NiAl}^{meas} - \chi_L - \chi_{dia} = 0.545 \times 10^{-6}$ emu/g. The ratio

$\delta = \dfrac{\chi_p^{meas}}{\chi_p^0}$ between the between the Pauli susceptibilities of d electrons measured and calculated

in the free electron approximation is the Stoner enhancement factor which for NiAl has the value

$\delta = 1.8$. This value shows that NiAl is exchange-enhanced Pauli paramagnet, suggesting that

also the $Ni_{1-x}Mn_xAl$ alloys could be exchange-enhanced Pauli paramagnets, which are correctly

treaded in the self-consistent renormalization (SCR) theory of spin fluctuations [34].

Table 5.1. The magnetic moments in the ordered (μ) and paramagnetic state (μ_{eff}), the Curie (T_C) and paramagnetic Curie (θ) temperatures and the lattice constants (a) of the $Ni_{1-x}Mn_xAl$ alloys.

	μ (μ_B/f.u.)	μ_{eff} (μ_B/f.u.)	T_C (K)	θ (K)	a (Å)
x=0					2.8752
x=0.2	0.19	1.06	367	385.7	2.8919
x=0.3	0.34	1.57	379.8	395	2.906
x=0.4	0.51	1.9	381.5	398.8	2.9155
x=0.5	0.77	2.32	385	405.5	2.927
x=0.6	1.01	2.66	401	422.7	2.9356
x=0.8	1.24	2.9	420.8	445.9	2.9664

T_C and θ increase monotonically with Mn concentration in good agreement with the theory of ferromagnetic materials, T_C being proportional with the number Z of neighboring magnetic atoms [146]. Comparing the intensity of the Ni 2p and valence band satellites in this systems with the similar ones in the previous system $Mn_{1-x}Al_xNi$, one may conclude that also in $Ni_{1-x}Mn_xAl$ alloys the Anderson condition of the existance of a local moment on Ni sites in the ordered state is not fulfilled. So, the measured magnetic moments in the ordered state are attributed to Mn atoms only. The values of the Mn spins S_{Mn} (see Table 5.2) were obtained from the relation $\mu_{Mn} = 2 S_{Mn}\mu_B$. Using these values, the effective Mn magnetic moments are calculated

$(\mu_{eff}^{Mn} = 2\sqrt{S_{Mn}(S_{Mn}+1)}\mu_B)$. In the paramagnetic region we have to consider the contribution of Ni magnetic moments, induced by temperature, to the magnetic susceptibility (the Ni 3d band is not completely filled). In the last column the Ni contribution to the effective magnetic moment is calculated ($\mu_{f.u.}^2 = x\mu_{Mn}^2 + y\mu_{Ni}^2$, x and y are the molar fraction of Mn and Ni, respectively). The Ni effective magnetic moment has reasonable values for x≤0.4, comparable with the values on Ni sites in other spin fluctuation systems [147, 148]. For x>0.4 the calculated Ni effective magnetic moments are too large; this suggests that not all the Mn atoms moments are orientated in the same direction and is possible to have antiferromagnetic Mn-Mn pairs. The probability of the apparition of Mn-Mn antiferromagnetic pairs increases with Mn concentrations.

Table 5.2. The magnetic moments and spin of Mn atoms in the ordered state and the calculated Mn and Ni effective magnetic moments of the $Ni_{1-x}Mn_xAl$ alloys.

	μ_{ord}^{Mn}	S_{Mn}	μ_{eff}^{Mn}
x=0.2	0.95	0.48	1.69
x=0.3	1.13	0.57	1.89
x=0.4	1.28	0.64	2.05
x=0.5	1.54	0.77	2.33
x=0.6	1.68	0.84	2.49
x=0.8	1.55	0.78	2.36

The strong Mn 3d - Al 3sp hybridization is due to the high number of Al atoms in the Mn first vicinity, namely 8 Al atoms at ~2.5 Å. This explains the small values of the Mn magnetic moments in $Ni_{1-x}Mn_xAl$ alloys comparing to MnNi. The Mn magnetic moment in the ordered state increases with Mn concentration, except for the x=0.8 alloy. This variation can be associated with the increase of the lattice parameter which leads to a decreasing in the Mn 3d - Al 3sp hybridization degree. But together with the Mn concentration, increases also the probability of the Mn-Mn antiferromagnetic pairs formation, so that a number of Mn magnetic moments do not contribute to the magnetization. These two phenomena influence the value of the measured magnetic moments.

It is well known that Mn-Mn interaction is antiferromagnetic when the distance is smaller than ~2.9 Å [29], comparable with the lattice constant in $Ni_{1-x}Mn_xAl$ alloys. For larger values the coupling is ferromagnetic. In these alloys there are two possibilities for the appearance of antiferromagnetic Mn-Mn pairs:

- There are two Mn atoms in the centre of near neighbour cells and lattice parameter is smaller than 2.9 Å (Fig. 5.11 a);

- A crystallographic disorder appears: Mn and Al atoms switch places, thus the Mn-Mn distance became ~2.5 Å (Fig. 5.11 b). The problem of crystallographically disorder alloys was fully discussed in chapter 3.
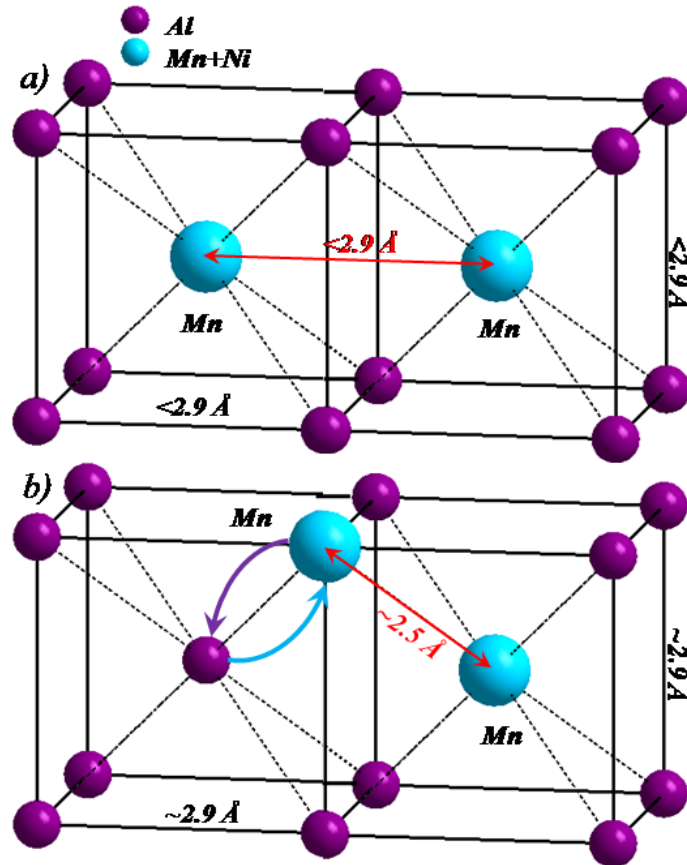
Fig. 5.11. Possible situations for Mn-Mn distance smaller than 2.9 Å

5.4 Conclusions

➢ The substitution of Ni for Mn in NiAl leads to no significant changes in the crystallographic structure, but has remarkable effects on the magnetic properties and electronic structure of $Ni_{1-x}Mn_xAl$ alloys.

➢ $Ni_{1-x}Mn_xAl$ alloys present a ferromagnetic behaviour below the corresponding Curie temperatures.

➢ The correlation between the results from ordered and paramagnetic state indicates the presence of some antiferromagnetically Mn-Mn pairs.

- ➢ The temperature dependence of the reciprocal susceptibility may be explained in terms of the self-consistent renormalization theory of spin fluctuations.

- ➢ Ni 3d band is partially filled due to the hybridization with Al 3sp states.

- ➢ The strong hybridization between Mn 3d and Al 3sp states is responsible for the lower values of the Mn magnetic moments.

Chapter 6

Electronic structure and magnetic properties of $Ni_{0.7-x}Al_xMn_{0.3}$ alloys [149]

In the last three chapters it was presented the effect of the substitution of Mn by Al atoms and Ni by Mn atoms in the electronic, crystallographic and magnetic structure, keeping the Ni and respective Al atomic concentration constant. To have a complete picture of the Al-Mn-Ni system in this chapter the Mn atomic concentration will remain the same and the substitution effect of Ni by Al atoms will be studied.

The phase diagram (Fig. 6.1) indicates, in case of $Ni_{0.7-x}Al_xMn_{0.3}$ alloys, two main regions of solid solubility. There are no reports in the literature regarding the structure, magnetic and spectroscopic properties of $Ni_{0.7-x}Al_xMn_{0.3}$ system.
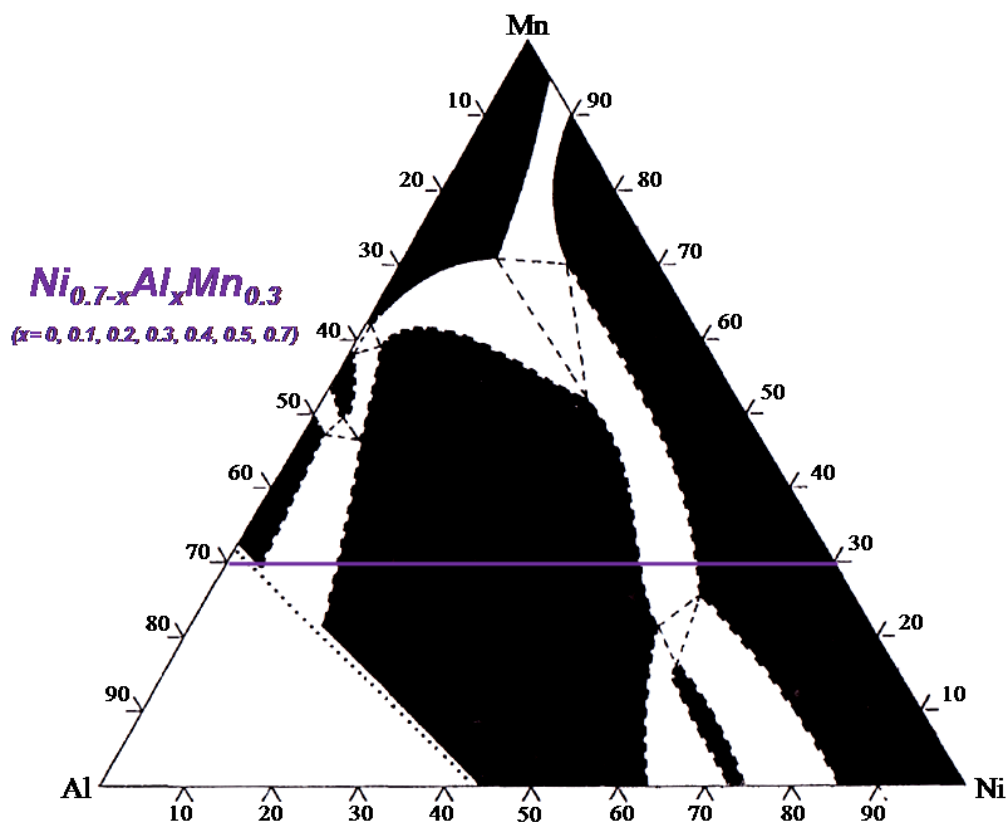
Fig. 6.1. Thernary phase diagram of Ni-Mn-Al alloys at T=1273K

6.1 Structural characterization

Seven samples from the $Ni_{0.7-x}Al_xMn_{0.3}$ system (x=0.0, 0.1, 0.2, 0.3, 0.4, 0.5, 0.7) were prepared. XRD measurements were performed on polished surfaces due to the hardness of the samples. X-ray diffraction pattern of $Ni_{0.7-x}Al_xMn_{0.3}$ alloys are shown in Fig. 6.2. The broad character of the peaks indicates the presence of the strains in the samples.
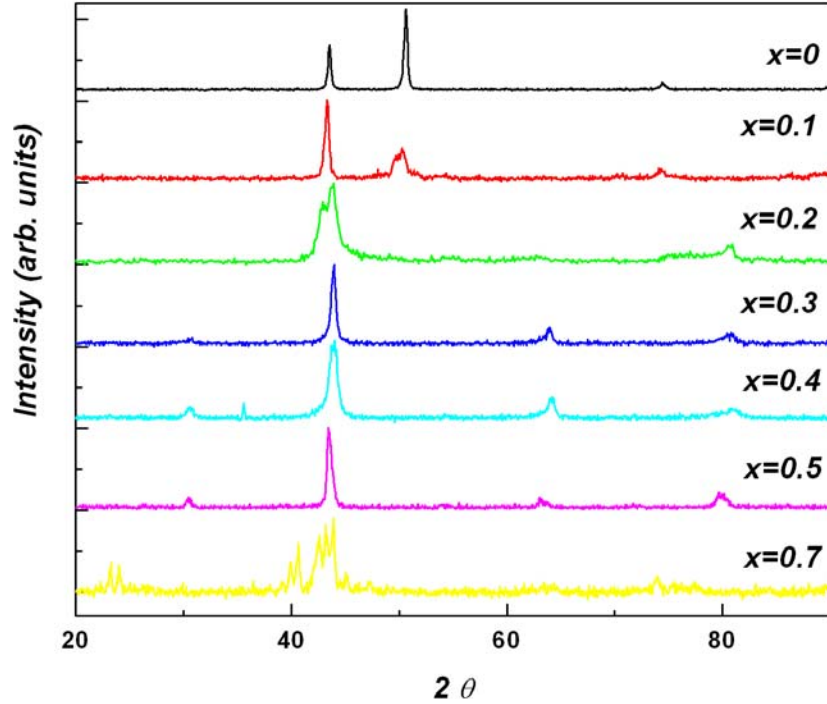
Fig. 6.2. X-ray diffraction pattern of $Ni_{0.7-x}Al_xMn_{0.3}$ alloys

All the investigated alloys are single phases except for $Al_{0.7}Mn_{0.3}$ and $Ni_{0.5}Al_{0.2}Mn_{0.3}$ alloys. XRD measurements revealed a change in the crystallographic structure around x = 0.2 from $AuCu_3$ to CsCl (B2) structure type. $Ni_{0.5}Al_{0.2}Mn_{0.3}$ appears as a mixture of these two structures. The results only from the single phase alloys are presented in the following pages.
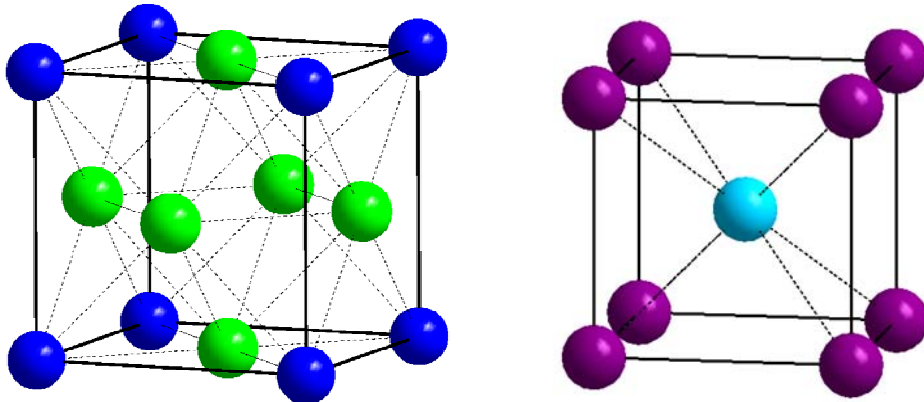
Fig.6.3.Representation of $AuCu_3$ and ClCs structure type

6.2 XPS spectra

XPS valence band spectra of the $Ni_{0.7-x}Al_xMn_{0.3}$ alloys are shown in Fig. 6.4. For Al K_α radiation, the Ni 3d cross section is about four times larger than the Mn 3d cross section [108]. Taking also into account the ratio between the contents of Ni and Mn in the alloys, one can say that the valence-bands spectra of $Ni_{0.7-x}Al_xMn_{0.3}$ alloys, at high Ni concentrations, are dominated by the Ni 3d states, which are preponderant at the Fermi level as in metallic Ni.
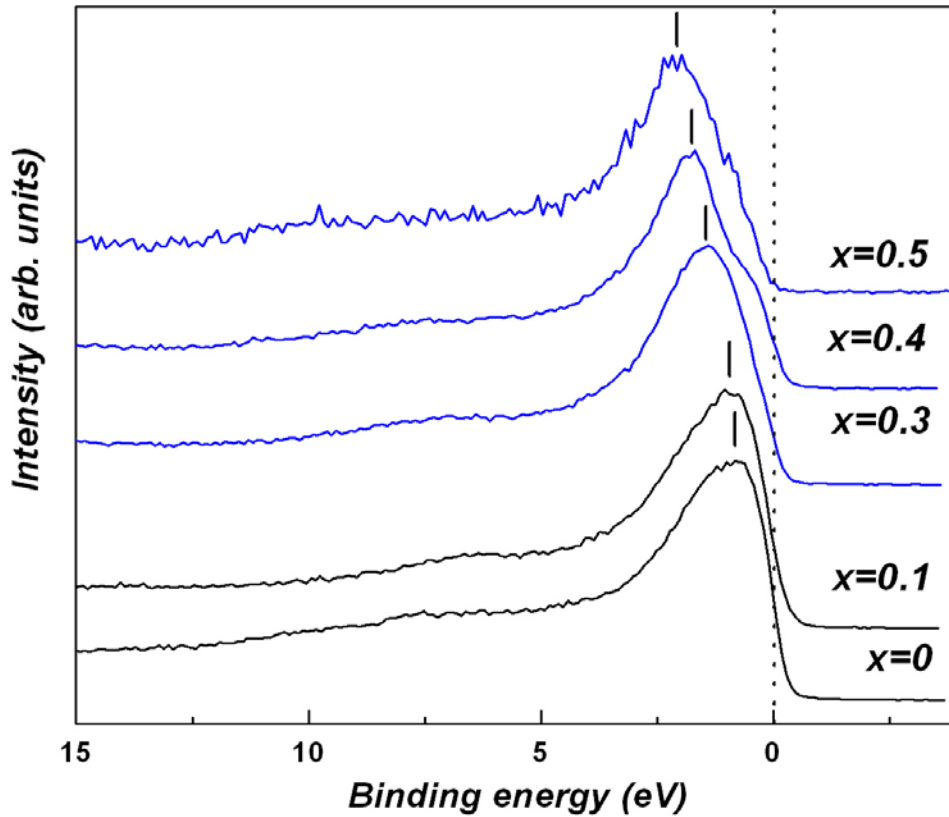
Fig. 6.4. XPS valence band spectra of $Ni_{0.7-x}Al_xMn_{0.3}$ alloys. The dotted line and the bars indicate the Fermi level and the position of the valence band centroids

The Mn 3d states are concentrated at the bottom of the valence band in the region around 3 eV binding energy and became more visible at low Ni concentrations. The XPS valance band spectra for small x present satellite structures at about 6.5 eV, which gradually disappears with the increase of Al content. The valence band centroids are shifted towards higher binding energies and the density of states at Fermi level decreases as the Al concentration increases, suggesting a gradual filling of the Ni 3d band due to hybridization of the Al 3sp and Ni 3d states. In d-band metals and alloys the 3d states are shifted gradually to higher binding energy with the increase in the d-state occupancy and consequently a decrease in the density of states at the Fermi level occurs.

The Ni 2p core-level spectra of $Ni_{0.7-x}Al_xMn_{0.3}$ alloys are shown in Fig. 6.5. The Ni $2p_{3/2}$ core level spectra exhibit satellite structures at about 6.5 eV higher binding energy (Fig. 6.6).
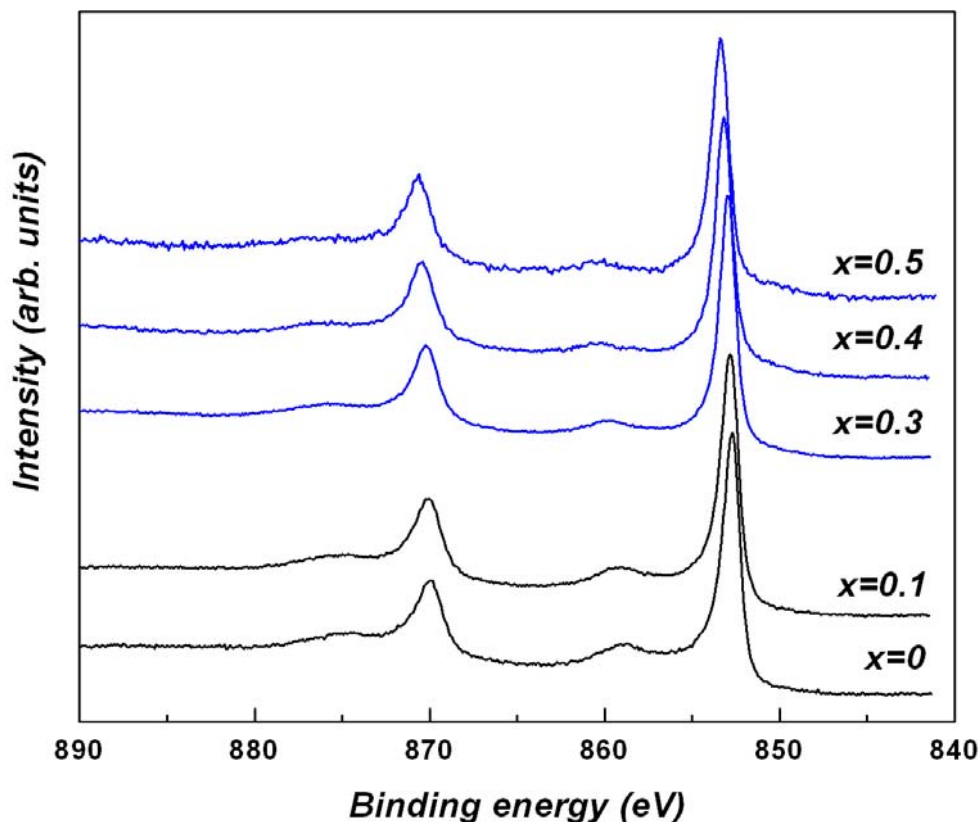
Fig .6.5. Ni 2p XPS spectra of $Ni_{0.7-x}Al_xMn_{0.3}$ alloys

As the Al concentration increases, the Ni 2p core-level lines are shifted to higher binding energy. These small chemical shifts are due to the change in the filling degree of the Ni 3d band, which leads to an increase in the electronic density around the Ni 2p shell.
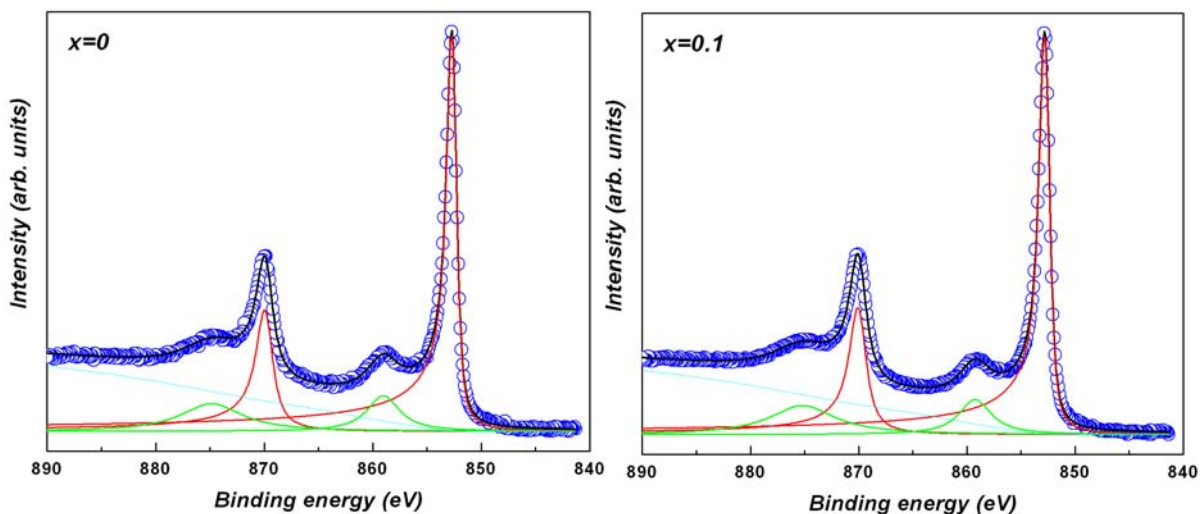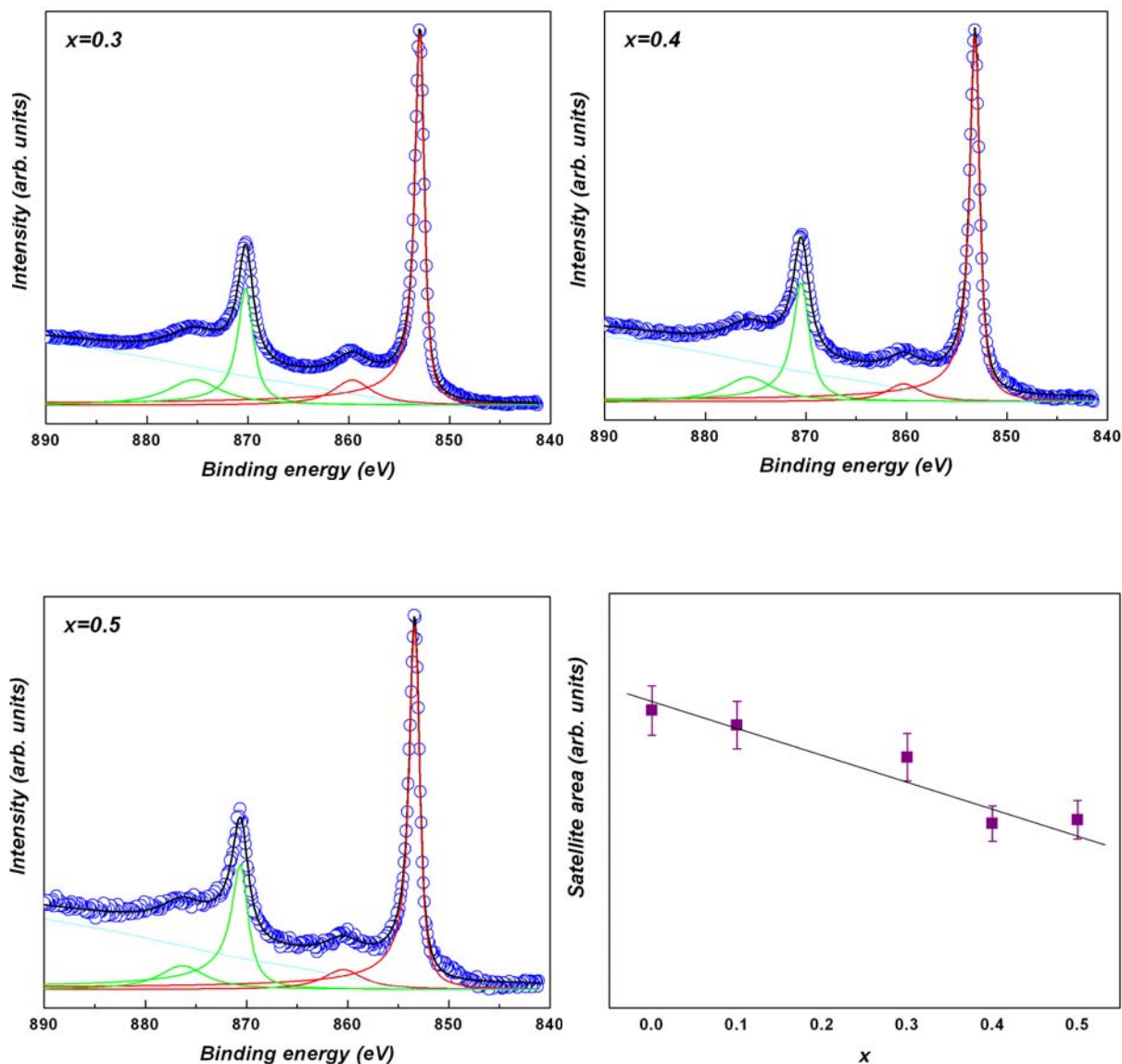
Fig .6.6. Ni 2p curve fitting results of $Ni_{0.7-x}Al_xMn_{0.3}$ alloys and the Al concentration dependence of Ni $2p_{3/2}$ satellite area

The observation of satellites implies the presence of d character in the unoccupied bands. The satellite structure intensity decreases as the Al content increases, confirming the gradual filling of the Ni 3d band. The presence of the satellite structures suggests that Ni atoms could carry a small magnetic moment.

There is an overlapping between Mn2p XPS line and Ni $L_2M_{23}M_{45}$ Auger line (Fig. 6.7). The observed spin orbit splitting, which can be identified in the distance between the two centers of energy of the $2p_{3/2}$ and $2p_{1/2}$ state is $\Delta_{so}{\approx}11.5$ eV.
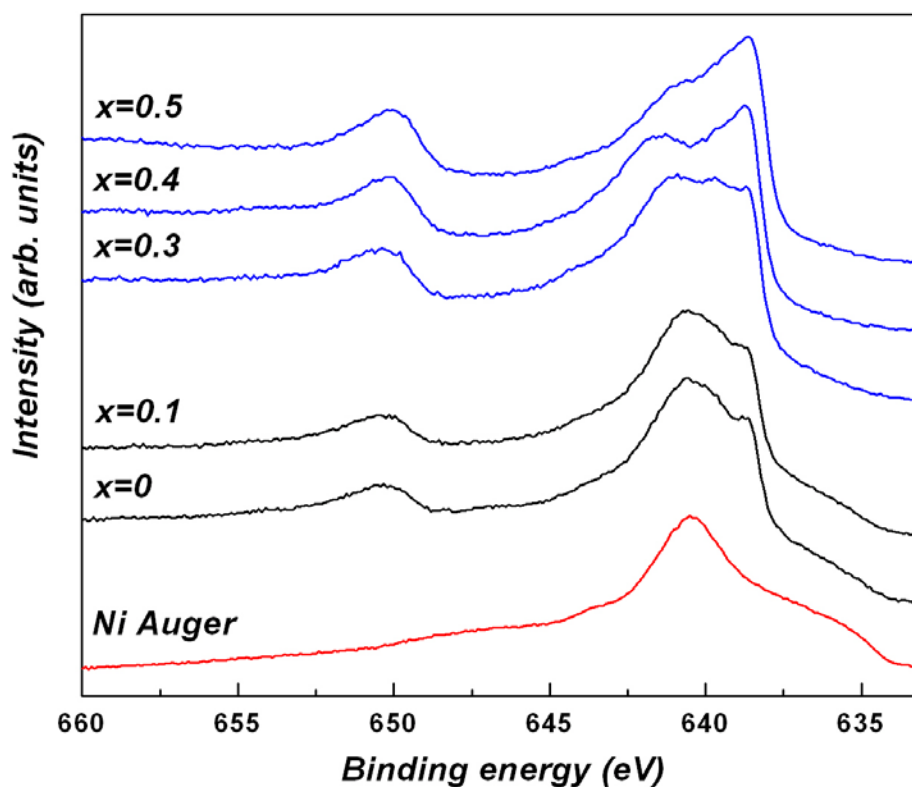
Fig .6.7. Mn 2p XPS spectra of $Ni_{0.7-x}Al_xMn_{0.3}$ alloys and Ni Auger line

After background removal, using a Shirley-type background shape, we have also fitted the Mn $2p_{3/2}$ core-level spectra for some of the investigated alloys with four components and a satellite line situated at binding energy around 644.5 eV. The curve fitting results for $Ni_{0.7}Mn_{0.3}$ alloy is given in Fig. 6.8, with the mean energy separation $\Delta_{ex} \approx 1.2$ eV. This gives direct evidence of the existence of local moments confined on Mn sites.
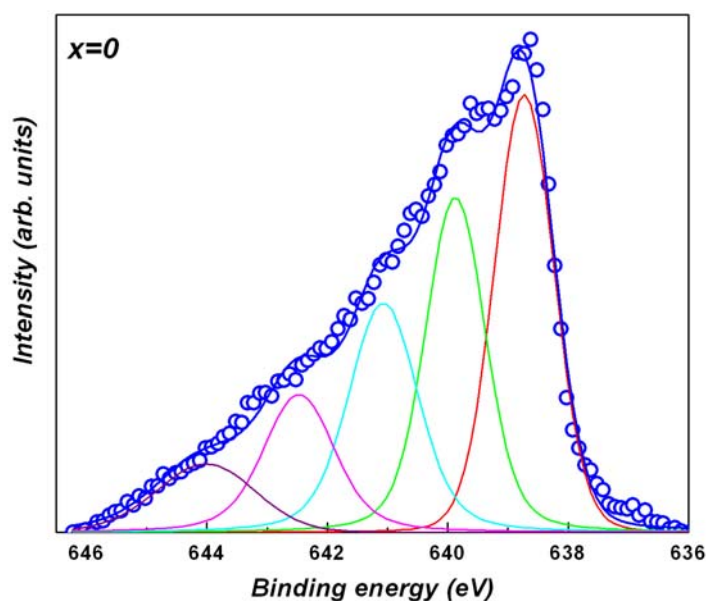
Fig. 6.8. Mn $2p_{3/2}$ curve fitting results of $Ni_{0.7}Mn_{0.3}$ alloy

103

6.3 Magnetic measurements

The temperature dependence of magnetic susceptibility of $Ni_{0.7}Mn_{0.3}$ and $Ni_{0.4}Al_{0.3}Mn_{0.3}$ alloys is given in Fig. 6.9. The susceptibility presents a maximum, specific for antiferromagnetic materials, which corresponds to Néel temperature. The values of the transition temperature are $T_N \approx 150K$ and $T_N \approx 125K$ for $Ni_{0.7}Mn_{0.3}$ and $Ni_{0.4}Al_{0.3}Mn_{0.3}$, respectively.
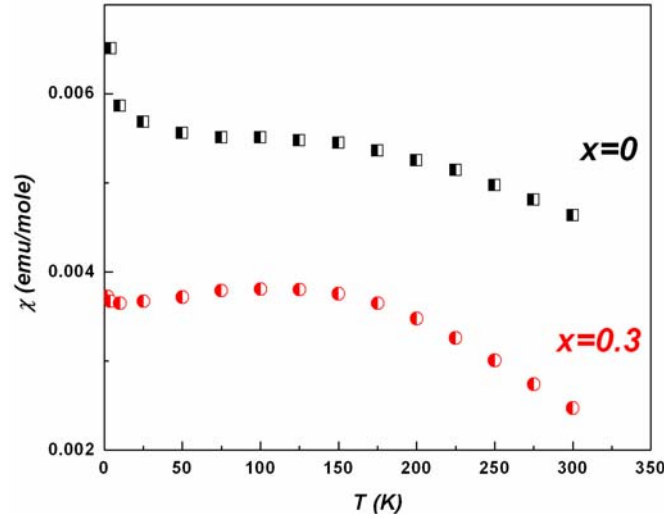
Fig. 6.9. The temperature dependence of magnetic susceptibility of $Ni_{0.7}Mn_{0.3}$ and $Ni_{0.4}Al_{0.3}Mn_{0.3}$ alloys

The increase of the magnetic susceptibility at very low temperatures could be due to some ferromagnetic impurity or a conical antiferromagnetic structure, which has a ferromagnetic component. This feature was also observed in the Chapter 4.

The spontaneous magnetization as a function of temperature is given in Fig. 6.10 for $Ni_{0.6}Al_{0.1}Mn_{0.3}$ and $Ni_{0.3}Al_{0.4}Mn_{0.3}$ alloys. The small values of spontaneous magnetization suggest a ferrimagnetic behavior of these two alloys.
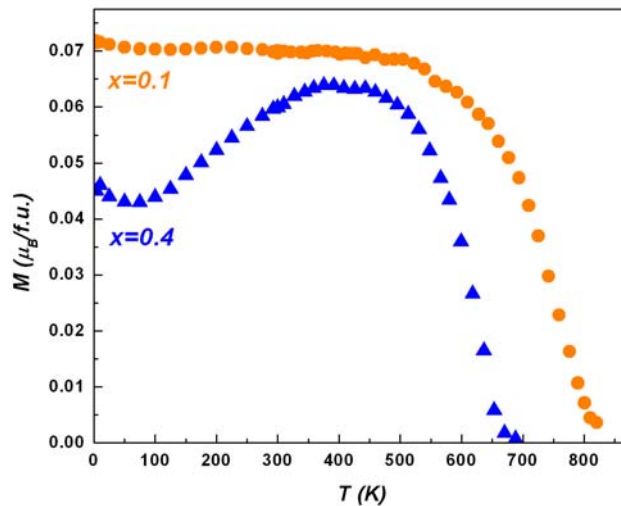
Fig. 6.10. The temperature dependence of the spontaneous magnetization of $Ni_{0.6}Al_{0.1}Mn_{0.3}$ and
$Ni_{0.3}Al_{0.4}Mn_{0.3}$ alloys

Fig. 6.11 shows the temperature dependence of the reciprocal susceptibility of $Ni_{0.6}Al_{0.1}Mn_{0.3}$ and $Ni_{0.3}Al_{0.4}Mn_{0.3}$ alloys in the paramagnetic state. The reciprocal of magnetic susceptibility follows a Néel-type hyperbolic law, specific to ferrimagnetic materials. Usually for ferromagnetic materials, the high temperature asymptote to the hyperbola has a Curie-Weiss form. Unfortunately, for these two alloys, because the transition temperature is very high and the instrumentation upper limit temperature was around 900K, the asymptote to the hyperbola was not reached.
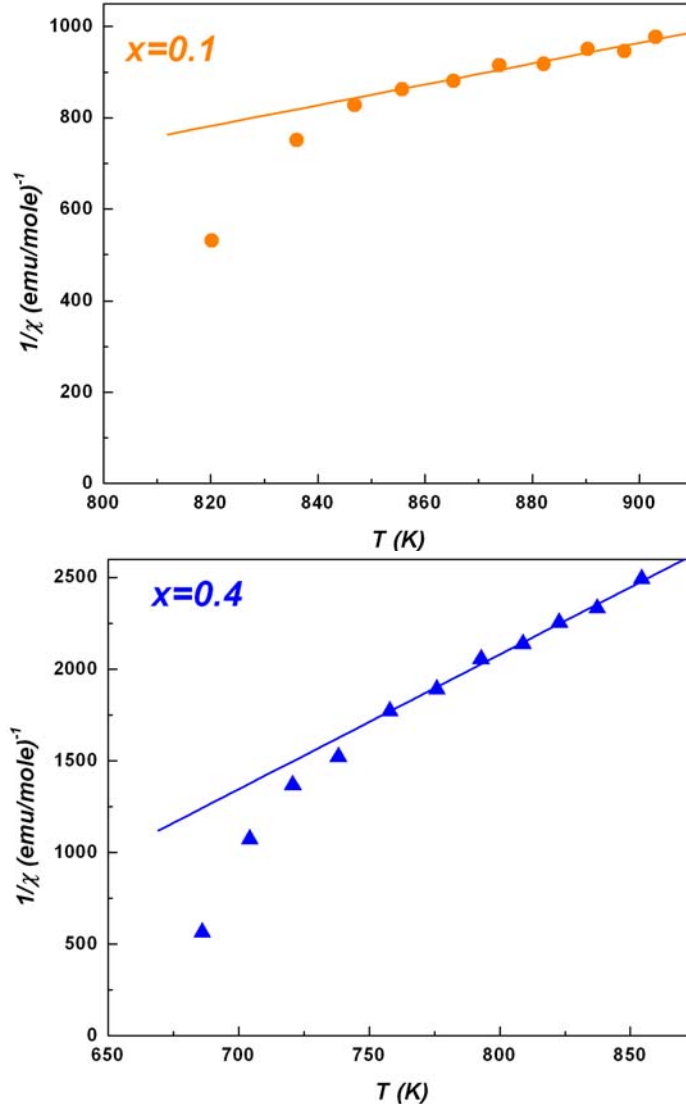
Fig. 6.11. The temperature dependence of the reciprocal susceptibility of $Ni_{0.6}Al_{0.1}Mn_{0.3}$ and $Ni_{0.3}Al_{0.4}Mn_{0.3}$ alloys

The Curie temperatures T_C have been determined in the molecular field approximation from the $M_{FM}^2(T)$ dependence (Fig. 6.12) and have the values 780.5K and 645K for $Ni_{0.6}Al_{0.1}Mn_{0.3}$ and $Ni_{0.3}Al_{0.4}Mn_{0.3}$, respectively.
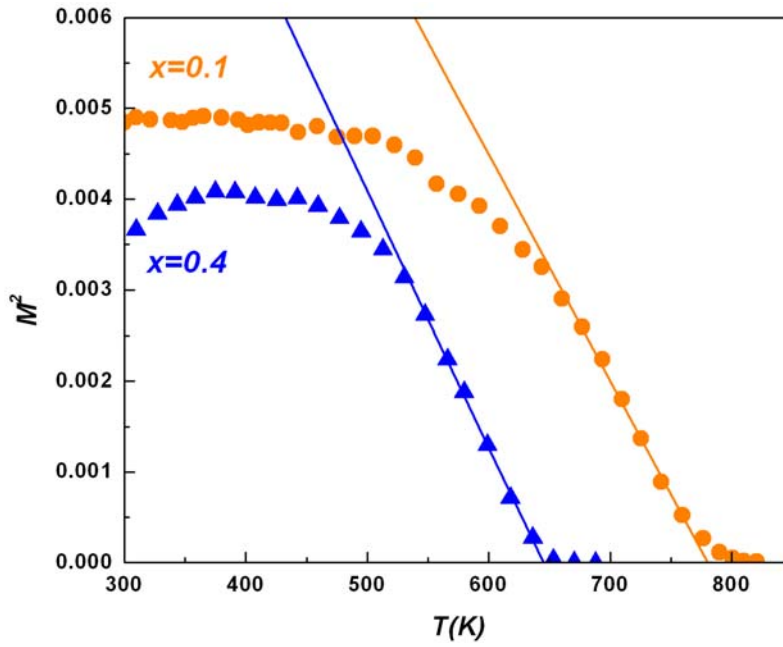
Fig. 6.12. M_{FM}^2 as a function of temperature of $Ni_{0.6}Al_{0.1}Mn_{0.3}$ and $Ni_{0.3}Al_{0.4}Mn_{0.3}$ alloys

The values and the variation of the magnetic susceptibility with the temperature (Fig. 6.13a) suggest a ferromagnetic behavior of $Ni_{0.2}Al_{0.5}Mn_{0.3}$ alloy. The ferromagnetic Curie temperature, determined in the same way like above, has the value $T_C = 400K$. The reciprocal susceptibility as a function of temperature for $Ni_{0.2}Al_{0.5}Mn_{0.3}$ alloy is presented in Fig. 6.13b and confirms the ferromagnetic behavior. The experimental data fit a Curie-Weiss law.
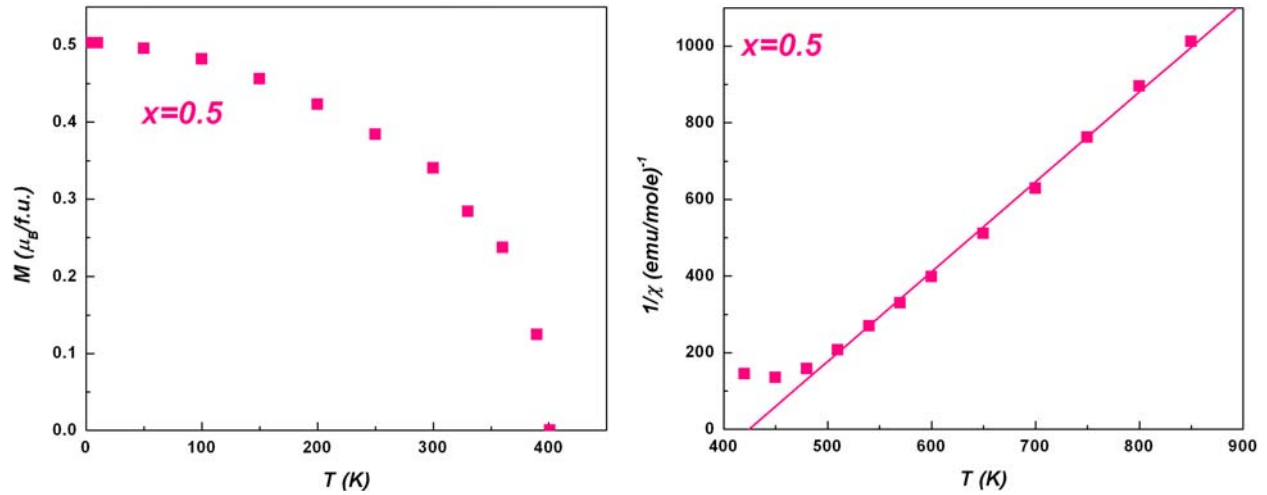
Fig. 6.13. The spontaneous magnetization (a), and the reciprocal magnetic susceptibility (b) as a function of temperature of $Ni_{0.2}Al_{0.5}Mn_{0.3}$ alloy

The magnetic behavior of $Ni_{0.7-x}Al_xMn_{0.3}$ alloys is illustrated in Fig. 6.14. We have seen in the Chapter 3 that in the ordered $AuCu_3$ structure type, Mn and Al atoms occupy the 1a position and Ni atoms are situated in 3c position. In this case the coupling between the Mn atoms

106

is ferromagnetic ($d_{Mn-Mn} > 2.9$A°). In the crystallographically disordered alloys a number of Mn atoms occupy the 3c positions and generate antiferromagnetic Mn-Mn pairs with the Mn atoms from their firs vicinity situated in 1a or 3c positions ($d_{Mn-Mn} < 2.9$A°). In $AuCu_3$ structure type 25% of atoms will occupy the 1a position and 75% the 3c position. On can see that in $Ni_{0.7}Mn_{0.3}$ alloy even if the disorder degree is considered to be zero, a number of Mn atoms will be forced to take the 3c position and to form Mn-Mn antiferromagnetic pairs. Furthermore, at this Mn concentration the alloy is crystallographically disordered (see Chapter 3), with a disorder degree very high. This explain the magnetic measurements results, which shown that $Ni_{0.7}Mn_{0.3}$ alloy has antiferromagnetic behavior.

In the Chapter 3 we have also seen that Al atoms play an important role in the stability of the crystallographically ordered structures, and the probability of the apparition of antiferromagnetic Mn-Mn pair decrease with the increase of Al concentration. This explains why $Ni_{0.6}Al_{0.1}Mn_{0.3}$ alloy has a ferrimagnetic behavior.
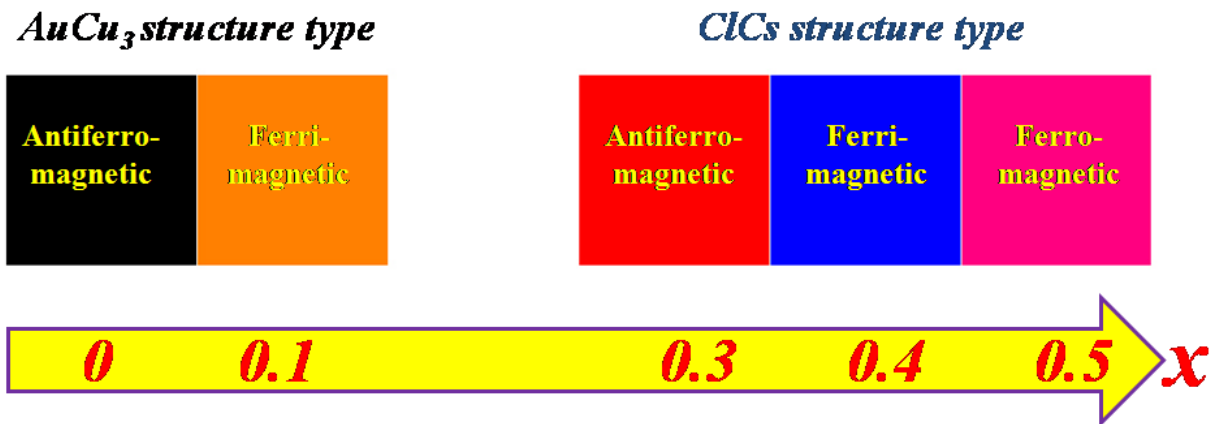
Fig. 6.14. The magnetic behavior of $Ni_{0.7-x}Al_xMn_{0.3}$ alloys

The $Ni_{0.4}Al_{0.3}Mn_{0.3}$ alloy has the lattice parameter $a \approx 2.90$Å. At this distance the Mn-Mn coupling is antiferromagnetic. The $Ni_{0.3}Al_{0.4}Mn_{0.3}$ alloy has the lattice parameter a little bit larger $a \approx 2.914$Å, but seems to be at the limit distance between the AFM and FM coupling. This could be a reason why this alloy has ferrimagnetic behavior. The lattice parameter of the $Ni_{0.2}Al_{0.5}Mn_{0.3}$ alloy is larger ($a \approx 2.94$) and it has a ferromagnetic behavior. This means that at this distance the coupling between the Mn atoms is parallel.

6.4 Conclusions

➢ The substitution of Al for Ni leads to significant changes in the crystallographic structure with remarkable effects on the electronic structure of $Ni_{0.7-x}Al_xMn_{0.3}$ alloys.

- XPS spectra pointed out the existence of local magnetic moments on Mn sites in $Ni_{0.7-x}Al_xMn_{0.3}$ alloys.

- Ni 2p core-level spectra evidenced the existence of unoccupied 3d states, which is one of the conditions for the apparition of local magnetic moments at Ni sites.

- The hybridization between the 3d Ni and 3sp Al states leads to a partial filling of the Ni 3d band, as indicated by the XPS core level and valence band spectra.

- At low Al concentrations the crystallographic structure remains the same but a change in the magnetic structure appears once Ni atoms are substituted by Al atoms. Aluminium plays an important role in stabilizing the crystallographic ordered structure.

- In the case of $Ni_{0.7-x}Al_xMn_{0.3}$ alloys, with ClCs structure type, a transition from antiferromagnetic to ferromagnetic through an intermediate ferrimagnetic behavior was evidenced once the Al concentration increases.

- This system is a very good example of how one can change the crystallographic structure type, the electronic structure and the magnetic interactions between the local magnetic moments by changing the atomic concentration of the constituents.

Summary

The main idea of the thesis was to see how one can change the crystallographic structure type, the electronic structure, the values of the magnetic moments and the sign of the interactions between the local magnetic moments by changing the atomic concentration of the constituent atoms in the ternary system Al-Mn-Ni.

The magnetic properties of the investigated alloys and compounds are strongly correlated with their crystallographic properties and reflect the changes in the first vicinity and in the distances between the 3d atoms. By changing the stoichiometry one can change the crystallographic structure type ($Mn_{1-x}Al_xNi$ and $Ni_{0.7-x}Al_xMn_{0.3}$ systems), but even if the crystallographic structure remains the same ($Mn_{1-x}Al_xNi_3$ and $Ni_{1-x}Mn_xAl$) the variation in the lattice parameters leads to changes in the coupling between the magnetic moments of 3d elements.

Some of the Al-Mn-Ni alloys are crystallographically disordered, but the crystallographic disorder degree decreases quickly with the increase of Al concentration. Aluminum plays an important role in stabilizing the crystallographic ordered structure in $Mn_{1-x}Al_xNi_3$ alloys. The same effect was observed for $Ni_{0.7-x}Al_xMn_{0.3}$ in the small range of Al concentrations.

XPS spectra and magnetic measurements pointed out the existence of local magnetic moments confined to the Mn sites for all Mn-Ni-Al alloys and compounds.

The hybridization between 3d Ni and 3sp Al states leads to a partial or complete filling of Ni 3d band, as indicated by XPS core level and valence band spectra.

XPS and magnetic measurements evidenced that Mn 3d band in $Mn_{1-x}Al_xNi_3$ and $Mn_{1-x}Al_xNi$ systems is not affected by hybridization with Al 3sp states while in $Ni_{1-x}Mn_xAl$ and $Ni_{0.7-x}Al_xMn_{0.3}$ systems Mn 3d band is strongly affected. This depends again on the interatomic distances.

XPS spectra suggest that Ni atoms could carry small magnetic moments in almost all the investigated alloys but, the Anderson condition for the existence of a local magnetic moment at Ni sites, in the ordered magnetic state, is fulfilled only for $Mn_{1-x}Al_xNi_3$ alloys. Ni atoms bring their contribution to the effective magnetic moment in the paramagnetic state. In many cases their contribution is small but for some of the investigated alloys temperature induced spin fluctuations at Ni sites were evidenced.

Magnetic measurements revealed different types of magnetic ordering: ferromagnetic, ferrimagnetic, antiferromagnetic and in some of the investigated alloys coexistence between antiferromagnetism and ferromagnetism was evidenced. By changing the stoichiometry was possible to pass from one type of magnetic ordering to another. A very good example is the $Ni_{0.7-x}Al_xMn_{0.3}$ system, where a transition from antiferromagnetism to ferromagnetism through an intermediate ferrimagnetic phase was evidenced once the Al concentration increases.

The profound understanding of the magnetic phenomena and the correct interpretation of the magnetic properties of the alloys and intermetallic compounds based on transition elements can be achieved only through the correlation of obtained data from XPS, XRD and magnetic measurements, corroborated with the band structure calculations.

References

[1] P.O.M. Dirac, Proc. Roy. Soc. Lond. A 123 (1929) 714-733

[2] J.H. Van Vleck, in "The Theory of Electric and Magnetic Susceptibilities", Oxford University Press, Oxford, 1932

[3] W. Heisenberg, Z. Physik 38 (1926) 411

[4] H.A. Kramers, Physica 1 (1934) 825-828

[5] P.W. Anderson, Phys. Rev. 115 (1959) 2-13; Solid State Physics 14 (1963) 99

[6] P. Weiss, J. Phys. Radium 6 (1907) 661

[7] W. Heisenberg, Z. Physik 49 (1928) 619

[8] E.C. Stoner, Proc. Roy. Soc. A 165 (1938) 372-414

[9] J. F. Janak, Phys. Rev. B 16 (1977) 255-262

[10] J.H. Van Vleck, Rev. Mod. Phys. 25 (1953) 220-227

[11] P.W. Anderson, Phys. Rev. 124 (1961) 41-53

[12] J. Friedel, Can. J. Phys. 34 (1956) 1190; Nuovo Cimento Suppl. 7 (1958) 287

[13] S. Alexander and P.W. Anderson, Phys. Rev. 133 (1964) A1594-A1603

[14] T. Moriya, Prog. Theor. Phys. 33 (1965) 157; In "Theory of Magnetism in Transition Metals", Proc. Int. School of Phys. Enrico Fermi, vol.37, ed. by W. Marshall, Academic, New York, 1967, p.206

[15] Y. Ishikawa, Physica B 91 (1977) 130

[16] A. Hamzic, R. Asomoza, and I.A. Campbel, J. Phys. F 11 (1981) 1441

[17] Y. Noda and Y. Ishikawa, J. Phys. Soc. Jpn. 40 (1976) 690-698

[18] K. Tajima, Y. Ishikawa, P.J. Webster, M.W. Stringfellow, O. Tochetti, and K.R.A. Ziebeck, J. Phys. Soc. Jpn. 43 (1977) 483-489

[19] K.R.A. Ziebeck, P.J. Webster, P.J. Brown, and J.A.C. Bland, J. Magn. Magn. Mater. 24 (1981) 258-266

[20] K.R.A. Ziebeck and P.J. Brown, J. Phys. F10 (1980) 2015-2024

[21] D.M.K. Paul and W. G. Stirling, J. Phys. F: Met. Phys. 9 (1979) 2439-2449

[22] Y. Ishikawa, J. Magn. Magn. Mater. 14 (1979) 123-132

[23] J.W. Cable, E.O. Wollan, W.C. Koehler, and H.R. Child, Phys. Rev. 128 (1962) 2118-2120

[24] E. Krén, G. Kádár, Phys. Lett., 29A (1969) 340-341

[25] A. J. Smith, W. G. Stirling and T. M. Holden, J. Phys. F 7 (1977) 2411-2420

[26] H. Yamada and M. Shimizu, J. Phys. F 7 (1977) L203-L209

[27] M. Kohgi and Y. Ishikawa, J. Phys. Soc. Jpn. 49 (1980) 985-993; J. Phys. Soc. Jpn. 49 (1980) 994-999

[28] K. R. A. Ziebeck, P. J. Brown, J. Deportes, D. Givord, P. J. Webster, J. G. Booth, Helv. Phys. Acta 56 (1983) 117

[29] A. Kjekshus, R. Mollebud, A.F. Andresen, and W.B. Pearson, Phil. Mag. 16 (1967) 1063

[30] T. Moriya, J. Magn. Magn. Mater. 31-34 (1983) 10-19

[31] B. T. Matthiss, R. M Bozorth, Phys. Rev. **100** (1958) 604

[32] B T. Matthias, A. M. Clogston, H. J. Williams, E. Corenzwit, R. C. Sherwood: Phys. Rev. Lett. **7** (1961) 7

[33] T. Moriya, A. Kawabata, J. Phys. Soc. Jpn. **34** (1973) 639; **35** (1973) 669

[34] T. Moriya, Spin Fluctuations in Itinerant Electron Magnetism, (Springer-Verlag, Berlin, 1985)

[35] W. Hallwachs, "¨Uber den Einfluß des Lichtes auf elektrostatisch geladene K¨orper," *Wiedemann'sche Annalen*, vol. 33, pp. 301–312, 1888

[36] H. Hertz, "¨Uber den Einfluß des ultravioletten Lichtes auf die elektrische Entladung," *Wiedemann'sche Annalen*, vol. 31, pp. 983–1000, 1887

[37] J. J. Thomson, "Cathode Rays," *Philosophical Magazine*, vol. 44, pp. 293–316, 1897

[38] A. Einstein, "¨Uber einen die erzeugung und verwandlung des lichtes betreffenden heuristichen gesichtspunkt," *Annalen der Physik*, vol. 17, pp. 132–148, 1905

[39] C. N. Berglund and W. Spiecer, "Photoemission studies of copper and silver: Theory," *Physica Review*, vol. 136, pp. A1030–A1044, 1964

[40] K. Siegbahn, C. Nordling, A. Fahlman, R. Nordberg, K. Hamrin, J. Hedman, G. Johansson, T. Bergmark, S. E. Karlson, I. Lindgren, and B. Lindberg, *ESCA–Atomic, Molecular and Solid State Structure Studied by Means of Electron Spectroscopy*. Almquist and Wicksell, Uppsala, 1967

[41] K. Siegbahn, C. Nordling, G. Johansson, J. Hedman, P. F. Heden, K. Hamrin, U. Gelius, T. Bergmark, L. O. Werme, R. Manne, and Y. Baer, *ESCA Applied to Free Molecules*. North Holland, Amsterdam, 1969

[42] K. Siegbahn, D. Hammond, H. Fellner-Feldegg, and E. F. Barnett, "Electron spectroscopy with monochromatized X–rays," *Nature*, vol. 176, pp. 245–252, 1972

[43] H. P. Bonzel and C. Client, "On the history of photoemission," *Progress in Surface Science*, vol. 49, pp. 107–153, 1995

[44] G. Ertl and J. K¨uppers, *Low Energy Electrons and Surface Chemistry*. VCH, Weinheim, 1985

[45] S. Hufner, *Photoelectron spectroscopy*. Springer–Verlag, Berlin, 1995

[46] C. Fadley, "Basic Concepts of X-ray Photoelectron Spectrocopy," in *Electron Spectroscopy: Theory, Techniques and Applications* (C. Brundle and P. Backer, eds.), vol. 2, pp. 2–156, Academic Press, London, 1978

[47] C. Cohen-Tannoudji, B. Diu, and F. Lalo¨e, *Quantenmechanik*, vol. 2. Walter de Gruyter, Berlin, 1999

[48] G. Borstel, "Theoretical aspects of photoemission," *Applied Physics A*, vol. 38, pp. 193–204, 1985

[49] W. Nolting, "Influence of electron correlations on auger electron – and appearance potential – spectra of solids," *Zeitschrift f¨ur Physik – Condensed Matter*, vol. 80, pp. 73–86, 1990

[50] J. C. Fuggle, R. L¨asser, O. Gunnarsson, and K. Sch¨onhammer, "Plasmon Gains as a Monitor of Incomplete Relaxation, Interference Effects, and the Transition from Sudden to Adiabatic Limits in Electron Spectroscopies," *Physical Review Letters*, vol. 44, pp. 1090–1093, 1980

[51] J. D. Lee, O. Gunnarsson, and L. Hedin, "Transition from the adiabatic to the sudden limit in core-level photoemission: A model study of a localized system," *Physical Review B*, vol. 60, pp. 8034–8049, 1999

[52] T. Koopmans, "¨Uber die Zuordnung von Wellenfunktionen und Eigenwerten zu den eizelnen Elektronen eines Atoms," *Physica*, vol. 1, pp. 104–113, 1933

[53] R. J. Powell and W. E. Spicer, "Optical properties of NiO and CoO," *Physical Review B*, vol. 2, pp. 2182–2193, 1970

[54] C. Powell, "Attenuation lenghts of low–energy electrons in solids," *Surface Science*, vol. 44, pp. 29–46, 1974

[55] J. C. Shelton, "Inelastic mean free paths for electrons in bulk jellium," *Surface Science*, vol. 44, pp. 305–309, 1974

[56] H. Bethe, "Zur Theorie des Durchgangs schneller Korpuskulastrahlung durch Materie," *Annalen der Physik*, vol. 5, pp. 325–400, 1930

[57] S. Tanuma, C. J. Powell, and D. R. Penn, "Proposed formula for electron inelastic mean free paths based on calculations for 31 materials," *Surface Science*, vol. 192, pp. L849–L857, 1987

[58] S. Tanuma, C. J. Powell, and D. R. Penn, "Calculations of inelastic mean free paths for 31 materials," *Surface and Interface Analysis*, vol. 11, pp. 577–589, 1988

[59] J. C. Ashley, "Interaction of low–energy electrons with condensed matter: stopping powers and inelastic mean free paths from optical data," *Journal of Electron Spectroscopy and Related Phenomena*, vol. 46, pp. 199–214, 1988

[60] S. Tanuma, C. J. Powell, and D. R. Penn, "Calculations of inelastic mean free paths: II. Data for 27 elements over 50–2000 eV range," *Surface and Interface Analysis*, vol. 17, pp. 911–926, 1991

[61] S. Tanuma, C. J. Powell, and D. R. Penn, "Calculations of inelastic mean free paths: III. Data for 15 inorganic compounds over 50–2000 eV range," *Surface and Interface Analysis*, vol. 17, pp. 927–939, 1991

[62] S. Tanuma, C. J. Powell, and D. R. Penn, "Calculations of electron inelastic mean free paths (IMFPs): IV. Evaluation of calculated of calculated IMFPs formula TPP–2 for electron energies between 50 and 2000 eV," *Surface and Interface Analysis*, vol. 20, pp. 77–89, 1993

[63] S. Tanuma, C. J. Powell, and D. R. Penn, "Calculations of inelastic mean free paths: V. Data for 14 organic compounds over 50–2000 eV range," *Surface and Interface Analysis*, vol. 21, pp. 165–176, 1993

[64] A. Jablonski, "Universal energy dependence of the inelastic mean free path," *Surface and Interface Analysis*, vol. 20, pp. 317–321, 1993

[65] J. Pendry, "Theory of Photoemision," *Surface Science*, vol. 57, pp. 679–705, 1976

[66] D. J. Spanjaard, D. W. Jepsen, and P. M. Marcus, "Effects of transmission factors and matrix elements on angular distribution of photoemission from Ag(111)," *Physical Review B*, vol. 15, pp. 1728–1737, 1977

[67] T. Schlathölter, *Theorie der spinpolarisierten Core–Level Spektroskopie für Photo– und Auger– Elektronen*. PhD thesis, Universität Osnabrück, 1999

[68] V.I. Nefedof, N.P. Sergushin, I.M. Band, and M.B. Trazhaskovskaya, Relative intensities in x-ray photoelectron spectra, Journal of Electron Spectroscopy and Related Phenomena

[69] J.H. Scofield, Hartree-slater subshell photoionization cross-section at 1254 and 1487 ev. Journal of Electron Spectroscopy and Related Phenomena

[70] D. Briggs and J. C. Rivi`ere, "Spectral Interpretation," in *Practical Surface Analysis by Auger and X-ray Photoelectron spectroscopy* (D. Briggs and M. P. Seah, eds.), vol. 1, pp. 87–140, John Wiley & Sons, Chichester, 1983

[71] S. Doniach and M.Sunjic, Many electron singularity in x-ray photoemission and x-ray line spectra from metals, J. Phys. C, 4C31:285, 1970

[72] M. Cardona and L. Ley, Photoemission in solids, Springer Verlag, Berlin, Heidelberg, 1978

[73] J. C. Slater, Quantum theory of atomic structure, McGraw-Hill, 2, 1960

[74] J. H. Wood and G. W. Pratt Jr., Physical Review

[75] C. S. Fadley, D. A. Shirley, A. J. Freeman, P. S. Bagus, and J. V. Mallow, Multiplet splitting of core-electron binding energies in transition-metal ions, Physical Review Letters

[76] C. S. Fadley and D. A. Shirley, Multiplet splitting of metal-atom electron binding energies, Physical Review A

[77] van Vleck, The dirac vector model in complex spectra, Physical Review, 45:405, 1934

[78] S. Plogmann, T. Schlatholter, J. Braun, M. Neumann, Y.M. Yarmoshenko, M.V. Yablonskikh, E.I. Shreder, E. Z. Kurmaev, A. Wrona, A. Slebarski, *Phys Rev.* B 60, 6428, (1999)

[79] L. Hedin, "Many–Body Effects," in *X-Ray Spectroscopy* (L. V. Az´aroff, ed.), pp. 226–283, Mc Graw–Hill Book Company, New York, 1974

[80] J. M. Hollas, *High resolution spectroscopy*, Butterworths & Co, London, 1982

[81] D. A. Shirley, High–resolution X–ray photoemission spectrum of the valence band of gold, Physical Review B, 5:4709–4714, 1972

[82] S. Tougaard and P. Sigmund, Influence of elastic and inelastic scattering on energy spectra of electrons emitted from solids, Physical Review B, 25:4452–4466, 1982

[83] S. Tougaard and B. Jørgensen, Inelastic Background Intensities in XPS Spectra, Surface Science, 143:482–494, 1984.

[84] S. Tougaard, Low Energy Inelastic Electron Scattering Properties of Noble and Transition Metals, Solid State Communications, 61:547–559, 1987

[85] S. Tougaard, Quantitative analysis of the inelastic background in surface electron spectroscopy, Surface and Interface Analysis, 11:453–472, 1988

[86] S. G. Chiuzbăian, Electronic structure and magnetism of selected materials, 2003.

[87] A. F. Takács, Electronic structure studies of metal-organic and intermetallic compounds, 2005

[88] H.M. Rietveld, J.Appl. Cryst. 2 (1969) 65

[89] A. Arrott, Phys. Rev. 108 (1957) 1394

[90] J.C. Riviere, in *Monographs on the Physics and Chemistry of Materials*, Clarendon Press, H. Frolich, P.B. Hirsch, N.F. Mott, A.J. Heeger, and R. Brooke, editors, Oxford, 1990, pp. 53–64

[91] H. Ebert, in *Electronic Structure and Physical Properties of Solids*, editor: H. Dreysse, Lecture Notes in Physics, vol. 535, Springer, Berlin, 2000, pp. 191; The Munich SPRKKR package, Version 3.6, http://olymp.cup.uni-muenchen.de/ak/ebert/sprkkr

[92] P. Weinberger, *Electron Scattering Theory for Order and Disordered Matter*, University Press, Oxford, 1990.

[93] A.Gonis, *Green Function for Ordered and Disordered Systems*, North-Holland, Amsterdam, 1992.

[94] P. Strange, *Relativistic Quantum Mechanics*, University Press, Cambridge, 1998.

[95] B. L. Gyorffy and M. J. Stott, in *Band Structure Spectroscopy of Metals and Alloys*, edited by D. J. Fabian and L. M. Watson, Academic Press, New York, 1973, pp. 385.

[96] H. Ebert and M. Battocletti, Solid State Commun. 98 (1996) 785

[97] L. Rednic, R. Pacurariu, V. Rednic, L.G. Pascut, V. Pop, M. Neumann, M. Coldea; *X-ray photoelectron spectroscopy and magnetism of $AlMnNi_6$ and $Al_7Mn_3Ni_{30}$,* J. Optoelectron. Adv. Mat. **9** (2007) 568 – 571.

[98] V. Rednic, L. Rednic, M. Coldea, V. Pop, M. Neumann, R. Pacurariu, A. R. Tunyagi, *X-ray Photoelectron Spectroscopy and Magnetism of $Mn_{1-X}Al_xNi_3$ Alloys,*   Cent. Eur. J. Phys. 6(3) (2008) 434-439.

[99] V. Rednic, D. Benea, M. Coldea, V. Pop, L. Rednic and M. Neumann, *KKR calculation of electronic band structure and XPS spectra of $Mn_{1-x}Al_xNi_3$ alloys*, sent for publication in J. Optoelectron. Adv. Mat.

[100] M. J. Marcinkowski, R. M. Poliak, Phil. Mag., 8, 1023(1963)

[101] C.G. Shul, M.K. Wilkinson, Phys. Rev. 97, 304 (1955)

[102] J. S. Kouvel, C. D. Graham Jr., J. J. Becker, J. Appl. Phys., 29, 518 (1958)

[103] P. J. Kaplan, R. L. Streever, Phys. Rev. B, 2, 3449(1970)

[104] F. R. de Boer, C. J. Schinkel, J. Biesterbos, S. Proost, J. Appl. Phys. 40, 1049(1969)

[105] Ul-Haq and J.G. Booth, J. Magn. Magn. Mat. 62, 256 (1986)

[106] T. Shinohara, T. Takasugi, H. Yamauchi, T. Kamiyama, H. Yamamoto, O. Izumi,
    J. Magn. Magn. Mat. 53, L1 (1985)

[107] W. B. Pearson, A handbook of Lattice Spacings and Structures of Metals and Alloys,
     (Pergamon Press, New York, 1958)

[108] J. Yeh, I. Lindau, At. Data Nucl. Tables 32,1(1958)

[109] Y. Kurtulus and R. Dronskowki, J. Sol. State Chem., 176, 390 (2003)

[110] R. Y. Umetsu, K. Fukamichi, A. Sakuma, J. Magn. Magn. Mat. 239, 530(2002)

[111] S. Plogmann, T. Schlatholter, J. Braun, M. Neumann, Yu. Yarmoshenko,
    M. V. Yabloskikh, E. I. Shreder, E. Z. Kurmaev, Phys. Rev. B, 60(1999)

[112] J. W. Cable, E. O. Wollan, W. C. Koehler, H. R. Child, Phys. Rev. 128, 2118 (1962)

[113] T. Busgen, J. Feydt, R. Hassdorf, S. Thienhaus, M. Moske, Phys. Rev. B 70,
    014111(2004)

[114] K. Kneller, in Ferromagnetismus, (Springer-Verlag, Berlin, 1962) 150

[115] V. Rednic, M. Coldea, S. K. Mendiratta, M. Valente, V. Pop, M. Neumann and L. Rednic, *X-ray Photoelectron Spectroscopy and Magnetism of $Mn_{1-x}Al_xNi$ Alloys*, J. Mag. Mag. Mat 321 (2009) 3415–3421

[116] L. Pal et al, J. Appl. Phys. **39** (1968) 538

[117] G. Bayreuther, in Magnetische Schicht-systeme, 30. Ferienkurs des Instituts für Festkörperforschung, Julich, 1999

[118] Ch. Müller, H. Wonn, W. Blau, P. Ziesche and V. P. Krivitshii, Phys Stat Sol. B 95 (1979) 215

[119] Lluis Manosa et al, J. Appl. Phys., **93**, (2003) 8498

[120] S. Morito, T. Kakeshita, K. Hirata, K. Otsuka, Acta mater. **46** (1998) 5377

[121] M. Acet, E. Duman, E. F. Wassermann, L. Manosa and A. Planes, J. Appl. Phys. **92** (2002) 3867

[122] S. Hüfner, Photoelectron Spectroscopy Principles and Applications, Springer-Verlag, Berlin (1995), p. 89

[123] P. Schieffer, C. Krembel, M. C. Hanf, G. Gewinner, J. Electron Spectrosc. Relat. Phenom. **104** (1999) 127.

[124] O. Rader, T. Mizokawa, A. Fujimori, Phys. Rev. B **64** (2001) 165414.

[125] O. Rader, E. Vescovo, M. Wuttig, D. D. Sarma, S. Blugel, F. J. Himpsel, A. Kimura, K. S. An, T. Mizokawa, A. Fujimori, C. Carbone, Europhys. Lett. **39** (1997) 429.

[126] A. Sandell, A. J. Jaworowski, , J. Electron Spectrosc. Relat. Phenom. **135** (2004) 7

[127] M. Coldea, M. Neumann, S. G. Chiuzbaian, V. Pop, L. G. Pascut, O. Isnard, A. F. Takacs, R. Pacurariu, J. Alloy Comp **417** (2006) 7

[128] H. Ebert, J. Phys.: Cond. Matter **1** (1989) 9111

[129] H. Ebert, Phys. Rev. B **44** (1991) 4406

[130] S. Plogmann et al, Phys. Rev. B **60** (1999) 6428

[131] Yu. M. Yarmoshenko et al, Eur. Phys. J. B **2** (1998) 1

[132] D.A. Shirley, Phys. Rev B **5** (1972) 4709

[133] A. Sakuma, J. Magn. Magn. Mat. **187** (1998) 105

[134] A. Kjekshus, R. Mollebud, A. F. Andresen, and W. B. Pearson, Philos. Mag. **16** (1967) 1063

[135] K. H. J. Buschow, J. F. Fast, A. M. Van Diepen and H. W. de Wijn, Phys Stat Sol. **24** (1967) 715

[136] R. Harris, M. Plischke, M. J. Zuckermann, Phys. Rev. Lett. **31**(1973) 160

[137] T. Hori, H. Shiraishi, Y. Nakagawa, J. Appl. Phys. **79** (1996) 6633

[138] K. R. A. Ziebeck, P. J. Webster, J. Phys. F: Met. Phys. **5**(1975) 1756

[139] L. F. Bates, Modern Magnetism, Cambridge Univ. Press, Cambridge, 1951

[140] V. Rednic, R. Pacurariu, L. Rednic, V. Pop, M. Neumann, M. Coldea; *Magnetism and X-ray Photoelectron Spectroscopy of AlNi$_{1-x}$Mn$_x$ Alloys;* Studia Universitatis Babes Bolyai, Physica, LI, **2** (2006) 20 – 26.

[141] V. Rednic, R. Pacurariu, L.G. Pascut, V. Pop, M. Neumann, and M. Coldea; *X-Ray Photoelectron Spectroscopy and Magnetism of Al$_2$MnNi and Al$_5$Mn$_3$Ni$_2$,* Moldavian Journal of the Physical Sciences, vol. **6** (2007) 86-91.

[142] V. Rednic, M. Coldea, O. Isnard, M. Neumann and L. Rednic, *Electronic structure and magnetic properties of Ni$_{1-x}$Mn$_x$Al alloys*, prepared for publication in Phys. Stat. Sol. B.

[143] P. B. Braun, J. A. Goedkoop, Acta Cryst. 16 (1963) 737

[144] Y. Hara, R. C. O' Handley, N. J. Grant, J. Magn. Magn. Mater. 54-57 (1986) 1077-1078

[145] M. B. Brodsky and J. O. Brittain, J. Appl Phys, **40** (1969) 3615

[146] Ch. Kittel, *Introduction to Solid State Physics*, Wiley, New York (1975)

[147] E. Burzo, E. Gratz and V. Pop, J. Magn. Magn. Mater., **123**, (1993) 159

[148] M. Coldea, D. Andreica, M. Bitu and V. Crisan, J. Magn. Magn. Mater., 157/158 (1996) 627

[149] V. Rednic, M. Coldea, O. Isnard, M. Neumann and L. Rednic, *Crystallographic and electronic structure of Ni$_{0.7-x}$Al$_x$Mn$_{0.3}$ alloys,* accepted for publication in Studia Universitatis Babes-Bolyai, Physica

List of Figures

List of Tables

List of publications

1.   V. Rednic, R. Pacurariu, L. Rednic, V. Pop, M. Neumann, M. Coldea; *Magnetism and X-ray Photoelectron Spectroscopy of AlNi$_{1-x}$Mn$_x$ Alloys;* Studia Universitatis Babes Bolyai, Physica, LI, **2** (2006) 20 – 26.
2.   L. Rednic, R. Pacurariu, V. Rednic, L.G. Pascut, V. Pop, M. Neumann, M. Coldea; *X-ray photoelectron spectroscopy and magnetism of AlMnNi$_6$ and Al$_7$Mn$_3$Ni$_{30}$,* J. Optoelectron. Adv. Mat. **9** (2007) 568 – 571.
3.   N. Aldea, P. Marginean, V. Rednic, S. Pintea, B. Barz, A. Gluhoi, B.E. Nieuwenhuys, Xie Yaning, F. Aldea, M. Neumann; *Crystalline and Electronic Structure of Gold Nanoclusters determined by EXAFS, XRD and XPS Methods,* J. Optoelectron. Adv. Mat. **9**(5) (2007) 1555.
4.   V. Rednic, R. Pacurariu, L.G. Pascut, V. Pop, M. Neumann, and M. Coldea; *X-Ray Photoelectron Spectroscopy and Magnetism of Al$_2$MnNi and Al$_5$Mn$_3$Ni$_2$,* Moldavian Journal of the Physical Sciences, vol. **6** (2007) 86-91.
5.   M. Coldea, R. Pacurariu, M. Neumann, L. G. Pascut, V. Rednic, *Spectroscopic studies on powdered CeNi5 oxidized in air,* AIP Conference Proceedings 899 (2007) 636.
6.   E.Burzo, N.Bucur, P.Vlaic and V.Rednic, *Magnetic properties and electronic structures of R-Ni-B compounds where R is a heavy rare earth,* J. Phys.: Condens. Matter **20** (2008) 7
7.   V. Rednic, L. Rednic, M. Coldea, V. Pop, M. Neumann, R. Pacurariu, A. R. Tunyagi, *X-ray Photoelectron Spectroscopy and Magnetism of Mn$_{1-x}$Al$_x$Ni$_3$ Alloys,*   Cent. Eur. J. Phys. 6(3) (2008) 434-439
8.   L. Rednic, M. Coldea, V. Rednic, M. Neumann, D. Benea, *X-ray Photoelectron Spectroscopy of MnSb1-xBix (x=0, 0.2, 0.5),* Studia Universitatis Babes-Bolyai, Physica, LIII, 2, (2008) 65 – 72
9.   V Rednic, M. Coldea, V. Pop, M. Neumann, L. Rednic and A.R. Tunyagi, *X-ray Photoelectron spectroscopy and magnetism of Mn1-xAlxNi alloys,* Proceedings of Joint International Conference Materials for Electrical Engineering (2008) 128-131.
10.   S. Pintea, P. Marginean, Stefan Gergely, V. Rednic, N. Aldea, "*Supported nickel catalysts investigated by temperature programmed reduction method*", Studia Universitatis Babes-Bolyai, Physica, L III, 2, (2008) 89-95.
11.   R. Pacurariu, V. Rednic, M. Coldea, D. Benea, V. Pop, O. Isnard, and M. Neumann; *Effects of substitution of Ni by Sb in MnNi;* Phys. stat. sol. (b), **246** (2009) 50-55
12.   S. Pintea, V. Rednic, P. Marginean, N. Aldea, X. Yaning, H. Tiandou, Z. Wu and M. Neumann, *Crystalline and electronic structure of Ni nanoclusters supported on Al2O3 and Cr2O3 investigated by XRD, XAS and XPS methods,* Superlattices and Microstructures, **46** (2009) *130-136*
13.   N. Aldea, V. Rednic, S. Pintea, P. Marginean, B. Barz, M. Neuman, A. Gluhoi, B. E. Nieuwenhuys, X. Yaning and F. Matei, *Local, global and electronic structure of supported gold nanoclusters determined by EXAFS, XRD and XPS methods,* Superlattices and Microstructures, **46** (2009) *141-148*
14.   V. Rednic, M. Coldea, S. K. Mendiratta, M. Valente, V. Pop, M. Neumann and L. Rednic, *X-ray Photoelectron Spectroscopy and Magnetism of Mn$_{1-x}$Al$_x$Ni Alloys,* J. Mag. Mag. Mat 321 (2009) 3415–3421
15.   L. Rednic, I. Deac, E. Dorolti, M. Coldea, V.Pop, V. Rednic and M. Neumann, *Magnetic Cluster Developement in In1-xMnxSb alloys,* accepted for publication in Cent. Eur. J. Phys
16.   N. Aldea, S. Pintea, V. Rednic, F. Matei, H. Tiandou and X. Yaning, *Local structure information by EXAFS analysis using two algorithms for Fourier transform calculation,* Journal of Physics: Conf Series, **182** (2009) 012056
17.   V. Rednic, M. Coldea, L. Rednic, L. G. Pascut, N. Aldea, S. Pintea and M. Neumann, *X-ray photoelectron spectroscopy and magnetism of AlDyNi, AlDyNi$_4$ and AlDy$_3$Ni$_8$ compounds,* Journal of Physics: Conf Series, **182** (2009) 012077
18.   S. Pintea, V. Rednic, M. Petru, X. Yaning and N. Aldea, *Temperature influence on the global and local structure of the chromia supported nickel catalysts,* Journal of Physics: Conf Series, **182** (2009) 012052

19. V. Rednic, D. Benea, M. Coldea, V. Pop, L. Rednic and M. Neumann, *KKR calculation of electronic band structure and XPS spectra of $Mn_{1-x}Al_xNi_3$ alloys*, sent for publication in J. Optoelectron. Adv. Mat.

20. V. Rednic, M. Coldea, O. Isnard, M. Neumann and L. Rednic, *Electronic structure and magnetic properties of $Ni_{1-x}Mn_xAl$ alloys*, prepared for publication in Phys. Stat. Sol. B.

21. V. Rednic, M. Coldea, O. Isnard, M. Neumann and L. Rednic, *Crystallographic and electronic structure of $Ni_{0.7-x}Al_xMn_{0.3}$ alloys,* accepted for publication in Studia Universitatis Babes-Bolyai, Physica

List of conference contributions

1. M. Coldea, R. Pacurariu, M. Neumann, L. G. Pascut, V. Rednic, *Spectroscopic Studies on Powdered $CeNi_5$ oxidized in air,* 6th International Conference of the Balkan Physical Union, August 22-26, 2006, Istanbul, Turkey.

2. V. Rednic, R. Pacurariu, L.G. Pascut, V. Pop, M. Neumann, M. Coldea, *X-Ray Photoelectron Spectroscopy and Magnetism of Al_2MnNi and $Al_5Mn_3Ni_2$,* 3rd International Conference on Materials Science and Condensed Matter Physics, Octombrie 3-6, 2006, Chisinau, Rep. Moldova.

3. L. Rednic, R. Pacurariu,V. Rednic, L.G. Pascut, V. Pop, M. Neumann, M. Coldea, *X-Ray Photoelectron Spectroscopy and Magnetism of $AlMnNi_6$ and $Al_7Mn_3Ni_{30}$,* Advanced Spectroscopies on Biomedical and Nanostructured Systems, Septembrie 3-6, 2006, Cluj-Napoca, Romania.

4. N. Aldea, B. Barz, P. Marginean, V. Rednic, S. Pintea, A. Gluhoi , B. E. Nieuwenhuys, Xie Yaning, F. Aldea, *Crystalline and electronic structure of gold nanoclusters determined by EXAFS, XRD and XPS methods*, 12th International Conference Romphyschem, 6-8th of September 2006, Bucharest, Romania.

5. V. Rednic, L. Rednic, R. Pacurariu, M. Coldea, M. Neumann, and M. Rakers, *X-Ray Photoelectron Spectroscopy and Magnetic Susceptibility of $Mn_{1-x}Al_xNi_3$ Alloys*, New research trends in material science - ARM-5, 2007, Sibiu, Romania.

6. S. Simon, H.Ylanen, S. Areva, H. Laaksonen, M.Vasilescu, V. Rednic, M. Neumann, *Studii MAS-NMR ŞI XPS Asupra unor Microsfere Silicatice cu Holmiu*, Simpozionul national de biomateriale, 2007, Cluj-Napoca, Romania.

7. L. Rednic, I. Deac, E. Dorolti, M. Coldea, V.Pop, V. Rednic and M. Neumann *Magnetic Cluster Development in In1-xMnxSb Alloys*, International Conference on Superconductivity and Magnetism ICSM 2008, 25-29 August 2008, Side, Turkey

8. V. Rednic, M. Coldea, V. Pop, M. Neumann, L. Rednic, A. R. Tunyagi, *X-ray photoelectron spectroscopy and magnetism of Mn1-xAlxNi alloys*, Materials for Electrical Engineering, 16-18 June 2008, Bucuresti, Romania

9. V. Rednic, M. Coldea, V. Pop, M. Neumann, L. Rednic, A. R. Tunyagi, *Effect of substitution of Mn by Al in MnNi on the crystallographic structure and magnetic properties*, International Conference on Superconductivity and Magnetism ICSM 2008, 25-29 August 2008, Side, Turkey

10. V. Rednic, M. Coldea, M. Neumann, L. Rednic, L. G. Pascut, *X-ray photoelectron spectroscopy and magnetism of $AlDyNi$, $AlDyNi_4$ and $AlDy_3Ni_8$ compounds*,Advanced Spectroscopies on Biomedical and Nanostructured Systems NANOSPEC 3, 7-10 September 2008, Cluj-Napoca, Romania

11. V. Rednic, L. Rednic, M. Coldea, V. Pop, M. Neumann, R. Pacurariu, A. R. Tunyagi, *Effects of substitution of Mn by Al in MnNi3 on the crystallographic order and magnetic properties*, International conference on Aluminum Alloys, 22-26 September 2008, Aachen, Germany

12. L. Rednic, I. Deac, E. Dorolti, M. Coldea, V.Pop, V. Rednic and M. Neumann, *X-ray photoelectron spectroscopy and magnetism of In1-xMnxSb Alloys*, Advanced Spectroscopies on Biomedical and Nanostructured Systems NANOSPEC 3, 7-10 September 2008, Cluj-Napoca, Romania

13. S. Pintea, V. Rednic, P. Marginean, N. Aldea, Xie Y., Hu Tiandou, Zhonghua Wu, M. Neuman, *Crystalline and electronic structure of Ni nanoclusters supported on Al_2O_3 and Cr_2O_3 investigated by XRD, XAS and XPS methods*, Second International Conference on Nanostructures SElf-Assembly, 2008, Rome, Italy

14. N. Aldea, V. Rednic, S. Pintea, P. Marginean, B. Barz, M. Neuman, A. Gluhoi, B. E.

Nieuwenhuys, Xie Y., F. Matei, *Local, global and electronic structure of supported gold nanoclusters determined by EXAFS, XRD and XPS methods,* Second International Conference on Nanostructures SElf-Assembly, 2008, Rome, Italy

15.   N. Aldea, V. Rednic, S. Pintea, P. Marginean, B. Barz, M. Neumann, A. Gluhoi, B. E. Nieuwenhuys, Xie Y., F. Matei, *Characterization of the supported gold nanoclusters by EXAFS, XRD and XPS methods*, Romphyschem-13, 2008, Bucharest, Romania

16.   S.Pintea, N.Aldea, P.Marginean, I.Bratu, V.Rednic, M.Neuman, Xie Yaning, *Structural and electronic characterization of the supported Ni/Cr$_2$O$_3$ and Ni/Al$_2$O$_3$ catalysts. Active metal-support interaction*, Romphyschem-13, 2008, Bucharest, Romania

17.   N. Aldea, S. Pintea**,** V. Rednic, F. Matei, *A new analysis of EXAFS spectra for close-shell systems*, Advanced Spectroscopies on Biomedical and Nanostructured Systems, 7-10th of Sept. 2008, Cluj-Napoca, Romania.

18.   N. Aldea, S. Pintea, V. Rednic, P. Marginean, R. Turcu, S. Gergely, M. Neumann, Y. Xie and F. Matei, *Local, Global and Electronic Structure of Nanostructured Systems*, The 14th Conference on "Progress in Cryogenics and Isotopes Separation", 29-31st of October 2008, Calimanesti - Caciulata, Valcea, Romania.

19.   S. Pintea**,** P. Marginean, S. Gergely, V. Rednic, N. Aldea, *TPR Study of Supported Ni Catalysts with Application in Environmental Protection, Ecology and Isotopic Exchange Reactions*, The 6th "PIM" Conference on "Isotopic Processes", 20-24th of September 2008, Cluj-Napoca, Romania.

20.   N. Aldea, S. Pintea, V. Rednic, S. Gergely, F. Matei, *Software dedicated to Fourier analysis of the X-ray line profiles* (in Romanian), Bucharest International Technical Fair, 7-11 October 2008, Bucharest, Romania.

21.   V Rednic, O. Isnard, M. Coldea, M. Neumann and L. Rednic *X-ray photoelectron spectroscopy and magnetism of Ni1-xMnxAl alloys*, E-MRS Spring Meeting, 8-12 June 2009, Strasbourg, France.

22.   S. Pintea, V. Rednic, P. Marginean, N. Aldea, D. Macovei, F. Matei, *XAS, XRD and XPS studies on nanostructured supported Co catalysts,* E-MRS Spring Meeting, 8-12 June 2009, Strasbourg, France.

23.   N. Aldea, S. Pintea, V. Rednic, F. Matei, X. Yaning *Comparative study of EXAFS spectra for close-shell systems*, International Conference on Amorphous and Nanostructured Chalcogenides, 29 June-7 July 2009, Constanta, Romania.

24.   N. Aldea, S. Pintea, V. Rednic and F. Matei, *New trends in X-ray line profiles analysis using various mathematical distributions. A comparative study*, Workshop on Trends in nanoscience: theory, experiment, technology, 23-30 August 2009, Sibiu, Romania.

25.   S. Pintea, V. Rednic, P. Mărginean and N. Aldea, *Changes induced by the heat treatment in the global and local structure of the Ni/Al$_2$O$_3$ and Ni/Cr$_2$O$_3$ catalysts*, Workshop on Trends in nanoscience: theory, experiment, technology, 23-30 August 2009, Sibiu, Romania.

Acknowledgements